TEMPORAL REGULARIZATION AND ARTIFACT CORRECTION IN SINGLE SLOW-ROTATION DYNAMIC SPECT

by

Thomas Humphries

M.Sc., Simon Fraser University, 2007

B.Math., University of Waterloo, 2005

THESIS SUBMITTED IN PARTIAL FULFILLMENT

OF THE REQUIREMENTS FOR THE DEGREE OF

DOCTOR OF PHILOSOPHY

IN THE

DEPARTMENT OF MATHEMATICS

FACULTY OF SCIENCE

© Thomas Humphries 2011
SIMON FRASER UNIVERSITY
Summer 2011

All rights reserved.
However, in accordance with the *Copyright Act of Canada*, this work may be reproduced, without authorization, under the conditions for “Fair Dealing.” Therefore, limited reproduction of this work for the purposes of private study, research, criticism, review, and news reporting is likely to be in accordance with the law, particularly if cited appropriately.

APPROVAL

Name: Thomas Humphries

Degree: Doctor of Philosophy

Title of Thesis: Temporal regularization and artifact correction in single slow-rotation dynamic SPECT

Examining Committee: Dr. Razvan Fetecau, Assistant Professor (Chair)

Dr. Manfred Trummer, Professor
Senior Supervisor

Dr. Anna Celler, Adjunct Professor
Senior Supervisor

Dr. Steven Ruuth, Professor
Supervisor

Dr. Paul Tupper, Associate Professor, Mathematics
Internal Examiner

Dr. Grant Gullberg, Senior Scientist,
Center for Functional Imaging,
Lawrence Berkeley National Laboratory
External Examiner

Date Approved: July 27, 2011

Abstract

Single photon emission computed tomography (SPECT) is a diagnostic functional imaging modality wherein the distribution of a radioactive tracer inside the body is estimated based on data acquired from around the patient by a slowly rotating camera. Conventional SPECT image reconstruction assumes that this distribution remains constant during acquisition. In this thesis we investigate imaging of a time-varying distribution of radiotracer, which results in a highly underdetermined reconstruction problem. Recovery of an accurate dynamic image from this data requires the use of additional constraints, including temporal regularization. This work builds on the dSPECT approach of Farncombe et al., which uses simple inequality constraints to restrict the temporal behaviour of the reconstructed image.

We first investigate the use of a stronger temporal constraint than the one used in dSPECT, to improve the quality of reconstructed images. Since dynamic tracer behaviour in the human body arises as a result of continuous physiological processes, changes in tracer concentration should follow a smooth time activity curve (TAC). We propose a modification to dSPECT, denoted d^2EM, which promotes smoothness by constraining the concavity of the TAC in every voxel of the reconstructed image. Digital phantom simulations comparing the performance of d^2EM versus the original dSPECT algorithm show that d^2EM provides more accurate images, with smoother, more consistent TACs within dynamic regions of interest. The d^2EM method is especially successful in simulations featuring high levels of noise and relatively gradual tracer kinetics.

We then examine artifacts in dynamic images reconstructed from single slow-rotation data, which occur due to the fact that only a small number of views of the object are acquired by the camera at any one time. Particular emphasis is placed on image artifacts caused by the effects of attenuation on the projection data, which can be severe. Using realistic 3D phantom simulations, as well as real-life dynamic renal SPECT data, we investigate methods to correct for these artifacts. The correction methods are shown to substantially improve the accuracy of reconstructed TACs in the presence of attenuation.

Acknowledgments

As I look back on my six years of study as a graduate student at SFU, I realize just how many people have played a role in my growth as a student, researcher and a person. My supervisors Dr. Anna Celler and Dr. Manfred Trummer have both been great sources of support and mentorship to me throughout both my M.Sc. and Ph.D. studies. They have given me a tremendous amount of freedom to pursue my own research interests while also keeping me on track, and helping me to navigate the occasionally perplexing and intimidating path toward scholarship. I owe both of them a great debt and hope that I can do them proud in my future research endeavours. I would also like to thank Dr. Steve Ruuth, Dr. Paul Tupper and Dr. Grant Gullberg for taking part in my Ph.D. defence and providing me with useful feedback and advice.

I owe thanks to several people with respect to the research presented in this thesis. The original dEM reconstruction code was provided to me by Dr. Troy Farncombe, which gave me a great head start in investigating dynamic imaging. Ahmed Saad provided me with the probabilistic segmentation program used in Chapter 5, and spent a non-trivial amount of time helping me with its use, for which I am very appreciative. The personnel at St. Paul's Hospital in Vancouver were very helpful with the acquisition of the dynamic renal data used in Chapter 5, with particular thanks being owed to Dr. Rajpaul Attariwala, Nazma Tarmohamed and Dr. George Sexsmith. I am also indebted to the Natural Sciences and Engineering Research Council of Canada, who have supported me through both my M.Sc. and Ph.D. work.

Part of what has made my time as a grad student enjoyable is working in the company of many bright and motivated people. At the Medical Imaging Research Group at Vancouver General Hospital I have been privileged to spend time and share many tasty lunches with Dr. Celler, Dr. Sergey Shcherbinin, Dr. Andriy Andreyev, Tyler Hughes and Josh

Grimes. I've also enjoyed sharing the ups and downs of being a grad student with fellow math department members at SFU like Todd Keeler, Bryan Quaife, Chiaka Drakes, Radina Droumeva and Sudeshna Ghosh.

Finally, I have to thank my parents Dick and Margie for their unconditional support and love throughout my studies, as well as my brother Ian and sister Tessa. I am truly blessed to have such a great family!

Thomas Humphries
July 31, 2011

Contents

List of Tables

List of Figures

Preface

Organization of thesis

This work is divided into six chapters and one appendix, which we now briefly describe.

1. Nuclear medicine and dynamic SPECT

The fundamental concepts of nuclear medicine, and SPECT imaging in particular, are discussed. The mathematical models and image reconstruction methods used in SPECT imaging are presented, as well as a review of existing research on dynamic SPECT imaging. We introduce the dSPECT approach, upon which the research presented in this thesis is built.

2. Concavity-constrained dSPECT reconstruction

The implementation of dSPECT as an expectation maximization-based algorithm (dEM) is discussed in detail. We then present the design and implementation of a new algorithm, denoted d^2EM, which extends the dEM approach by imposing a stronger temporal constraint. This constraint restricts the concavity of the time activity curve (TAC) in every voxel of the image.

3. Experimental validation of d^2EM

The performance of d^2EM is assessed against dEM in a series of simulations using 2D digital phantoms. We assess the effects of object geometry, kinetic behaviour and noise level on the performance of both algorithms, using several quantitative measures of error.

Dynamic images produced using OSEM to reconstruct each frame of the image independently (based on more complete projection data than used in the simulations with dEM and d^2EM) are also used as a basis of comparison.

4. Artifacts in slow-rotation dynamic SPECT

Artifacts which occur in dynamic images reconstructed from data acquired with a single slow camera rotation are identified and discussed. Particular emphasis is placed on artifacts resulting from the effects of attenuation on projection data, which can be severe. We show that these artifacts occur despite the inclusion of attenuation modeling in the system matrix used for image reconstruction. Two post-reconstruction approaches to correct for these artifacts are then proposed.

5. 3D simulations and experiments

Digital phantom simulations of a dynamic renal SPECT study are performed to assess the severity of artifacts caused by attenuation and other effects. We then investigate the effectiveness of the methods proposed in Chapter 4 in correcting for these artifacts. Experiments using two sets of real-life renal data acquired from healthy volunteers are also performed to further validate the approach.

6. Conclusions and future work

The findings of this work are summarized, and some avenues for further investigation are suggested.

Appendix A: Full experimental results

Since a large number of digital phantom simulations were performed, the full results of these experiments are included in an appendix at the end of the thesis. These results are summarized or referenced in the body of the thesis.

Notation

Mathematical symbols that are used extensively throughout the thesis are listed here for reference.

i	the index referring to a voxel in the discretized image.
j	the index referring to a bin in the projection data.
k	the index referring to a time frame of the dynamic image.
I	the total number of voxels in the image.
J	the total number of projection bins at every camera stop.
K	the number of stops made by the camera. This is also the number of time frames reconstructed in the dynamic image.
x	the image vector of length I being reconstructed in the static case.
x'	the image vector of length IK being reconstructed in the dynamic case.
$\tilde{x}$	the vector of length IK over which the dEM algorithm optimizes.
$\tilde{\tilde{\mathrm{x}}}$	the vector of length IK over which the d^{2}EM algorithm optimizes.
A	the $IK \times IK$ difference tensor used in dEM.
B	the $IK \times IK$ difference tensor used in d^{2}EM.
C	the $JK \times I$ system matrix used in static SPECT reconstruction.
C'	the $JK \times IK$ system matrix used in slow-rotation dynamic SPECT reconstruction.
p	the projection data vector of length JK, which includes noise.
$r^{(\mathrm{n})}$	the residual, defined in (3.1).
$E^{(\mathrm{n})}$	the total relative error of an image, defined in (3.2).
ε	the relative error of the mean TAC within a region of interest (ROI), defined in (3.3).
$\bar{\sigma}$	the weighted relative standard deviation between voxel TACs within an ROI, defined in (3.4).
$\mathcal{S}$	the average relative shape error between voxel TACs within an ROI, defined in (3.5).

Chapter 1

Nuclear medicine and dynamic SPECT

Diagnostic medical imaging can be broadly divided into two categories: anatomical and functional. *Anatomical* imaging, which includes modalities such as computed tomography (CT), magnetic resonance imaging (MRI) and ultrasound, provides information about the spatial distribution of different tissues within the body. Conversely, *functional* imaging aims to assess the *in vivo* physiology of tissues and organs, by measuring the distribution of some imaging agent within the patient body. While it is possible to perform functional imaging using CT or MRI [40, 46], the most common functional imaging methods are nuclear medicine (NM) procedures.

In nuclear medicine imaging, a pharmaceutical agent labeled with a radioactive tracer is introduced to the patient. This radiopharmaceutical is engineered so that it localizes within an organ or tissue type of interest after a short period of time, after which its distribution can be measured using an imaging system. The absolute or relative levels of tracer absorbed within the targeted region give an indication of physiology.

NM includes modalities such as planar scintigraphy, positron emission tomography (PET) and single photon emission computed tomography (SPECT). The focus of this work is SPECT, and particularly the application of SPECT to assessing physiological processes that are characterized by relatively rapid dynamic tracer behaviour. In this chapter we provide basic information needed to understand the work in later chapters, including a description of the SPECT imaging process, how SPECT acquisition is modeled, and mathematical methods used to generate SPECT images. We also review existing literature specifically addressing the problem of dynamic SPECT imaging.

1.1 Fundamentals of SPECT imaging

1.1.1 The SPECT imaging process

The first step in SPECT imaging is the administration of a radiopharmaceutical tracer to the patient. The tracer includes both a biological component, which provides the means by which it will accumulate in the organ or tissue of interest, and a radionuclide component, which provides the means by which it will be detected. ^{99m}Tc-sestamibi, for instance, is a common radiopharmaceutical used for measuring blood perfusion in the myocardium (heart muscle). It consists of the chemical compound methoxyisobutylisonitrile (MIBI) labeled with technetium-99m, a radioactive isotope which emits gamma rays (photons) and has a half-life of roughly six hours. The choice of radiopharmaceutical for a nuclear medicine procedure depends on what aspect of physiology one wants to image, as well as other considerations such as the half-life of the radionuclide and how easily it can be produced.

The base SI unit of radioactivity is a becquerel (Bq), with one Bq corresponding to one nuclear decay per second[1]. A typical SPECT procedure involves administering between 50-700 MBq of the tracer to the patient. Since nuclear decay is a Poisson process, the direction of every photon emission is random, as well as the time interval between emissions. The amount of tracer administered to the patient must therefore be large enough so that a statistically significant number of *counts* can be recorded during the imaging time, while remaining as low as reasonably achievable[2] so that the patient is not subjected to an unnecessarily large dose of radiation. Typically, the dose of radiation administered during a SPECT procedure is several times smaller than that administered during a diagnostic CT scan.

The distribution of the tracer within the body is measured using a gamma camera. A typical gamma camera consists of a bed on which the patient lies, and a rotating gantry consisting of between one and three camera heads. Each head consists of a collimator, detector, photomultiplier tube (PMT) array and electronic components, as illustrated in Figure 1.1. The detector is typically a scintillator crystal such as sodium iodide, which produces a flash of light when a photon interacts with it. The light is converted by the PMT array into

---

[1] The non-SI unit known as the curie (Ci) is sometimes used as well. One Ci = 3.7×10^{10} Bq.

[2] This principle is known as “ALARA” in the field of radiation protection.

an amplified electrical signal. This signal is then recorded by the electronic components, which determine the position on the detector surface at which the event occurred.

Detected events are usually *binned* by their position into a discretized grid of pixels overlaid on the detector surface. The camera electronics also measure the energy of the incident photon. All photons originating from the radiotracer are emitted with a signature energy, and only photons whose energies are close to the signature energy of the radiotracer are recorded as events by the camera software. Some radioisotopes emit photons with one of several signature energies.

A collimator is required because the detector crystal on its own is not capable of determining the direction from which an incident photon originated. Without any directional information, it is impossible to reconstruct the spatial distribution of the tracer. The collimator is a physical filter, usually made of lead, that sits on top of the detector and limits the *acceptance angle* of incident photons. The most common type is a parallel hole collimator, which consists of a honeycomb-like array of narrow hexagonal channels, separated by thin septa. Since a photon must pass through one of these channels to reach the detector surface, the collimator ensures in principle that each detected photon must have originated from somewhere in the narrow field of view defined by the acceptance angle[3]. As a result of collimation, only a small number of emitted photons (on the order of 1 in 10,000) are detected by the camera system. Thus, the sensitivity of SPECT (ratio of photons detected to photons emitted by the tracer) is quite low compared to PET, which does not require mechanical collimation of this nature.

While the collimator would ideally ensure that any detected photons originate along the line normal to the point of detection, in practice every collimator channel has a conical field of view determined by the acceptance angle of the collimator. The acceptance angle is determined by the ratio of channel length to channel width. Consequently, objects that are farther away from the detector surface appear blurred compared to objects that are close to it, as illustrated in Figure 1.2. This effect is referred to as *collimator blurring* or *depth-dependent resolution*. A collimator with a small acceptance angle reduces the effect of blurring, but also reduces the sensitivity of the system.

---

[3] It is also possible for a photon originating from outside this field of view to pass through one or more collimator septa and still be detected. This phenomenon, known as *septal penetration*, is negligible in most SPECT studies.

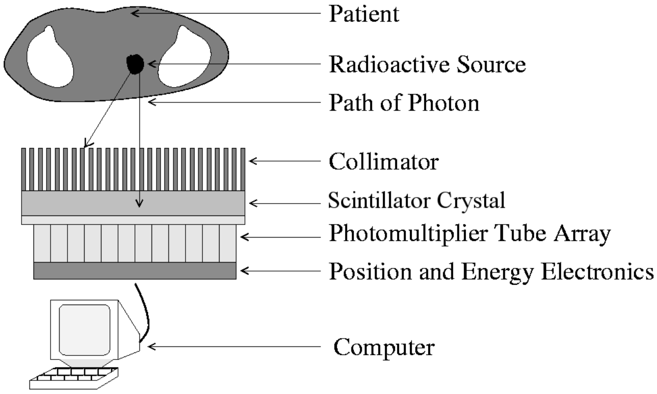

Figure 1.1: Typical SPECT camera system construction, consisting of collimator, scintillator crystal (detector), photomultiplier tube array and electronic components. Figure reproduced from [76] with permission of the author.

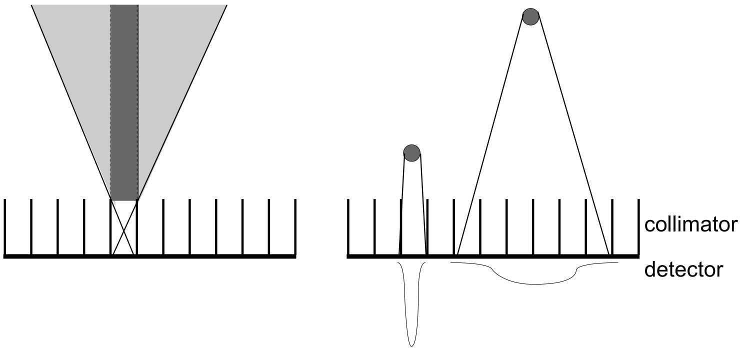

Figure 1.2: Illustration of the effect of depth-dependent collimator resolution on projection data. On the left, the idealized field of view (FOV) provided by the collimator (dark grey) is shown versus the actual FOV determined by the angle of acceptance (light grey). On the right, the effect of collimator blurring is shown in the profiles drawn under the detector. Two identical sources are present, but the one farther from the detector appears blurred in the projection data due to depth-dependent collimator resolution. Both figures are exaggerated for the sake of clarity.

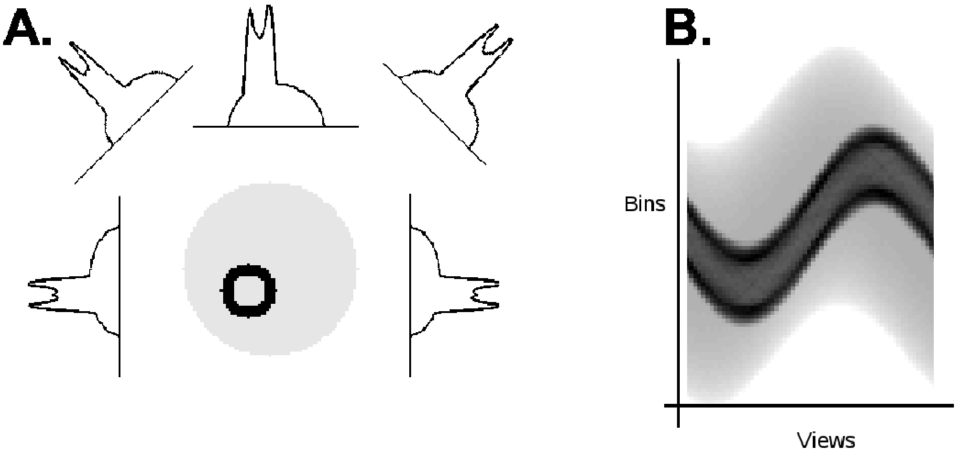

Figure 1.3: Illustration of the acquisition of projection data around an object. Figure A: a 2D object containing activity (dark grey indicating greater concentration) is imaged from several angles, giving a series of 1D projections. Figure B: a sinogram consisting of 64 views acquired from 360° around the object in Figure A.

Over the course of acquisition, the camera gantry rotates around the patient in a "stop and shoot" motion: it remains stationary for some period of time (typically 10-20 seconds) while detecting emitted photons, then rotates by a small angle and stops again. In doing so, the camera acquires a number of discrete views from around the patient, each of which can be considered as a two-dimensional projection of the 3D distribution of tracer (*activity*) in the patient. The projection data corresponding to a 2D slice of the object being imaged can be viewed as a *sinogram* (Figure 1.3), which shows how the projections vary as a function of the acquisition angle. At a minimum, projections acquired from a 180° arc around the patient are needed to accurately reconstruct the distribution of activity, although a full 360° rotation is used in many applications. Using two or three camera heads improves camera sensitivity and reduces the amount of time needed to acquire sufficient projection data.

As the photons emitted from the tracer pass through matter, they may interact with it in one of several ways. *Photoelectric absorption* occurs when the photon interacts with an atomically bound electron and is completely absorbed as a result. *Scattering* occurs when the photon is deflected by some angle, changing its direction. The most prevalent type of scattering in SPECT studies is *incoherent* (Compton) scattering, where the photon deflects off of an electron within the material, losing energy in the process[4]. Although the scattered photon loses energy, it may still be recorded as an event if it passes through the collimator, due to the limited energy resolution of the detector.

The probability that a photon is absorbed or scattered depends on the quantity and density of the material through which it passes. *Attenuation*, which refers to photons that are not detected as a result of photoelectric absorption or scattering, produces the appearance of lower activity, especially in regions that are located deep within the body or surrounded by dense tissue, such as bone. As a result, it degrades image accuracy if it is not taken into account during image reconstruction. Photons which are detected by the camera after scattering also degrade image quality since they provide incorrect information about the spatial distribution of the tracer (See Figure 1.4). To account for these effects, current SPECT procedures usually involve the acquisition of an *attenuation map* which quantifies the probability (given by an *attenuation coefficient*) that photons will be attenuated when passing through the tissue at any location in the body. The attenuation coefficient, denoted μ, depends on the nature of the tissue as well as the energy of the incident photon. The attenuation map is typically obtained from either a CT or transmission scan, which occurs in tandem with the acquisition of SPECT projection data.

1.1.2 SPECT system modeling

The simplest system model for the SPECT acquisition process is that the number of counts recorded at any location on the detector is proportional the integral of the activity distribution along the line normal to that point. In 2D, this model can be described by the Radon transform [54]. Suppose the activity distribution is given by a continuous function $f(\mathbf{y})$, where $\mathbf{y} = (y_1, y_2)$ gives the co-ordinates in space. Then, the Radon transform $\mathcal{R}[f]$ is parameterized by an angle ϕ and distance r:

$$\begin{aligned} \mathcal{R}[f](r,\phi) &= \int_{-\infty}^{\infty} f(r\xi(\phi) + \tau\xi^{\perp}(\phi))\, d\tau \qquad (1.1) \\ &\equiv \breve{f}(r,\phi), \end{aligned}$$

---

[4] A different effect known as *coherent* (Rayleigh) scattering causes photons to be deflected without losing energy, but occurs primarily when photons have lower energies than those emitted by most SPECT tracers.

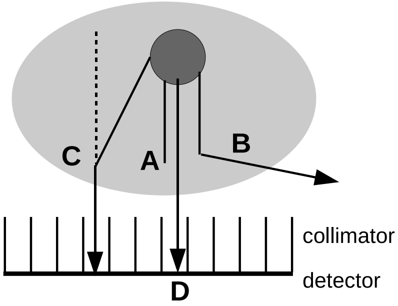

Figure 1.4: Effects of attenuation and scatter on projection data. A source (dark grey) is surrounded by attenuating material (light grey). Photon A is absorbed; photon B is scattered and not detected; photon C is scattered and detected, giving false positional information (dashed line); photon D is detected normally.

where $\xi = (\cos\phi, \sin\phi)^T$ and $\xi^\perp = (-\sin\phi, \cos\phi)^T$. This parameterization is illustrated in Figure 1.5. Holding ϕ fixed gives the 1D projection of $f(y)$ along lines parallel to $\xi^\perp$.

Equation (1.1) describes a continuous function $\breve{f}(r, \phi)$ representing the projection of the continuous activity distribution $f(\mathbf{y})$ along any line through the object. In the context of SPECT, however, $\breve{f}$ is only known for a discrete set of r values (corresponding to bins on the detector), and ϕ values (corresponding to the finite number of views taken by the camera). Furthermore, the unknown activity distribution $f(\mathbf{y})$ must be discretized (as a pixelized image, for instance) in order to be computed and stored. This discrete Radon transform can be represented as a linear system of equations:

$$Rx = p, \tag{1.2}$$

where x is the vector representing the discretized distribution of activity (the image), p is the vector of discretized projection data (i.e., the counts in each detector bin at every angle), and R is the system matrix. Let I be the total number of image pixels, and JK be the total size of the projection data (the number of bins on the detector, J, times the number of views acquired, K). Then, R is a $JK \times I$ matrix, with R_{ji} representing the contribution of the i^{th} image pixel to the j^{th} projection bin. A simple model is for R_{ji} to be given by the area of the intersection between the i^{th} pixel and the ray normal to the j^{th} bin, divided by the

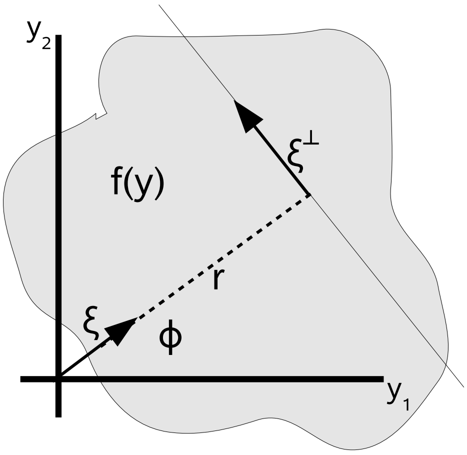

Figure 1.5: Parameterization of the Radon transform in 2D. $\breve{f}(r, \phi)$ is obtained by integrating $f(\mathbf{y})$ along the solid line perpendicular to $r\xi$.

total area of intersection between the ray and the object (Figure 1.6). The matrix R is quite sparse, as each pixel contributes to only a small fraction of the total number of detector bins. Since SPECT data is noisy as a result of the stochastic nature of photon decay, the data vector p should be viewed as a random variable, with each of the p_j having a Poisson distribution.

The Radon transform alone is not adequate to accurately model the SPECT acquisition process, since it does not include important physical effects such as collimator blurring, attenuation and scatter. To model the acquisition process accurately, these effects should be included in the system matrix as well. In practice, attenuation and collimator blurring are usually directly included as part of the system matrix, but scatter is not. The inclusion of scatter modeling in the system matrix reduces its sparsity considerably, which significantly increases the computation time of any reconstruction algorithm. Thus, if scatter compensation is attempted, it is typically done using other approaches [39, 76].

Denoting a general system matrix by C (to distinguish it from the system matrix R that results only from discretizing the Radon transform), the system then becomes:

$$Cx = p. \tag{1.3}$$

This model is applicable to both 2D and 3D imaging; in the 3D case, x represents a volumetric image consisting of discrete *voxels*, reshaped into a vector, and p corresponds to

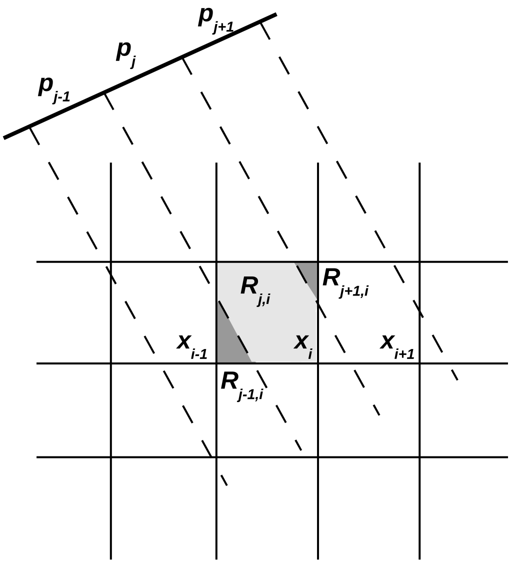

Figure 1.6: Discretization of the Radon transform into the linear system (1.2). The lightly shaded area, which corresponds the system matrix element R_{ji}, is the intersection of the normal ray corresponding to the j^{th} bin with the i^{th} image pixel. The areas corresponding to $R_{j-1,i}$ and $R_{j+1,i}$ are shaded in dark.

pixels on a 2D detector surface that has acquired multiple views around the object. Three dimensional SPECT images are typically viewed as a series of 2D slices through the 3D volume.

1.1.3 SPECT image reconstruction

Approaches to reconstruction of an image based on tomographic data can be broadly divided into two categories; analytic methods and iterative methods. Analytic methods are based on the Radon transform model (1.1) of the system; the most popular of these by far is the method of filtered backprojection. Iterative approaches are based on the linear system model (1.3), and include the algebraic reconstruction technique, maximum-likelihood expectation maximization, ordered subsets expectation maximization, maximum *a posteriori* expectation maximization, and least-squares methods.

Analytic reconstruction algorithms

Generally speaking, analytic algorithms are not appropriate for dynamic SPECT imaging, as they require that the activity distribution be unchanging during acquisition. As such, we only discuss them briefly here; a more thorough treatment is presented in [38]. Analytic methods are based on the Central Section Theorem, which relates the Radon transform of an image to the Fourier transform. This theorem provides an explicit formula for the inversion of the Radon transform, which can be applied to recover an image from projections. This formula is based on the continuous Radon transform, however, and since the Radon transform of the image is only known for discrete values in practice, applying the inversion formula directly is difficult. Instead, the method of filtered backprojection (FBP) is most commonly used.

FBP is based on the backprojection operator $\mathcal{B}$, which maps the Radon transform of the image, $\breve{f}$ (i.e., the projection data), back into image space:

$$\mathcal{B}[\breve{f}](y_1, y_2) = \int_0^{\pi} \breve{f}(y_1 \cos\phi + y_2 \sin\phi, \phi)\, d\phi. \tag{1.4}$$

Intuitively, this operation can be viewed as “smearing” the counts from every projection bin back along the ray associated with it, then normalizing. When image space and projection space are discretized, the backprojection at (y_1, y_2) is therefore a weighted average of the counts in every projection bin to which the image pixel containing the point contributed. The FBP reconstruction algorithm is given by:

$$f(\mathbf{y}) = \mathcal{B}\left[\mathcal{F}_1^{-1}\left[|k|\, \mathcal{F}_1 \breve{f}\right]\right], \tag{1.5}$$

where $\mathcal{F}_1$ is the 1D Fourier transform, and k is the frequency variable in Fourier space. The term $|k|$, known as the ramp filter, must be included to properly invert the Radon transform; its omission results in a severely blurred image. Since the ramp filter amplifies all high-frequency components of the data (i.e. noise), however, other filters are sometimes used as well in order to reduce image noise [8].

Historically FBP has been popular because it is computationally fast while providing reasonable image quality. As computational speed has increased, however, iterative algorithms have become the method of choice for image reconstruction, as they allow much greater flexibility for modeling different physical effects that cannot be incorporated into the Radon transform model.

Iterative reconstruction algorithms

Iterative approaches to image reconstruction are based on the linear system model (1.3). This system is usually very large; for a 3D image, for instance, a typical situation could involve a 64×64×64-voxel image with 60 views (of size 64×64) acquired around the object, resulting in a system matrix consisting of roughly 246,000×262,000 elements. Existence and uniqueness of a solution do not hold in general, as the measured data p are noisy, and the problem may be overdetermined (more equations than unknowns) or underdetermined (fewer equations than unknowns) depending on how the image and projection spaces are discretized. Thus, direct methods of solving the system are not feasible, and iterative approaches must be used.

An algebraic reconstruction technique (ART) is one that attempts to solve the system (1.3) by sequentially satisfying the constraints provided by the equations $c_j x = p_j$, where c_j is the j^{th} row of C, $j \in [1, JK]$. Often, ART refers specifically to the method of Kaczmarz [32], first proposed in 1937. This technique was most notably investigated for use in image reconstruction as it applies to electron microscopy and X-ray photography [24]. At the n^{th} iteration, the i^{th} component of the estimate is updated with the following formula:

$$x_i^{(n+1)} = x_i^{(n)} + \frac{C_{ji}}{\sum_{i'} C_{ji'}^2} \left(p_j - \sum_{i'} C_{ji'} x_{i'}^{(n)} \right), \tag{1.6}$$

where $n + 1 \mod JK = j$. At every iteration, $x^{(n)}$ is orthogonally projected onto the hyperplane defined by the equation $c_j x = p_j$, where j increases with every iteration, eventually returning to $j = 1$. If a unique solution exists, then ART converges to it after JK iterations; essentially finding the intersection of the JK hyperplanes defined by the system. Otherwise, it converges to one of many solutions (in the underdetermined case) or to a limit cycle (overdetermined case). In practice, ART is seldom used in SPECT image reconstruction since it converges slowly, requires access to rows of the system matrix (which is usually not stored due to its size) and does not account for the fact that the data are noisy.

Given that the data are noisy, the goal of image reconstruction is most appropriately viewed as finding the image x with the highest likelihood of producing the noisy data p, given the system model and an appropriate model for the distribution of the noise. Methods that take this approach are known as *statistical* reconstruction methods. Define

$$\hat{p} = Cx, \tag{1.7}$$

i.e., $\hat{p}$ represents the "true" data one would measure given an activity distribution x, in the absence of noise. Since nuclear decay is a Poisson process, the noise in the measurement data is most accurately modeled as Poisson noise. Then, the *likelihood*, $\mathcal{L}$, of measuring the noisy data p is given by the conditional probability:

$$\mathcal{L} = \text{Pr}(p|\hat{p}) = \prod_j \frac{e^{-\hat{p}_j}\hat{p}_j^{p_j}}{p_j!} \tag{1.8}$$

The value of $\hat{p}$ with the maximum likelihood of producing p can be found by finding the minimizer of the negative logarithm of $\mathcal{L}$:

$$\begin{aligned} -\log\mathcal{L} &= \sum_j \left[\hat{p}_j - p_j \log \hat{p}_j\right] + \text{constant} \\ &= \sum_j \left[\sum_i C_{ji}x_i - p_j \log \sum_i C_{ji}x_i\right] + \text{constant}. \end{aligned} \tag{1.9}$$

From this point forward we discard the constant term since it can be ignored for the purposes of minimization. Denote the contribution of voxel i to $\hat{p}_j$ by

$$\hat{p}_{ji} = C_{ji}x_i. \tag{1.10}$$

In practice we cannot make the analogous observation p_{ji}, since we are only capable of measuring the sum of all p_{ji}, namely p_j. This quantity is theoretically useful, however, since we can then express the log likelihood for a single image voxel as

$$-\log\mathcal{L}_i = \sum_j \left[C_{ji}x_i - p_{ji}\log C_{ji}x_i.\right] \tag{1.11}$$

Taking partial derivatives with respect to x_i then gives

$$-\frac{\partial}{\partial x_i}\log\mathcal{L}_i = \sum_j\left[C_{ji} - \frac{p_{ji}}{x_i}\right] \tag{1.12}$$

$$-\frac{\partial^2}{\partial x_i^2}\log\mathcal{L}_i = \sum_j \frac{p_{ji}}{x_i^2} \tag{1.13}$$

Since the right-hand side of (1.13) is always positive, this implies that the negative log likelihood is minimized when the right-hand side of (1.12) is zero; i.e., when

$$\sum_{j=1}^{J} C_{ji} = \frac{1}{x_i}\sum_j p_{ji}$$

$$x_i = \sum_j p_{ji}\bigg/\sum_j C_{ji}. \tag{1.14}$$

Since p_{ji} is unobservable, it must be estimated. The best estimate is obtained by taking p_j, which is the sum of the p_{ji}, and multiplying it by the ratio of $\hat{p}_{ji}$ to $\hat{p}_j$:

$$\begin{aligned} p_{ji} &= p_j\frac{\hat{p}_{ji}}{\hat{p}_j} \\ &= p_j\frac{C_{ji}x_i}{\sum_i C_{ji}x_i}. \end{aligned} \tag{1.15}$$

Substituting (1.15) into (1.14) then gives a fixed-point iteration for x_i:

$$x_i^{(n+1)} = x_i^{(n)}\frac{1}{\sum_j C_{ji}}\sum_j C_{ji}\frac{p_j}{\sum_{i'} C_{ji'}x_{i'}^{(n)}}. \tag{1.16}$$

This is the maximum likelihood expectation maximization (MLEM) algorithm for emission tomography, as first derived in [65]. Intuitively, MLEM can be viewed as a repetition of the following procedure:

1. The current estimate, $x^{(n)}$, is projected forward, i.e. multiplied by the system matrix C. This operation gives an estimate of what the measured projection data “would” look like for the current image estimate.

2. The ratio of each actual projection measurement p_j to the forward projected estimate from Step 1 is taken. Thus if the values in the forward projected estimate are lower than the corresponding measured values, the ratios will be greater than one; otherwise, the ratios will be less than one.

3. The ratios are backprojected into image space. This is equivalent to multiplying the vector of ratios from Step 2 by the transpose of C. This operation maps the ratios back into image space, so that each element $x_i^{(n)}$ in image space can be scaled by an appropriate factor.

4. Every backprojected ratio is normalized by dividing by $\sum_j C_{ji}$. If every column of C sums to one then this step is not necessary, but in general this is not the case. The normalization ensures that the values in x remain proportional to the measured data.

5. Finally, each normalized, backprojected ratio is multiplied by the corresponding value of $x^{(n)}$ to produce the new estimate $x^{(n+1)}$.

A well-known property of MLEM is that in the presence of noisy data, image quality begins deteriorating after a fairly small number of iterations [30]. Once the large-scale features of the image have been recovered, further iterations mostly fit the noisy distribution of emitted counts, rather than the underlying activity. To reduce this effect, MLEM is typically stopped after some pre-determined number of iterations, rather than being run until a convergence criterion is met. This approach is simple, but may result in image artifacts since the MLEM algorithm does not converge at the same rate in all regions of the image. An alternative approach includes a smoothing prior into the update formula, through the use of maximum *a posteriori* (MAP) reconstruction [25]. The MAP update is given by:

$$x_i^{(n+1)} = x_i^{(n)} \frac{1}{\sum_j C_{ji} + \beta \frac{\partial U(x^{(n)})}{\partial x_i}} \sum_j C_{ji} \frac{p_j}{\sum_{i'} C_{ji'} x_{i'}^{(n)}}. \tag{1.17}$$

Here $U(x)$ is an energy function which penalizes deviations between neighbouring image voxels, and β is a weighting term for the prior. Both U and β must be carefully chosen to avoid over-smoothing the image and losing fine detail.

An accelerated version of MLEM, known as ordered subsets expectation maximization (OSEM), is typically used in practice [28]. OSEM is identical to MLEM, except that every iteration of OSEM consists of several subiterations which act only on a subset, Ω_m, of the acquired projection data:

$$x_i^{(n+1)} = x_i^{(n)} \frac{1}{\sum_{j \in \Omega_m} C_{ji}} \sum_{j \in \Omega_m} C_{ji} \frac{p_j}{\sum_{i'} C_{ji'} x_{i'}^{(n)}}. \tag{1.18}$$

For instance, if the projection data consist of 64 views which are divided into four subsets, then Ω_1 would consist of every fourth view starting with the first view, Ω_2 of every fourth view starting with the second view, etc. One full iteration of OSEM over all four subsets thus requires roughly the same computation time as one iteration of MLEM; however, the image is typically of the same quality as one produced with four full MLEM iterations [30].

Finally, least-squares approaches are sometimes used to solve the image reconstruction problem as well [36]. In this case, the objective function to minimize is given by

$$g(x) = \frac{1}{2} \left\| p - Cx \right\|_2^2 , \tag{1.19}$$

rather than the negative log likelihood (1.9). This objective function can be derived by using a Gaussian likelihood model for the data p, rather than the Poisson model. Since Poisson noise is well-approximated by Gaussian noise at high count rates, this is a reasonable assumption in many cases. Approaches for solving least-squares problems are well-studied, and include methods such as conjugate gradient for least squares (CGLS) and the generalized minimum residual method (GMRES) [48]. One complication in using a generic least-squares method for image reconstruction is that such methods generally do not enforce non-negativity of the solution. Nonnegativity can be enforced through the inclusion of a penalty term in the objective function or by modifying the update formula in these algorithms; however, these approaches may adversely affect convergence of the algorithm or increase computation time [36]. MLEM-based approaches, in contrast, ensure non-negativity since the update of $x^{(n)}$ consists only of multiplication by strictly positive quantities.

1.2 Dynamic SPECT

In conventional SPECT reconstruction, the projections are assumed to be *consistent*; i.e., each projection corresponds to the same distribution of tracer, viewed from a different angle. In general, a static single-rotation SPECT reconstruction algorithm is able to accurately reconstruct an image if the total acquisition time is less than the effective (biological + physical) half-life, $T_{\frac{1}{2}}$, of the tracer. If the tracer kinetics are faster, then noticeable artifacts will be present in the image [6, 49, 51]. In cases where adjacent regions exhibit different washout rates (e.g., in healthy vs unhealthy tissue), the effect is even more severe [51, 42]. Thus, in conventional static SPECT imaging, it is important for the washout of the tracer to be slow relative to the acquisition time.

There are clinical applications, however, where rapid, dynamic behaviour of a tracer could be used as an indication of function within an organ or region of the body. Myocardial blood flow, renal filtration, and the binding of ligands and receptors in the brain, for instance, are all dynamic processes that can be imaged using nuclear medicine tracers. Several types of dynamic NM imaging are possible. In planar dynamic imaging, the dynamic behaviour of a single-photon emitting tracer is imaged using a stationary camera head, providing a time series of two-dimensional projections acquired from one angle. Regions of interest are then drawn over some portion of the image, and a *time activity curve* (TAC) showing the change in tracer concentration within that region over time is extracted. This TAC can then be fit to an appropriate model in order to obtain kinetic parameters, such as the rate of uptake or wash-out of tracer within that region.

Planar imaging only provides two-dimensional information, which cannot be reliably corrected for effects such as attenuation and organ overlap. A PET camera, on the other hand, is able to rapidly acquire three-dimensional dynamic information, due to its high sensitivity and the fact that it acquires data from all angles around the patient simultaneously. As a result, dynamic imaging using PET has been applied to many clinical situations, particularly imaging dynamic processes in the brain, such as cerebral blood flow and glucose metabolism, or the binding of ligands to targeted receptors. The dynamic images produced by PET can be analyzed using techniques such as compartmental modeling, to produce parametric maps which quantify the level of function in different regions of the imaged organ. While PET is ideally suited to dynamic studies, however, there are several challenges associated with its clinical use. These challenges include the high cost of PET equipment, and the need for a cyclotron to produce PET tracers. Thus, obtaining three-dimensional, dynamic information using a SPECT system is of considerable interest. Since views around the object are not acquired simultaneously by standard SPECT cameras, however, the issue of how to deal with inconsistent projection data must be addressed.

Approaches to dynamic SPECT imaging can be broadly categorized in several ways. Certain methods require the acquisition of data using multiple fast rotations of the camera, for instance, while others attempt to reconstruct a dynamic image from data acquired in the conventional way using a single slow camera rotation. Some methods attempt to reconstruct a four-dimensional time series of 3D images (time frames), from which TACs and kinetic parameters can be extracted afterward; others skip this step and extract TACs or kinetic parameters directly from the projection data. What follows is an overview of different proposed approaches to dynamic SPECT data processing and reconstruction. A more thorough review of dynamic SPECT principles, reconstruction approaches and applications has recently been presented in [26].

1.2.1 Fast-rotation approaches

Methods using conventional reconstruction algorithms

If the gamma camera completes a rotation around the patient in a time period that is relatively short compared to $T_{\frac{1}{2}}$, then the projection data acquired during this rotation can be considered consistent. So, if the camera rotates around the patient many times at sufficiently high speed, it can acquire multiple sets of consistent, 360° projection data, each of which can be used to reconstruct a 3D image using a conventional method such as OSEM. This procedure provides a set of independently reconstructed time frames which, taken together, form a 4D image. To accurately image a tracer with $T_{\frac{1}{2}}$ on the order of several minutes, for instance, a full set of projection data must be acquired over at most a minute in order to achieve satisfactory temporal resolution. This “fast rotation” is much quicker than the one used in a conventional “slow rotation” SPECT study, which is typically on the order of 15 to 30 minutes.

The fast-rotation approach has been used in many dynamic cardiac imaging studies using various tracers such as $^{99\mathrm{m}}$Tc-teboroxime [50, 72, 71], $^{99\mathrm{m}}$Tc-pertechnetate [9] and ^{123}I-BMIPP [45]. All of these studies used triple-head cameras, which allowed for the rapid acquisition of 360° of projection data by rotating each head only 120°. The time per rotation (i.e. the temporal resolution of the final dynamic image) varied from 5 seconds to two minutes in these studies. The effect of various factors on the accuracy of kinetic parameters extracted from from dynamic $^{99\mathrm{m}}$Tc-Teboroxime cardiac SPECT images using fast-rotation methods has been particularly well-studied [14, 77, 70, 61, 33]. In addition to cardiac imaging, the fast-rotation technique has also been applied to dynamic SPECT imaging of the lungs [74], brain [80], and kidneys [1, 47].

The fast-rotation approach suffers from several drawbacks. From a practical point of view, many clinical SPECT systems are not even capable of multiple fast rotations, as they are designed for conventional SPECT acquisitions. Images produced using this method also tend to be very noisy, as the increased rotation speed greatly diminishes the number of counts acquired in every rotation, reducing the signal-to-noise ratio. Using triple-head cameras helps to mitigate this problem, but these cameras are also not clinically prevalent. Finally, reconstructing each frame of the image separately using a static 3D algorithm does not enforce any temporal consistency on the resulting 4D image. Since each frame of the image is reconstructed independently, the temporal correlation between the activity distributions in every frame of the image is not considered during the reconstruction procedure.

Using interpolation to simulate fast-rotation data from a slow-rotation scan has also been proposed [52, 13]. If a dual-head camera makes two complete slow rotations around a patient, for instance, then projections of the object from a given angle are acquired at four different times. Projections corresponding to that angle for other time frames can then be approximated using time-weighted interpolation between the actual measured projections from that angle. This method produces images that are much less noisy than the fast-rotation approach, due to the improved count rate provided by slow rotation. The majority of the data used to produce the image is interpolated rather than actually measured, however, and thus the reconstructed image may not accurately reflect reality.

New camera systems, which make use of alternative camera geometries and improved detectors to increase camera sensitivity, have been developed in recent years and have strong potential for dynamic SPECT applications [22, 60, 23, 69]. Several of these systems feature multiple detectors arranged in a stationary or quasi-stationary manner around the patient, rather than a large rotating camera head. These cameras are able to acquire projections from multiple angles through the patient in a short time period, which can then be used to independently reconstruct 3D frames of a dynamic image, similarly to the fast-rotation method. At the present time, however, these systems are not yet widely available in clinics.

Methods using compartmental modeling

Extraction of kinetic parameters from dynamic SPECT images is often useful to assess function. Since the images produced by fast rotation methods are noisy and may contain artifacts, it is often preferable to estimate the parameters directly from the projection data, without reconstructing actual images. Direct estimation can be accomplished by first using a kinetic model to represent the transfer of radiotracer between the blood and various tissue types, and solving for the time-dependent concentration of radiotracer, $C_n(t)$, in each tissue type n as a function of the blood input function, $B(t)$. $B(t)$ is assumed to be known, usually either from blood sampling, or by extracting it from some part of the projection data assumed to contain mostly contributions from blood. A one-tissue compartmental model between $B(t)$ and each $C_n(t)$ is usually assumed, with transfer coefficient K_n to tissue from blood. Every measured projection is then assumed to be a linear combination of $B(t)$ and the $C_n(t)$, and after multiple rotations of the camera, the K_n between each tissue type and the blood is estimated by solving a system of difference equations.

This approach was first developed in [81] and tested on a small-scale 2D simulation, with later work focused on applying it to more complex and realistic situations [58, 59, 29]. With this method, an image is first reconstructed from summed projections using conventional OSEM, in order to obtain a spatial segmentation of the patient body into different tissue types. Then, the volume corresponding to each tissue type is forward-projected in order to ascertain which projection bins contain contributions from that volume, and the projections can be used to estimate the washout parameter from each tissue type.

More recently the direct estimation approach has been modified to include the use of B-splines to model the TACs for every tissue type in the model [56, 57]. Using this method, the estimation problem becomes a matter of determining the spline coefficients for every tissue type from the projection data, then fitting the resulting TAC to the compartmental model in order to estimate the washout parameters. This method has the advantage of being much more computationally efficient than the original one, especially as the total size of the projection data set becomes large.

A third approach that incorporates kinetic modeling is a 4D maximum *a posteriori* (MAP) algorithm using a compartmental model-based prior [34]. Unlike in direct estimation of kinetic parameters, this method does reconstruct a time series of 3D images. During reconstruction, the TACs in each voxel of the image are encouraged to conform to a compartmental model through the use of a prior term and a MAP-based iterative reconstruction algorithm.

Another method has focused on the extraction of TACs for each compartment from the projection data, rather than kinetic parameters [44]. This method uses a small-dimensional, orthogonal basis to model the kinetic behaviour of the tracer. The basis is derived by taking the singular value decomposition of a matrix consisting of a spectrum of exponential functions, then convolving the first few singular vectors with the (known) blood input function. As with the B-spline approach, the reconstruction problem is then to determine the coefficients corresponding to each basis function and tissue type.

The main advantages of these methods over those discussed in the previous section is that they include modeling of the dynamic behaviour of the tracer, thus exploiting the temporal correlation between time frames of the image. Additionally, kinetic parameter estimates obtained using these methods are not biased by image artifacts resulting from high noise levels or inconsistent projection data. As was the case with the methods of the previous section, however, most of these methods require cameras capable of multiple rotations around the patient, which may not be widely available. Use of fast rotations also results in data that is noisier than the data acquired using a conventional slow rotation.

1.2.2 Slow-rotation approaches

At the present time the vast majority of systems available in clinics are standard SPECT systems which are only capable of acquiring data over a single slow camera rotation. Dynamic SPECT imaging on these systems requires reconstructing an image from extremely inconsistent projection data, since in the majority of dynamic studies, the tracer distribution changes drastically during the acquisition period. Slow-rotation dynamic SPECT methods usually assume that the activity concentration in every image voxel changes with every projection view acquired by the camera. Thus, the number of time frames, K, in the 4D reconstructed image corresponds to the number of stops made by the rotating camera. The system representation of the data acquisition then changes from (1.3) to:

$$C'x' = p \tag{1.20}$$

Here p represents the same vector of measured projection data as in (1.3), but the activity vector x' and system matrix C' now have different dimensions. The vector x' represents a 4D distribution of activity, whose size is K times greater than x. As a result, C' is also enlarged, with K times as many columns as the static system matrix C. The components of C', however, are identical to those of C since the system geometry is the same; furthermore, the number of non-zero entries is the same since the activity in time frame k only contributes to the k^{th} projection. Consequently, C' is block-diagonal and very sparse (see Figure 1.7).

Standard SPECT effects such as patient-specific attenuation and depth-dependent collimator response can be incorporated into C', just as in the static case. Attenuation correction (AC) is particularly important for slow-rotation dynamic SPECT, since varying attenuation as the camera rotates around the patient produces the same effect on the projection data as actual tracer dynamics. For instance, without AC it is not possible to know whether a decrease in measured activity over several projections is due to tracer washout, or to an increase in the density or amount of material between the detector and the activity source. As will be discussed in Chapter 4, however, modeling attenuation in the system matrix is not sufficient to fully correct for its effects in slow-rotation dynamic SPECT.

Since the number of unknowns has increased K-fold from the static case, but the amount of data has remained the same, the problem is extremely underdetermined. There are infinitely many potential solutions x' that fit the data, the vast majority of which are physiologically meaningless. To obtain a meaningful solution, assumptions must be made in order to reduce the number of unknowns or constrain the behaviour of the activity. Several different approaches to this problem have been studied.

Methods using an exponential model

One early method [41, 7] proposed modeling the time-dependent activity in each voxel x'_i by dual exponential washout:

$$x'_i(t) = a_i e^{-\lambda_i t} + b_i e^{-\eta_i t} + c_i, \tag{1.21}$$

for some constants a_i, b_i, c_i, λ_i and η_i. Then, only five parameters have to be estimated for each voxel, rather than the activity concentration in all K time frames. Some disadvantages of this method include that it assumes a specific functional form for the activity in every voxel that may not be appropriate in reality; that it only models decaying activity, and that it requires nonlinear optimization to determine the λ_i and η_i, which increases the complexity of the calculation.

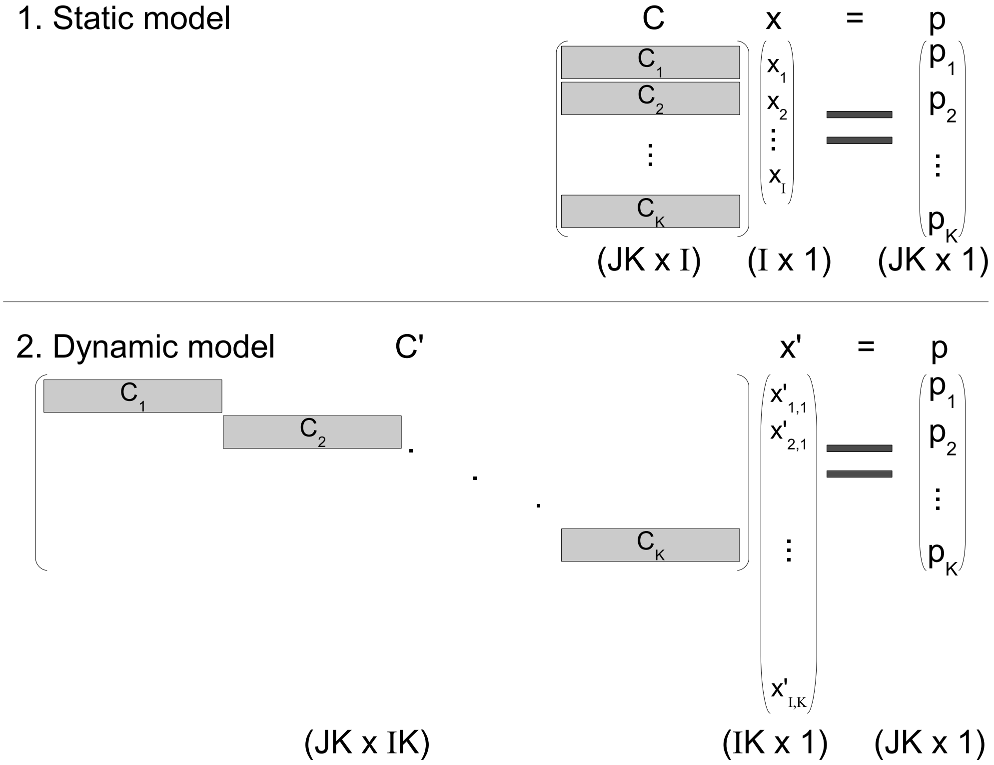

Figure 1.7: Change in system representation from static case (top row, equation (1.3)) to slow-rotation dynamic case (bottom row, equation (1.20)). The system matrix and activity vector are both enlarged, but the vector of projection data is unchanged. The dimensions of each matrix are given underneath it. In the above figure, each C_k is a $J \times I$ submatrix whose ji^{th} element gives the contribution of voxel i to projection bin j at time k, and each p_k is a vector of size J representing the counts detected in all J camera bins at time k.

This problem can be linearized by assuming instead that activity in every voxel consists of a sum of arbitrarily many decaying exponential terms [27]:

$$x_i'(t) = \int_0^\infty m_i(\lambda) e^{\lambda t} \, d\lambda \tag{1.22}$$

which yields a linear algebraic system of equations for the coefficients $m_i(\lambda)$ when discretized over λ. In addition to linearizing the problem, this approach has the advantage of eliminating the need to assume *a priori* how many exponential terms are needed to model the activity. It was later concluded, however, that a more general assumption of monotonically decreasing activity was more flexible and computationally simpler than an exponential model [3]. This led to the development of the dSPECT method, which is discussed later in this section.

Methods using factor analysis of dynamic structures

Factor analysis of dynamic structures (FADS), is an image decomposition method that is typically used to analyze an existing dynamic image, such as a time series of planar nuclear medicine scans, or a fully 4D dynamic image [2, 15]. The principle behind FADS is that the activity in every voxel of the image is composed of a linear combination of a small number of time-dependent factors. Least-squares optimization can then be used to determine the temporal behaviour of the different factors (encapsulated in a basis matrix F), as well as their coefficients in every image voxel (encapsulated in a coefficient matrix A). Extracting factors from an existing image can improve analysis of the image; for instance, by separating dynamic behaviour of the blood pool from that of the myocardium in ^{99m}Tc-Teboroxime cardiac SPECT studies [66], or removing contaminating activity due to the liver from these same studies [67].

The FADS method can also be incorporated into the actual reconstruction of images from projection data. Replacing the vector x' in (1.20) by the matrix product AF gives an inverse problem for determining appropriate values for these two matrices. These can be determined either simultaneously using a least-squares method [68], or using MLEM in an alternating fashion, by holding one of A or F fixed in every iteration [55].

In addition to providing a factor decomposition of the image immediately, the main advantage of the FADS approach is that it significantly reduces the number of unknowns to be estimated. The full problem of estimating the activity in every voxel at every time frame requires estimating IK unknowns; the FADS-based method requires estimating only $S(K+I)$, where S is the number of factors, typically no greater than 3 or 4. Some drawbacks of this approach are that it represents a considerable simplification of the actual physiology, that it may not be clear how many factors are necessary to accurately model the tracer dynamics, and that the factors determined by the method are not generally meaningful, due to nonuniqueness of the solution [55].

Methods using Kalman filtering

Some recent work has focused on using the recursive Kalman filtering algorithm [35] to estimate the dynamic distribution of activity based on slow-rotation data [37, 53]. In this approach, a first-order Markov chain model is used to model the time evolution of the tracer distribution. The dynamic image is then estimated from the projection data using the Kalman algorithm, which includes prediction, correction, and smoothing steps. Since Kalman filtering does not guarantee non-negativity of the solution, this condition must be added in some way. This can be accomplished by solving an optimization problem using non-negative least squares after the Kalman filtering step [37], or by incorporating regularization techniques such as Bregman projection [53]. The Kalman filtering approach has been tested on small, 2D simulations and provided reasonable results, but it has not yet been determined whether it is feasible for larger-scale, realistic clinical data.

dSPECT method

The dSPECT method arose as a generalization of the exponential model-based methods discussed earlier. Even if activity is decreasing exponentially, a more general assumption – namely, that the activity is monotonically decreasing – is computationally simpler, and provides comparable results [3]. Thus, the dSPECT algorithm [19] was originally formulated as a constrained linear least squares problem; namely, that of minimizing

$$f(x') = \left\{ \sum_{j,k} {\sigma_{j,k}}^{-2} \left(\sum_{i} C'_{ji,k} x'_{i,k} - p_{j,k} \right)^2 \right\}, \tag{1.23}$$

subject to the constraint

$$x'_{i,1} \geq x'_{i,2} \geq \ldots x'_{i,k} \geq 0 \quad \forall\, i \tag{1.24}$$

Here, $x'_{i,k}$ refers to the value of the i^{th} pixel at time frame k, $C'_{ji,k}$ is the system matrix element indicating the contribution of voxel i to projection bin j at time k, $p_{j,k}$ are the counts measured in projection bin j at time k, and $\sigma_{j,k}$ is a weighting factor determined from the variance in $p_{j,k}$. Although the projection data p is the same size as in the static case, here we explicitly index it by j and k to make the time dependence clear. The dSPECT method has been tested extensively with different acquisition protocols (e.g. dual and triple-head camera acquisitions) in simulations and physical phantom experiments [16, 12].

The constraint (1.24) is trivially adapted to the case of monotonically increasing activity, simply by reversing the order of the inequalities. Uptake and washout (increasing then decreasing activity) in a region, however, requires a more sophisticated approach. If the activity in voxel x'_i is known to peak in time frame t_i, then the constraint is given by:

$$0 \leq x'_{i,1} \leq x'_{i,2} \leq \ldots x'_{i,t_i} \geq x'_{i,t_i+1} \cdots \geq x'_{i,k-1} \geq x'_{i,k} \geq 0 \quad \forall\, i. \tag{1.25}$$

In general, however, the value of t_i is not known *a priori*. The original approach to determining t_i was to reconstruct two preliminary images, one assuming increasing activity in every voxel, the other assuming decreasing activity [18]. As it attempts to fit the data under these assumptions (which are known to be incorrect), dSPECT gives an indication of the true time-to-peak in every voxel (see Figure 1.8). This approach is time-consuming, however, and was replaced with one that allows the assumed peak location to be adjusted between iterations of the algorithm as it tries to fit the data [16]. This second approach is described in detail in Section 2.1.

dSPECT can also be applied using an expectation maximization (EM) approach, denoted dEM, which is similar to the MLEM algorithm (1.16). This approach provides comparable results to the CLS formulation (1.23) while being computationally simpler [17, 16]. An additional benefit of dEM is that positivity does not need to be included as a constraint, as it is inherent to the MLEM algorithm. The dEM formulation of the problem is given in Chapter 2, Equation (2.8).

Since the development of dSPECT, further studies have focused on modifications to the algorithm, and on its application to certain clinical situations. These studies have included incorporating depth-dependent resolution into the dynamic system matrix [20], including additional regularization to improve image quality [43, 5], implementing dSPECT using sophisticated nonlinear optimization software [4], and unifying dSPECT with gated SPECT

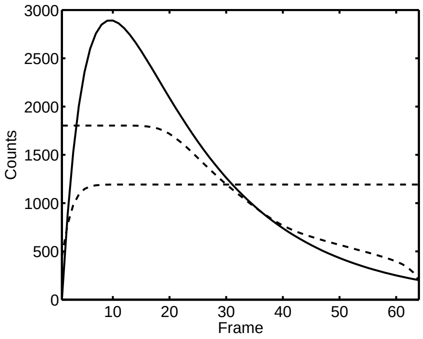

Figure 1.8: Illustration of the original dSPECT method for finding time-to-peak, from a simple phantom experiment. The true TAC for a region of interest in the phantom is shown as a solid line, with dashed lines showing TACs obtained from reconstructed images assuming increasing behaviour (lower dashed curve) and decreasing behaviour (upper dashed curve). Both dashed TACs are essentially flat during the sixth to eighteenth time frames, indicating that the true peak occurs somewhere in that interval.

to account for cardiac motion and produce 5-dimensional (5D) images [31, 21]. Clinical applications that have been studied include using dSPECT to assess renal function [11], and to reduce artifacts caused by high bladder uptake in pelvic SPECT imaging [78].

Chapter 2

Concavity-constrained dSPECT reconstruction

Since dynamic tracer behaviour within the body arises as a result of continuous physiological processes, we expect that the time activity curves (TACs) in a given region of interest (ROI) should be fairly smooth, provided adequate temporal sampling. While the dSPECT constraint – namely, that activity in every voxel must either increase, decrease, or increase to a maximum value and then decrease – does eliminate many nonphysical solutions, it does not force the TAC in every voxel to be smooth. As a result, TACs with unphysical behaviour, such as sharp spikes, may be present in images reconstructed using dSPECT. In this chapter we develop a modification to dSPECT which, instead of acting on the first derivative of the TAC in every voxel, constrains the second derivative. The method, which we denote d^{2}EM, guarantees smoother TACs than dSPECT through the use of this stronger constraint. The use of a concavity-based constraint was previously proposed in [16], but not implemented.

We first review details on the implementation of dSPECT, and specifically its EM-based formulation, dEM. These details are necessary to understand the implementation of d^{2}EM. We then discuss the design and implementation of the new method.

2.1 Implementation of dEM

In dSPECT, the TAC in every voxel is only permitted one of three behaviours: strictly increasing, strictly decreasing, or increasing to a maximum value and then decreasing. This behaviour is enforced through the use of a *difference tensor*, denoted by A. By acting on the dynamic image vector x' (see (1.20)), A defines a new vector:

$$\tilde{x} = Ax'. \tag{2.1}$$

The vector $\tilde{x}$, which has the same dimensions as x', consists of differences in activity between successive time frames, for each voxel. The key mechanism behind dSPECT is that if every element of $\tilde{x}$ is held positive, then the inverse mapping from $\tilde{x}$ to x', A^{-1}, controls the temporal behaviour of x'. For instance, if one wishes to enforce strictly increasing activity on voxel x'_i, the block of A corresponding to x'_i is a $K \times K$ matrix given by

$$A_i = \begin{pmatrix} 1 & & & \\ -1 & 1 & & \\ & \ddots & \ddots & \\ & & -1 & 1 \end{pmatrix}. \tag{2.2}$$

Let $x'_{i,k}$ denote the value of voxel i at time frame k, and correspondingly for $\tilde{x}_{i,k}$. Then, since $\tilde{x}_i$ contains only positive values, the inverse mapping A_i^{-1} ensures that $x'_{i,1} > 0$, $(x'_{i,2} - x'_{i,1}) > 0$, etc., giving the desired increasing behaviour. Note that A_i also maps $\tilde{x}_{i,1}$ to $x'_{i,1}$, making it the only element of $\tilde{x}_i$ that is not a first difference value. This mapping guarantees that the TAC for voxel i is non-negative, and provides a one-to-one correspondence between $\tilde{x}_i$ and x'_i.

Decreasing behaviour in voxel i is enforced using a similar matrix; $x'_{i,K}$ is held positive as well as the negative first differences $x'_{i,K-1} - x'_{i,K}$, etc.:

$$A_i = \begin{pmatrix} 1 & -1 & & \\ & \ddots & \ddots & \\ & & 1 & -1 \\ & & & 1 \end{pmatrix}. \tag{2.3}$$

For increasing-then-decreasing behaviour in voxel i, with peak activity occurring in time frame $k \in [2, K-1]$, the following tensor is used:

$$A_i = \begin{pmatrix} 1 & & & & & & \\ -1 & 1 & & & & & \\ & \ddots & \ddots & & & & \\ & & -1 & 2 & -1 & & \\ & & & & \ddots & \ddots & \\ & & & & & 1 & -1 \\ & & & & & & 1 \end{pmatrix}, \tag{2.4}$$

where the k^{th} row contains the three entries -1,2 and -1 in the $(k-1)^{\text{th}}$, k^{th} and $(k+1)^{\text{th}}$ columns, respectively. This matrix enforces increasing behaviour in all frames earlier than k, and decreasing behaviour in all frames later than k. At frame k, we have:

$$\tilde{x}_{i,k} = -x'_{i,k-1} + 2x'_{i,k} - x'_{i,k+1}, \tag{2.5}$$

which, when solved for $x'_{i,k}$, gives

$$x'_{i,k} = \frac{1}{2}\left(x'_{i,k-1} + x'_{i,k+1}\right) + \frac{1}{2}\tilde{x}_{i,k}. \tag{2.6}$$

That is to say, $x'_{i,k}$ is the average of $x'_{i,k-1}$ and $x'_{i,k+1}$, plus some value specified by $\tilde{x}_{i,k}$. As a result, the maximum value of the TAC corresponding to voxel i may actually occur in frame $k-1$, k **or** $k+1$, depending on the magnitude of $\tilde{x}_{i,k}$. The actual constraint being enforced is that the TAC be concave-down at point k – thus preventing $x'_{i,k}$ from being the smallest of the three values, which would violate the dSPECT constraint.

This condition provides a mechanism by which the assumed peak time can shift between iterations of the algorithm. For instance, suppose the maximum value of x'_i was assumed to occur in frame k, but after updating $\tilde{x}$ and mapping back to x', we find that the maximum value of x'_i occurs in frame $k+1$. Then, for the next iteration, the peak is assumed to occur in frame $k+1$. After the next update of $\tilde{x}$, the assumed peak location can be shifted again (e.g. to frame $k+2$).

This is an important feature because the time of peak activity for each voxel is not known *a priori*. Some initial assumption about the time of peak activity in every voxel is made, and the assumed peak times for each voxel are then adjusted based on the projection data between every iteration of the algorithm. This is the second approach to determining the time of peak activity, as opposed to the first one discussed in the previous chapter (see Figure 1.8). It has the advantage of allowing peak times to be adjusted between every iteration of the algorithm, rather than requiring multiple runs of the dEM algorithm using different assumptions.

Combining (1.20) and (2.1) gives the following system model:

$$C' A^{-1} \tilde{x} = p, \tag{2.7}$$

The update formula for dEM is then analogous to (1.16):

$$\tilde{x}_{i,k}^{(n+1)} = \frac{1}{\sum_j \left(C'_{ji,k} A^{-1}_{i,k} \right)} \tilde{x}_{i,k}^{(n)} \sum_j C'_{ji,k} A^{-1}_{i,k} \frac{p_{j,k}}{\sum_{i'} C'_{ji',k} A^{-1}_{i',k} \tilde{x}^{(n)}_{i',k}} \tag{2.8}$$

with all terms defined as in (1.23). This iterative formula is essentially the same as the update formula for MLEM reconstruction of static images, with the combined dynamic system matrix and difference tensor $C' A^{-1}$ used in place of the static system matrix C. One key difference from MLEM is that not only the solution vector $\tilde{x}$, but also the matrix A^{-1} may change at every iteration of the algorithm. This has implications for the convergence of the algorithm, as will be shown in Section 3.3 of the next chapter.

The dEM algorithm must typically be run for a large number of iterations (between 50 and 100) before converging to a satisfactory solution. This is due to the fact that the the algorithm must determine the location of peak activity in every voxel as well as the activity intensity in every time frame, making the reconstruction problem more challenging than that of conventional static SPECT. Furthermore, the OSEM acceleration cannot be employed since the projections are inconsistent. Thus the full set of projection data must be used at every iteration of the algorithm [17].

2.2 Design of d^{2}EM

The second derivative constraint imposed by d^{2}EM should have the following properties:

1. The intent is to impose a stronger constraint than dEM; thus, the permitted TACs should be a subset of those permitted by dEM. In other words, it should not be possible to generate a solution in d^{2}EM that violates the dEM constraint.

2. The concavity of the TAC must be allowed to change once, as forcing TACs to be either concave-up or concave-down only is too restrictive. Allowing the second derivative to change sign once could allow the first derivative to change sign twice, however, which would violate the dSPECT constraint. Therefore, only TACs where the first derivative also changes sign at most once can be permitted.

3. The second derivative of the TAC should be able to change sign from positive to negative (concave-up to concave-down) as well as from negative to positive. This is in contrast to dSPECT, which only allows the first derivative to change sign from positive to negative.

4. The constraint should be imposed in the same way as in dEM, using a tensor denoted by B. The d^{2}EM algorithm will optimize over the vector

   $$\tilde{\tilde{\mathrm{x}}} = Bx'. \tag{2.9}$$

   The update formula will then be analogous to (2.8):

   $$\tilde{\tilde{\mathrm{x}}}_{i,k}^{(n+1)} = \frac{\tilde{\tilde{\mathrm{x}}}_{i,k}^{(n)}}{\sum_j \left(C'_{ji,k} B_{i,k}^{-1}\right)} \sum_j C'_{ji,k} B_{i,k}^{-1} \frac{p_{j,k}}{\sum_{i'} C'_{ji',k} B_{i',k}^{-1} \tilde{\tilde{\mathrm{x}}}_{i',k}^{(n)}}. \tag{2.10}$$

Figure 2.1 shows the general shapes of all possible TACs whose concavity changes at most once, and indicates whether each type will be permitted or prohibited by d^{2}EM. Most TAC shapes are prohibited because the first derivative changes from negative to positive, which violates the dSPECT constraint. Shapes M and P cannot be allowed in d^{2}EM for reasons that will be explained later, despite being valid TACs in dSPECT.

2.3 Implementation of d^{2}EM

Recall that TAC for voxel x'_i consists of K time frames, where K is the number of stops made by the camera. In dEM, for increasing or decreasing behaviour, the corresponding K-vector $\tilde{x}_i$ consists of $K-1$ first differences, and one additional value ($x'_{i,1}$ or $x'_{i,K}$, respectively) to ensure positivity and provide a one-to-one mapping between x'_i and $\tilde{x}_i$. For peaking activity, $\tilde{x}_i$ contains $(K-3)$ first differences, one second difference value at the

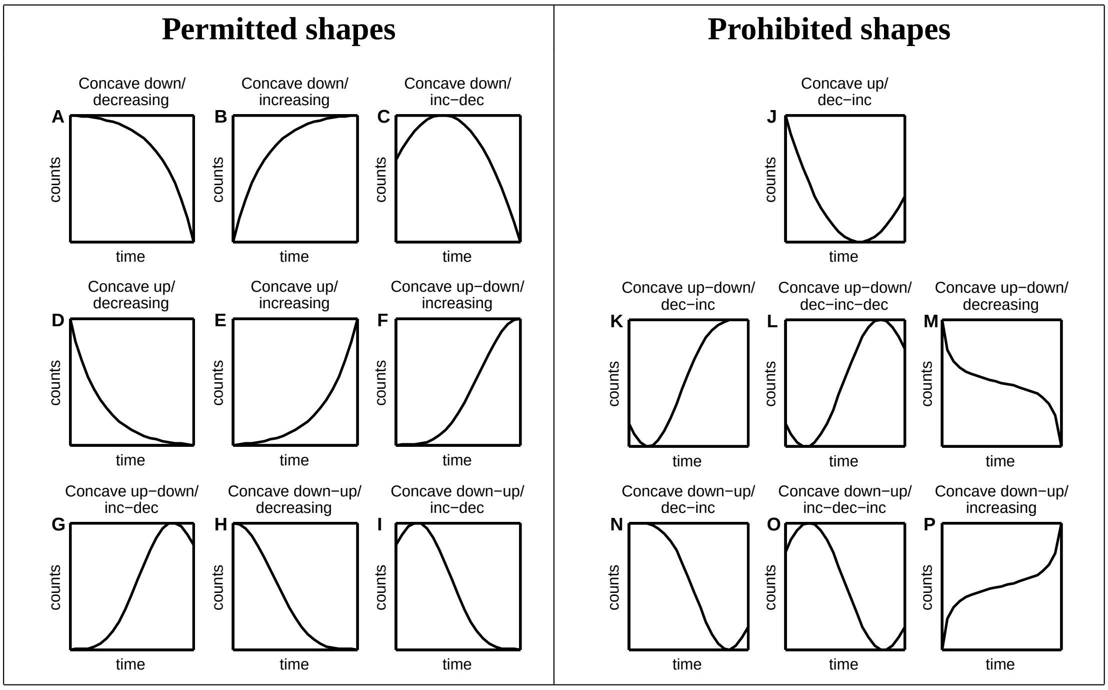

Figure 2.1: General shapes of all TACs which change concavity at most once, grouped by whether or not they should be permitted by d^{2}EM.

assumed peak location, and the voxel activity values at the first and last time frame. In this case, since the derivative changes sign at an interior timeframe, it is necessary to store both endpoint voxel values to ensure positivity of the TAC.

Analogously, the vector $\tilde{\tilde{\mathrm{x}}}_i$ in d^{2}EM will include $(K-2)$ second difference values in cases where the concavity does not change, and $(K-4)$ second differences and one third difference if it does. The vector can therefore include two other values in the first case, and three in the second case. These values will be chosen specifically to preserve positivity and enforce the desired TAC shapes illustrated in Figure 2.1.

2.3.1 Tensor construction

A concave-down curve can be either increasing, decreasing, or increase and then decrease (shapes A, B and C in Figure 2.1). Downward concavity can be enforced by storing the negative second difference at each point in $\tilde{\tilde{\mathrm{x}}}_i$:

$$\tilde{\tilde{\mathrm{x}}}_{i,k} = -x'_{i,k-1} + 2x'_{i,k} - x'_{i,k+1}, \qquad k \in [2, K-1] \tag{2.11}$$

To ensure positivity of the TAC, it is sufficient to store the two endpoint values $x'_{i,1}$ and $x'_{i,K}$ in $\tilde{\tilde{\mathrm{x}}}_i$, since a concave-down curve cannot lie below the secant line connecting the two endpoints. So any of shapes A, B or C can be enforced in voxel x'_i by the $K \times K$ tensor block B_i:

$$B_i = \begin{pmatrix} 1 & & & & \\ -1 & 2 & -1 & & \\ & \ddots & \ddots & \ddots & \\ & & -1 & 2 & -1 \\ & & & & 1 \end{pmatrix} \tag{2.12}$$

Unlike in dEM, the location of the peak activity is not stored explicitly. Whether the concave-down curve is increasing, decreasing, or peaking at an intermediate time frame is determined by the relative magnitudes of the values in $\tilde{\tilde{\mathrm{x}}}_i$.

A similar construction cannot be used for a concave-up curve, since the prohibited shape J can occur even if both endpoints are held positive. Instead, the concave-up decreasing and concave-up increasing cases (shapes D and E) are treated separately. Concave-up increasing behaviour is enforced by forcing $x_{i,1}$ and $x_{i,2} - x_{i,1}$ (the first difference at the earliest timeframe) to be positive, as well as all second difference values (2.13). Concave-up decreasing behaviour is enforced by imposing similar conditions at the last time point (2.14).

$$B_i = \begin{pmatrix} 1 & & & & \\ -1 & 1 & & & \\ 1 & -2 & 1 & & \\ & \ddots & \ddots & \ddots & \\ & & 1 & -2 & 1 \end{pmatrix} \tag{2.13}$$

$$B_i = \begin{pmatrix} 1 & -2 & 1 & & \\ & \ddots & \ddots & \ddots & \\ & & 1 & -2 & 1 \\ & & & 1 & -1 \\ & & & & 1 \end{pmatrix} \tag{2.14}$$

For the case where the TAC is initially concave-up and later concave-down (denoted *concave-up-down*), shapes F and G are permitted, while shapes K, L and M are not. Both shapes F and G can be enforced by forcing the activity values at both endpoints, as well as the first difference at the earliest timeframe, to be positive. Doing so ensures positivity of the TAC, since it must increase initially and cannot decrease below the endpoint at the latest timeframe. Finally, shapes K, L and M are prevented from occurring, since all three have a negative first derivative at the first timeframe. Thus, the following tensor block is used to enforce concave-up-down behaviour:

$$B_i = \begin{pmatrix} 1 & & & & & & & \\ -1 & 1 & & & & & & \\ 1 & -2 & 1 & & & & & \\ & \ddots & \ddots & \ddots & & & & \\ & & 1 & -3 & 3 & -1 & & \\ & & & & \ddots & \ddots & \ddots & \\ & & & & & -1 & 2 & -1 \\ & & & & & & & 1 \end{pmatrix} \tag{2.15}$$

The change in concavity occurs at the k^{th} time frame, where row k contains the entries 1, -3, 3 and -1 in the $(k-2)^{\text{th}}$ to $(k+1)^{\text{th}}$ columns, respectively. As with the tensor for the peaking TAC (2.4) in dEM, this construction allows the actual inflection point to occur either in the $(k-1)^{\text{th}}$, k^{th} or $(k+1)^{\text{th}}$ frame. Between iterations of d^{2}EM, the first derivative values in each of these frames can be checked, and the assumed location of the inflection point shifted to the frame with the maximum first derivative value.

Note that both shapes L and M are concave-up-down, and decreasing at both endpoints. As a result, it is not possible to differentiate between these two shapes by constraining only the endpoint behaviour. This is why shape M is prohibited even though it does not violate the dEM constraint; it is not possible to prevent it from assuming shape L without a more cumbersome restriction on values of $\tilde{\tilde{\mathrm{x}}}_i$ other than the endpoints.

A TAC that changes from concave-down to concave-up (*concave-down-up*) can be enforced using a mirror version of tensor (2.15):

$$B_i = \begin{pmatrix} 1 & & & & & & & \\ -1 & 2 & -1 & & & & & \\ & \ddots & \ddots & \ddots & & & & \\ & & -1 & 3 & -3 & 1 & & \\ & & & & \ddots & \ddots & \ddots & \\ & & & & & 1 & -2 & 1 \\ & & & & & & 1 & -1 \\ & & & & & & & 1 \end{pmatrix} \tag{2.16}$$

This tensor allows shapes H and I while preventing shapes N, O and P from occurring. Shape P is forbidden for the same reason as shape M in the concave-up-down case.

The d^{2}EM update formula (2.10) requires inverting the tensor B. In dEM, since the tensor A is essentially bidiagonal in all cases, inverting A involves only forward or backward solving for entries in x'. In d^{2}EM, the tensor B is either triangular (2.13 and 2.14), tridiagonal (2.12), or tetradiagonal (2.15 and 2.16). B can, therefore, be inverted easily using forward or backward solving for the triangular matrices, Crout factorization [10] for the tridiagonal matrices, or a combination of these for the tetradiagonal matrices.[1]

2.3.2 Transition rules

Both dEM and d^{2}EM impose shape constraints on the TACs in every voxel through the use of the difference tensor. Since it is not known *a priori* which TAC shape is the correct choice for a given image voxel, the tensor must be adjusted in between iterations of the algorithm, in order to find the best fit to the data. As mentioned previously, in dEM this is accomplished by allowing the assumed time of peak activity to be adjusted in between iterations. This adjustment is possible because of the form of the tensor (2.4), which allows the activity in a voxel to peak one frame earlier or later than the assumed time. Through this mechanism, the assumed behaviour can shift through the entire spectrum of behaviours permitted by dSPECT, from decreasing (maximum activity in the first time frame) to increasing (maximum activity in the last time frame), as illustrated in Figure 2.2. Strictly

---

[1] Crout factorization was implemented using code provided by the authors of [10] at `http://www.as.ysu.edu/~faires/Numerical-Analysis/DiskMaterial/index.html`.

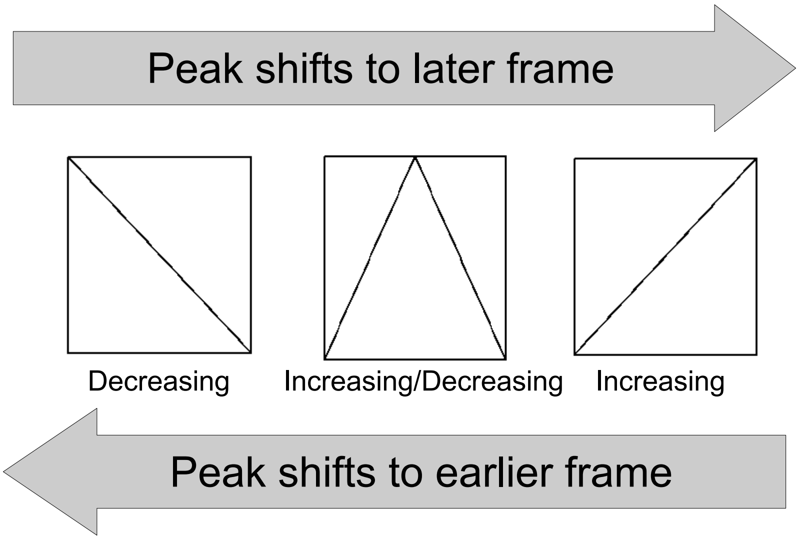

Figure 2.2: Range of possible TAC shapes in dEM, from decreasing (activity peaks in first time frame), to increasing/decreasing (activity peaks in intermediate time frame) to increasing (activity peaks in last time frame).

speaking, the tensors for increasing and decreasing activity (Equations (2.2) and (2.3), respectively) are not necessary, since all behaviours can be achieved with tensor (2.4). They are useful, however, if one does know beforehand that activity should *only* be increasing or decreasing, and wishes to impose that constraint on the solution without allowing the constraint to change.

For d^{2}EM, the situation is somewhat more complicated because there is a wider range of constraints that can be imposed, as indicated by the need for the five different tensors (2.12) to (2.16). In order for the algorithm to be robust, there must be a mechanism by which the assumed behaviour of the TAC in any voxel can be adjusted from the current assumed shape to any of the other basic curve constraints. For example, if the behaviour in a voxel is initially assumed to be concave-down, but the true activity is concave-up increasing, then over some number of iterations, there must be a way for the algorithm to recognize that the current assumption of concave-down behaviour for that voxel is not correct, and to adjust the tensor accordingly until it attains concave-up increasing behaviour. We now discuss how this adjustment can be achieved.

In the concave-down-up state (2.16), the TAC is initially concave-down, then becomes concave-up at an inflection point in some time frame k between 2 and $(K-1)$. As discussed previously, the location of the inflection point in any voxel with concave-down-up behaviour can be shifted one frame earlier or one frame later after every iteration, based on the data. If the inflection point shifts earlier and earlier until $k=2$, then the TAC is almost entirely concave-up, as well as decreasing since the tensor (2.16) forces it to be decreasing at the last time frame. Thus, if the inflection point shifts to $k=2$, this suggests that the TAC should be concave-up and decreasing, and so the assumed shape for that voxel can be changed by using tensor (2.14). Conversely, if the inflection point shifts until it reaches the last possible time frame, $k=(K-1)$, the TAC is now almost entirely concave-down, suggesting that concave-down behaviour (2.12) is the most suitable assumption.

Similarly, in the concave-up-down state, the inflection point can shift over to $k=2$, resulting in a curve that is almost entirely concave-down, or to $k=(K-1)$, resulting in a curve that is almost entirely concave up and increasing. As illustrated in Figure 2.3, these transitions suggest that there are two “branches” of behaviour, connected through the concave-down state. To complete the picture, however, we need to define rules to allow transitions from the concave-down, concave-up increasing and concave-up decreasing states as well. Since there is no inflection point in any of these states, we must judge whether a transition to a different state should occur based on the magnitude of the concavity at either end of the TAC.

As an example, suppose the TAC in a voxel is assumed to be concave-down, but the true activity curve is concave-down-up. As d^2EM attempts to fit the data under the incorrect assumption, the concavity of the TAC in the later time frames will approach zero, since the true activity curve is concave-up during this time period. Thus, if the concavity in the late time frames is tending to zero, this is an indication that the assumed behaviour should be changed to concave-down-up. A similar argument can be made to define a transition from the concave-down state to concave-up-down, if concavity tends to zero in the early time frames. Transitions from concave-up-increasing behaviour to concave-up-down (if concavity in late time frames tend to zero) and from concave-up-decreasing to concave-down-up (if concavity in early time frames tends to zero) complete the diagram, tying all five shape constraints together and allowing transitions between all of them. Figure 2.4 shows this completed transition diagram.

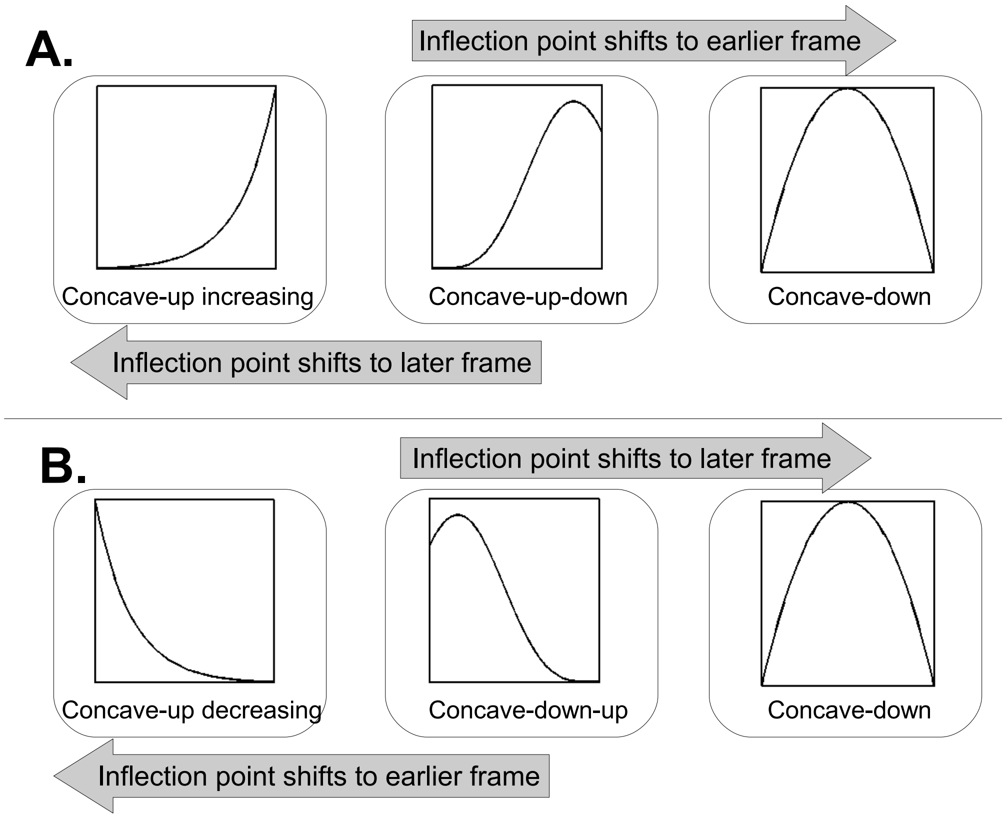

Figure 2.3: Illustration of how the assumed shape can be adjusted based only on the shifting of the inflection point, for the concave-up-down (**A**) and concave-down-up (**B**) states.

One disadvantage of this scheme is that it may take a large number of iterations before the algorithm determines the correct shape, if the initial assumption is incorrect. For instance, if the TAC in a voxel is initially assumed to be concave-down-up, but the true TAC is concave-up-increasing, then the assumed shape has to pass through the concave-down and concave-up-down states before arriving at the correct shape. Furthermore, the transitions out of the concave-down, concave-up-increasing and concave-up-decreasing states require defining some tolerance at which the concavity of the curve is considered to be “tending to zero,” since in practice the concavity values in $\tilde{\tilde{\mathrm{x}}}$ can become only arbitrarily small. It may take many iterations before the concavity at either end of the TAC becomes small enough to justify changing the assumption. Performing many iterations is problematic in terms of

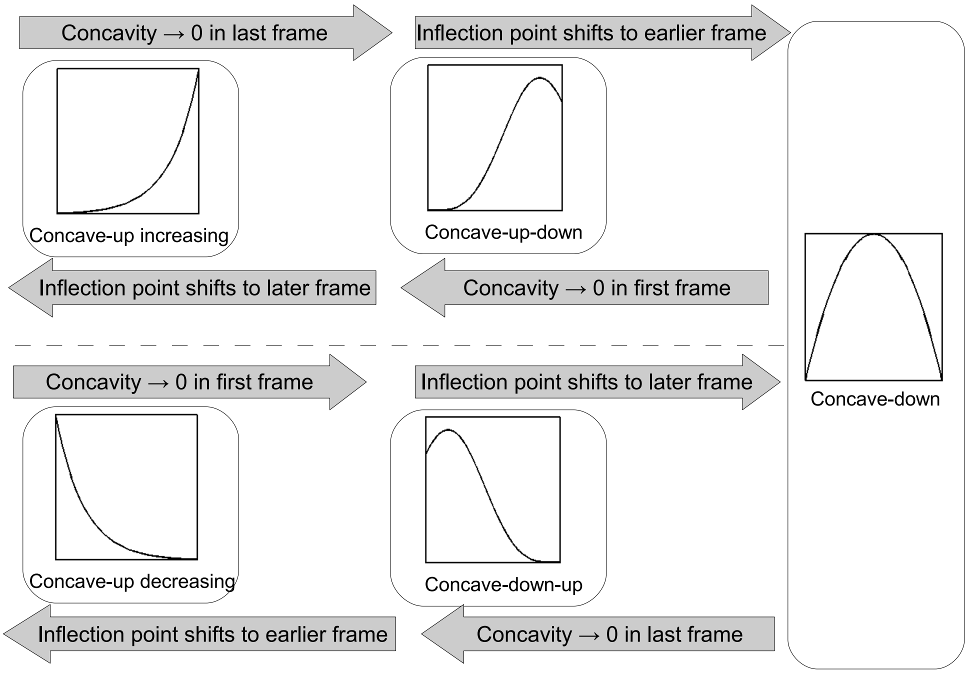

Figure 2.4: Full diagram of transitions between five d^2EM shape constraints. In the concave-down-up and concave-up-down states, the inflection point can shift earlier or later until reaching one of the other three shapes. From the concave-down, concave-up-increasing and concave-up-decreasing states, the concavity at one or both end frames of the TAC is examined to determine whether changing the assumption is justified.

image quality as well as computation time, as it amplifies the noise in the image.

To avoid these potential issues, an alternative transition scheme is possible, where the concave-down, concave-up-increasing and concave-up-decreasing states are omitted. Omitting these three states does not reduce the range of shapes permitted by d^2EM, since these shapes can be obtained under the constraints for concave-up-down and concave-down-up behaviour (tensors (2.15) and (2.16), respectively) as well. For instance, if the time of inflection under the concave-down-up assumption occurs at the earliest possible time, it is possible for the curve to be concave-up-increasing. The modified scheme, illustrated in Figure 2.5, eliminates the need for transitions based on examining the concavity of the curve, and should allow d^2EM to determine the correct curve shape more quickly. In Section 3.4 of the next chapter, we will compare the two transition schemes to see which is

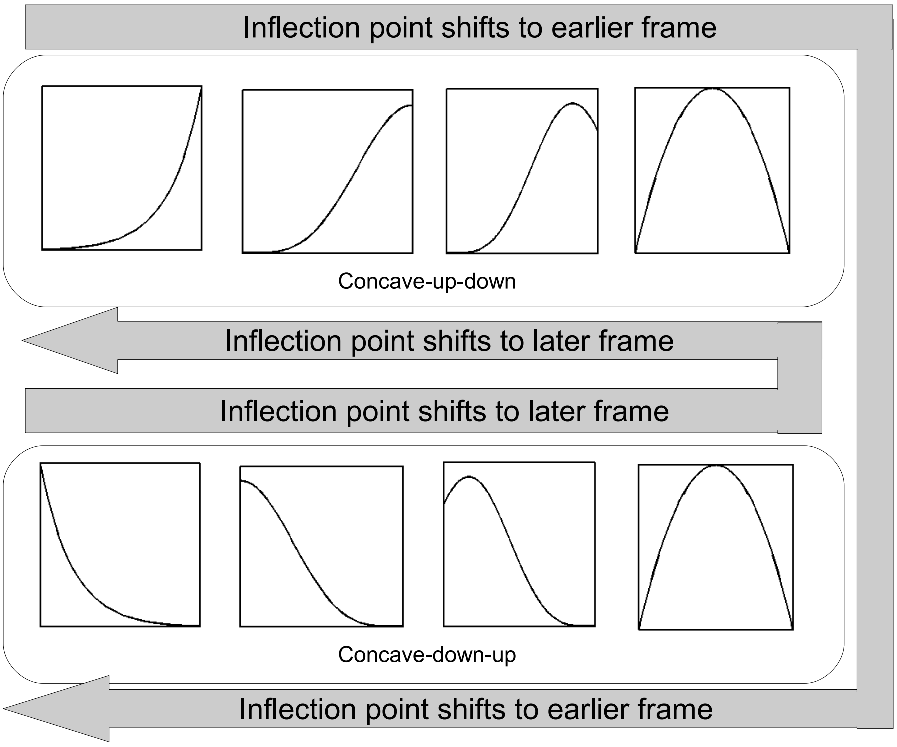

Figure 2.5: Alternate d^{2}EM transition diagram in which only the concave-down-up and concave-up-down tensors are used.

more effective.

Chapter 3

Experimental validation of d^{2}EM

In this chapter we assess the performance of d^{2}EM against dEM using simple, 2D digital phantom simulations. A digital phantom is a computerized image mimicking the distribution of tracer inside a sensibly modeled object. Once the phantom has been created, it can be used to generate simulated projection data, which is then input to a reconstruction algorithm to produce a reconstructed image. Phantom simulations are useful because the accuracy of the reconstructed image can be assessed by directly comparing it to the truth (i.e. the original phantom), which is not possible with real-life data. Furthermore, digital phantom simulations allow a fine level of control over different experimental parameters, such as the acquisition protocol used to acquire the projection data, the level of noise in the data, and the kinetic behaviour of the phantom.

In this chapter, two-dimensional phantoms were used to limit computation time, so that the performance of d^{2}EM could be tested for a wide range of kinetic behaviours and experimental conditions, and so that convergence could be examined over a large number of iterations. These simulations represent a considerable simplification of real-life situations, since the phantoms consisted of simple, 2D geometries with spatially uniform dynamic regions. In Chapter 5, dEM and d^{2}EM will be assessed using more realistic 3D phantom experiments, as well as two sets of real-life dynamic renal data. Analyzing these experiments requires discussion of some additional considerations, however; particularly those related to the impact of attenuation and collimator blurring on slow-rotation dynamic SPECT reconstruction. This discussion takes place in Chapter 4. Consequently, neither attenuation nor collimator blurring were modeled in any of the simulations presented in this chapter.

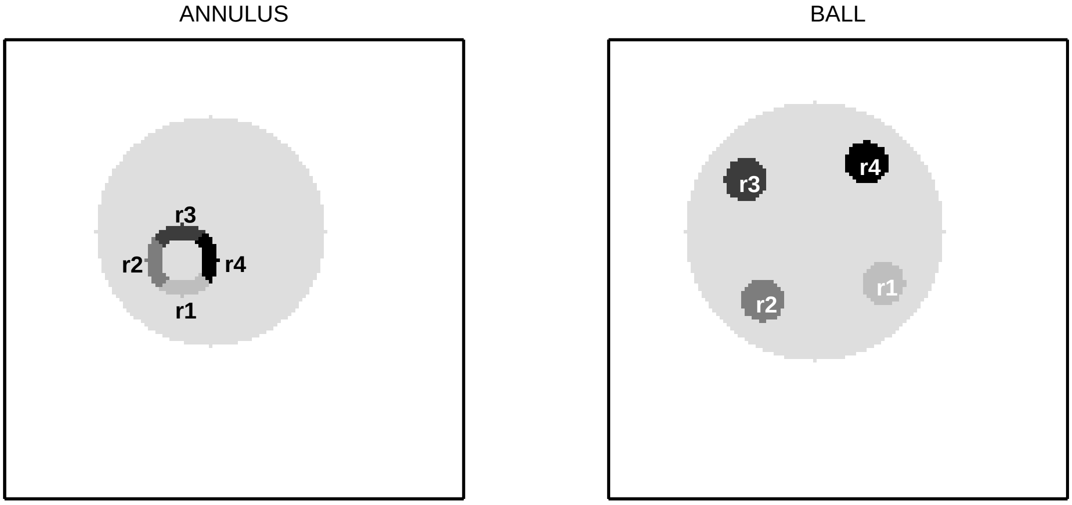

Figure 3.1: Geometry of 2D annulus (left) and ball (right) phantoms. Dynamic regions are labeled from r1 (Region 1) to r4 (Region 4). Large, light grey circle indicates the region of background activity.

3.1 Phantom construction

Two phantom geometries were used in these experiments, both consisting of a 128×128 voxel dynamic image with 64 time frames. The first geometry consisted of an annulus divided into four regions of equal size. The annulus had an outer radius of 10 voxels and thickness of 4 voxels. It was located off-centre within a circular region of radius 32 voxels, which was filled with low-level, constant background activity. The annulus shape was chosen because it is similar to a short axis slice through the myocardium. The second geometry consisted of four separate circular regions (balls), each with a radius of 6 voxels, arranged in a circle. These four regions were also situated in a circular region of background activity. The ball geometry modeled the situation of distinct, well-separated dynamic regions, as would be seen in dynamic imaging of the kidneys, for instance. Images of the both geometries are shown in Figure 3.1, with the four dynamic regions labeled. The dynamic regions were arranged asymmetrically to add further complexity to the simulation.

Each of the four regions in these two geometries featured different simulated tracer kinetics, modeled by a simple curve. In order to test a wide range of kinetic situations, three

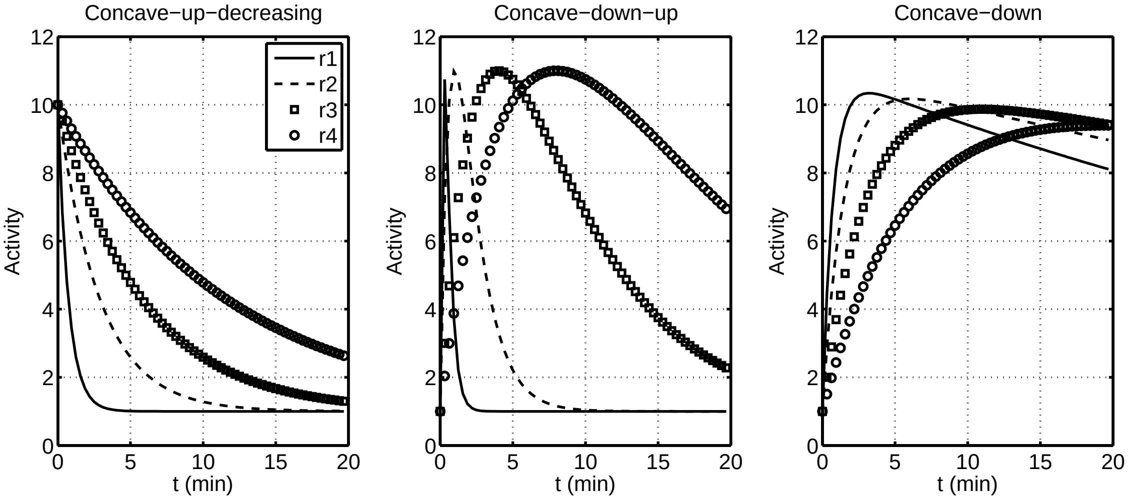

Figure 3.2: The twelve kinetic behaviours used in the 2D phantom simulations. Concave-up-decreasing shapes shown in left plot, concave-down-up shapes in middle plot, concave-down on right. For each category of behaviour, kinetics ranged from fast (r1) to slow (r4).

general categories of time activity curve were defined: concave-up-decreasing, concave-down-up, and concave-down, corresponding to the different curve models shown in Figure 2.4. Concave-up-increasing and concave-up-down behaviour were not simulated, since they are essentially mirror images of concave-up-decreasing and concave-down-up behaviour, respectively.

For each of these three categories of behaviour, four curves ranging from fast to slow kinetics were created, giving a total of 12 different TACs. The fastest-changing curve was always assigned to Region 1, and the slowest to Region 4. The 12 curves are illustrated in Figure 3.2, and the functions and parameters used to generate the curves are given in Table 3.1. The curves were defined for a simulated time interval of 0 to 20 minutes. Every voxel in each of the four dynamic regions of the phantom was then assigned dynamic behaviour corresponding to the appropriate curve. The background region was assigned a constant value of 1. To summarize, a total of six different phantoms, each consisting of four dynamic regions, were created: two geometries (annulus and ball) times three categories of behaviour (concave-up-decreasing, concave-down-up, and concave-down).

Projection data corresponding to the six phantoms were computed by simulating an

	Concave-up-decreasing $1+9e^{-\lambda t}$	Concave-down-up $1+40\left(-e^{-\lambda_1 t}+e^{-\lambda_2 t}\right)$		Concave-down $1+10\left(-e^{-\lambda_1 t}+e^{-\lambda_2 t}\right)$	
	$T_{\frac{1}{2}}(\lambda)$	$T_{\frac{1}{2}}(\lambda_1)$	$T_{\frac{1}{2}}(\lambda_2)$	$T_{\frac{1}{2}}(\lambda_1)$	$T_{\frac{1}{2}}(\lambda_2)$
r1	0.5	0.125	0.25	0.5	40.0
r2	2.0	0.5	1.0	1.0	60.0
r3	4.0	2.0	4.0	2.0	80.0
r4	8.0	4.0	8.0	4.0	100.0

Table 3.1: Functions and parameters used to generate the 12 TACs in Figure 3.2. The exponential functions used to generate each TAC are shown in the column heading. Both the time t and half-life values $T_{\frac{1}{2}}$ are in minutes. The $T_{\frac{1}{2}}$ values are related to the corresponding λ values by $\lambda = \ln(2)/T_{\frac{1}{2}}$.

acquisition using a dual-head camera with heads perpendicular to one another. This configuration was chosen because dual-head cameras are widely available in clinics, and because a single-head acquisition, which gives only one view through the object for every time frame, is not sufficient to obtain reasonable results using dSPECT [16]. The heads started at 0° and 90° (corresponding to the left and bottom sides of the objects in Figure 3.1) and rotated counterclockwise over 360°. Poisson-distributed noise was added to the projection data only in the third and fourth experiments. Some sample sinograms are shown in Figure 3.3. The projection data were computed using the same dynamic system matrix C' as was used in the reconstruction algorithms.

3.2 Image analysis

In every experiment, each set of projection data was used to reconstruct an image using 500 iterations of both the dEM and d^{2}EM algorithms. This is a considerably larger number of iterations than would be used in practice, but it was useful to examine the long-term convergence behaviour of the two algorithms. A total of four different experiments, which are described in subsequent sections, were run to examine various aspects of the d^{2}EM algorithm.

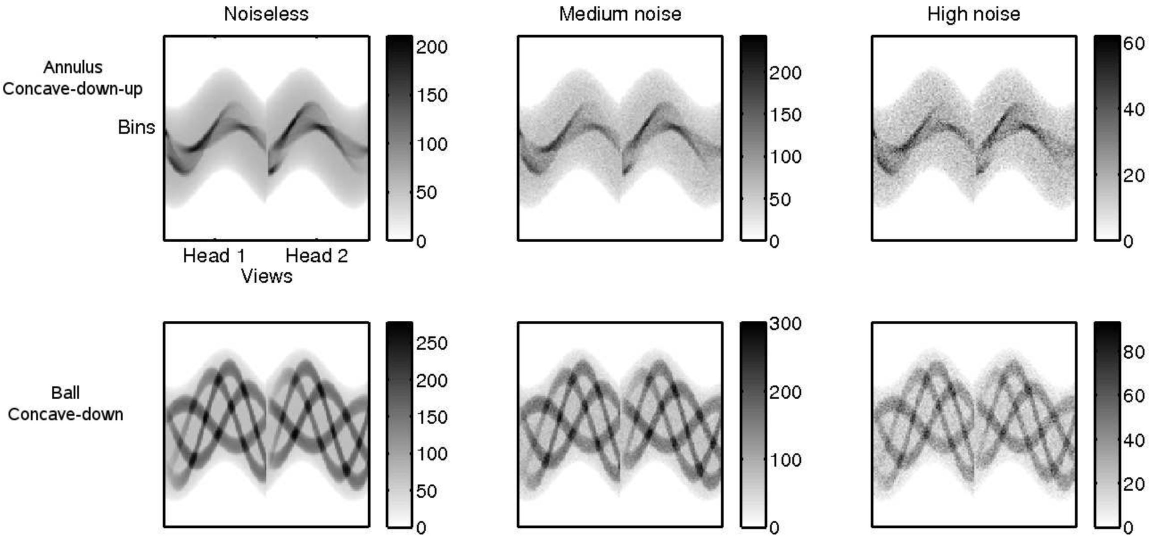

Figure 3.3: Sample dual-head sinograms used in the 2D phantom experiments. Top row: annulus phantom for the concave-down-up kinetic behaviour; Bottom row: ball phantom for the concave-down behaviour. Left column shows noiseless data, middle column shows medium-noise data, and right column shows high-noise data. Noisy data was used only in Experiments 3 and 4.

Five different figures of merit were defined to assess the performance of dEM and d^{2}EM, and the quality of the reconstructed images. The first two figures defined below were examined as functions of the number of iterations, in order to assess the convergence properties of either algorithm. The last three figures of merit were used to assess the quality of images after a fixed number of iterations had been run, and were only examined in Experiments 3 and 4.

1. Residual: The residual was defined as

$$r^{(\mathrm{n})} = \left\| C' x'^{(\mathrm{n})} - p \right\|_2 \tag{3.1}$$

where n is the number of iterations, p is the simulated projection data, and C' is the slow-rotation dynamic SPECT system matrix as defined in (1.20). $x'^{(\mathrm{n})}$ is the vector representing the dynamic image at iteration n, obtained by inverting (2.1) for dEM or (2.9) for d^{2}EM. The residual is a measure of how well the current image estimate fits the projection data, under the assumed system model given by C'.

2. Total relative error: Total relative error was given by

$$E^{(\mathrm{n})} = \left\| x'^{(\mathrm{n})} - x'^{\mathrm{true}} \right\|_2 \Big/ \left\| x'^{\mathrm{true}} \right\|_2 \times 100\%. \tag{3.2}$$

where x'^{true} is the original phantom used to generate the projections. $E^{(\mathrm{n})}$ is a measure of how close the current image estimate is to the true image. Note that since the slow-rotation dynamic SPECT reconstruction problem is highly underdetermined, two solutions with vastly different values of $E^{(\mathrm{n})}$ could produce the same residual $r^{(\mathrm{n})}$.

3. Relative error of mean TAC in regions of interest: One typical method of analyzing a dynamic image is to draw a region of interest (ROI) over part of the image and observe the time activity curve for that region, averaged over all voxels. Thus, assessing how well the reconstruction method recovers the mean TAC for a region is a good practical measure of performance. For both the annulus and ball phantoms, ROIs corresponding to the four dynamic regions r1 to r4 were defined, as given by the true phantom boundaries. The 1×64 vector representing the mean TAC for each region, obtained from the reconstructed image, was denoted by τ, and the equivalent vector representing the true mean TAC was denoted by τ^{true}. The relative TAC error for each region was then defined as

$$\varepsilon = \left\| \tau - \tau^{\mathrm{true}} \right\|_2 \Big/ \left\| \tau^{\mathrm{true}} \right\|_2 \times 100\%. \tag{3.3}$$

This error measure indicated how well the reconstructed image agreed with the truth in the aggregate sense, in the most important dynamic regions of the image.

4. Weighted relative standard deviation between voxel TACs: Since the dynamic activity in every ROI of the phantoms was known to be homogenous (i.e. the same in every voxel), it is desirable for this to be reflected in the reconstructed images as well. While it is not reasonable to expect the TACs in every voxel of a reconstructed ROI to be identical, ideally there should not be a great deal of variation between them. In order to assess the amount of variation, a weighted relative standard deviation for each ROI, summed over all time frames, was calculated by

$$\bar{\sigma} = \sum_{k=1}^{K} W_k \frac{\sigma_k}{\nu_k} \times 100\%, \tag{3.4}$$

where σ_k is the standard deviation between true and reconstructed activities in every voxel of the ROI at time k, ν_k is the true activity at time k for a voxel in the ROI, and the weighting factor is

$$W_k = \nu_k \Bigg/ \sum_{k'=1}^{K} \nu_{k'}.$$

The weighting ensured that the relative variation in time frames where the activity level was high was weighted more heavily than variation in time frames of low activity.

5. Average relative shape error: Even if the amount of variation between TACs within an ROI is similar for two different images, one may still be judged to be superior to the other. Consider the example presented in Figure 3.4. Suppose we have an ROI consisting of two voxels, where the true dynamic behaviour is a constant curve (dashed line). In reconstructed image A, the TAC in one voxel of the ROI has increasing behaviour, and the TAC in the other has decreasing behaviour (solid lines, left plot). In Image B, both voxels are reconstructed as having constant behaviour, but with the incorrect magnitude (right plot). In both cases, the variation within the ROI, as would be quantified by $\bar{\sigma}$, is the same. Image B, however, has recovered the correct, constant dynamic behaviour in both voxels, while Image A has not. The TAC *shapes* provided by Image B are in better agreement with the truth than those provided by Image A, and thus this image should be judged to have higher quality.

In order to quantify the consistency of TAC shapes within each ROI, then, an average relative shape error was calculated by:

$$\mathcal{S} = \frac{1}{I'} \sum_{i=1}^{I'} \left(\|\tau^{\text{true}} - \alpha_i \tau_i\|_2 \Big/ \|\tau^{\text{true}}\|_2 \right) \times 100\% \tag{3.5}$$

where I' is the number of voxels in the ROI, τ_i is the 1×64 vector representing the reconstructed TAC in voxel i, τ^{true} is the true TAC vector for that ROI, and α_i is the scaling factor which minimizes the 2-norm difference between the two vectors:

$$\alpha_i = \frac{\tau^{\text{true}} \cdot \tau_i}{\tau_i \cdot \tau_i},$$

where $\cdot$ is the dot product between the two vectors. The average relative shape error measured how consistent the shapes of TACs were with the truth inside each ROI, while ignoring their magnitudes. If the shape of the TAC in a voxel of the reconstructed image was

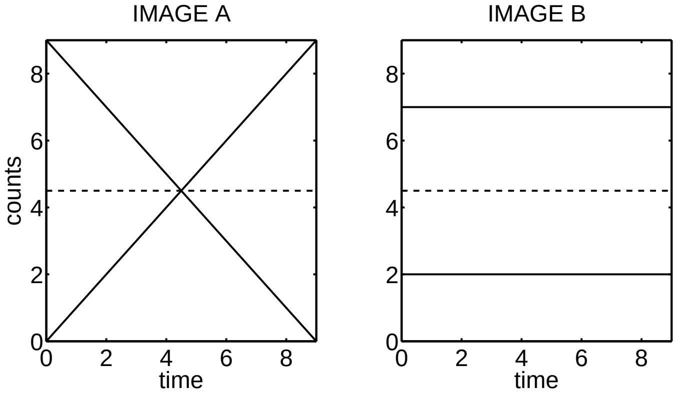

Figure 3.4: Example motivating the use of the shape error $\mathcal{S}$ to quantify the consistency of TAC shapes within an ROI. The true TAC within the ROI, which consisted of two voxels, is indicated by the dashed line, and the reconstructed TACs are indicated by solid lines for both Images A and B.

close to the true shape, then the difference between them would be small after scaling; if their shapes were different, then the difference would still be relatively large.

3.3 Experiment 1: fixed and non-fixed difference tensors

Both dEM and d^{2}EM require adjusting the difference tensor in between iterations of the algorithm in order to determine the correct dynamic behaviour. The goal of this experiment was to determine to what extent the need to adjust the difference tensor affects convergence of either algorithm. This information was useful in interpreting the results of subsequent experiments.

In this experiment, a first set of reconstructed images was created where the true times of peak activity, or times of inflection, for every voxel were provided to the dEM and d^{2}EM algorithms, respectively. That is to say that the correct difference tensor A or B was provided, and not allowed to change in between iterations. This experiment was then repeated for the general case, where the difference tensor was unknown and had to be adjusted between iterations. For the dEM reconstruction, the TAC in every voxel was initially assumed to peak at the midway point of the acquisition (the 32$^{\text{nd}}$ time frame). For d^{2}EM, the TAC in every voxel was assumed to be concave down-up, with the inflection

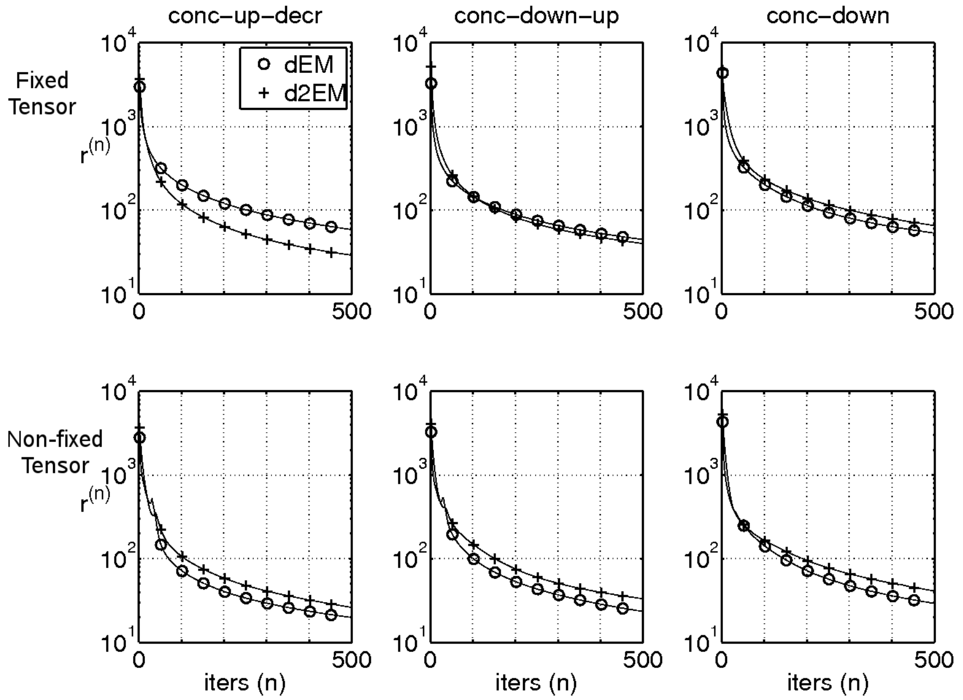

Figure 3.5: Residual values $r^{(\mathrm{n})}$ as a function of the number of iterations for the annulus phantom reconstructions (left, middle and right columns), for both the fixed tensor (top row) and non-fixed tensor (bottom row) experiments. Y-values are on a logarithmic scale.

point occurring in the 32$^{\mathrm{nd}}$ time frame. The expectation was that the performance of both algorithms should be better in the first case than in the second case, where the correct difference tensor was not known *a priori*.

Figures 3.5 and 3.6 show the behaviour of the residual $r^{(\mathrm{n})}$ and total relative error $E^{(\mathrm{n})}$ for the reconstruction of the three annulus phantoms using both dEM and d^{2}EM. The top row of both figures show the results when the tensor was held fixed at the correct configuration, while the bottom row shows the results when the tensor was adjusted between every iteration after a generic initial assumption. The behaviour of $r^{(\mathrm{n})}$ and $E^{(\mathrm{n})}$ for the three ball phantom experiments were similar.

The most noticeable difference between the fixed and non-fixed tensor reconstructions was that the convergence of both $r^{(\mathrm{n})}$ and $E^{(\mathrm{n})}$ was no longer monotonic when the tensor was not fixed. For the phantoms with concave-up-decreasing and concave-down-up TACs,

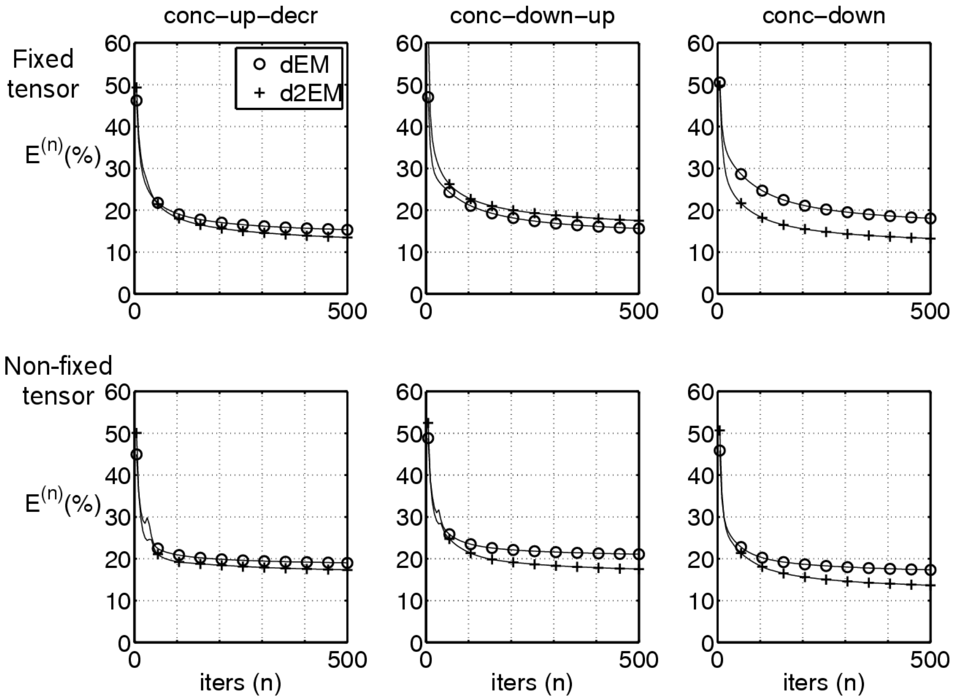

Figure 3.6: Total relative error values $E^{(n)}$ as a function of the number or iterations for the annulus phantom reconstructions (left, middle and right columns), for both the fixed tensor (top row) and non-fixed tensor (bottom row) experiments.

the errors briefly increased between 30 and 40 iterations, before monotonically decreasing again. It is evident when looking at the reconstructed images that this occurs as a result of the adjustments being made to the difference tensor during these iterations. As an example, Figure 3.7 shows average TACs in region 2 of the annulus phantom with concave-down-up kinetics. As the location of peak activity/inflection point shifts left towards the correct location, the error between the reconstructed and true time activity curves briefly increases before the correct shape is found.

For every experiment, whether dEM or d^{2}EM was used, the value of $r^{(n)}$ at the 500th iteration was smaller if the tensor was not fixed than if it was held fixed; however, the value of $E^{(n)}$ was almost always smaller in the fixed tensor case. This illustrates the dichotomy between the residual and image error for a large, underdetermined problem such as this one. By relaxing the conditions on the solution (i.e. making the tensor non-fixed), one is able

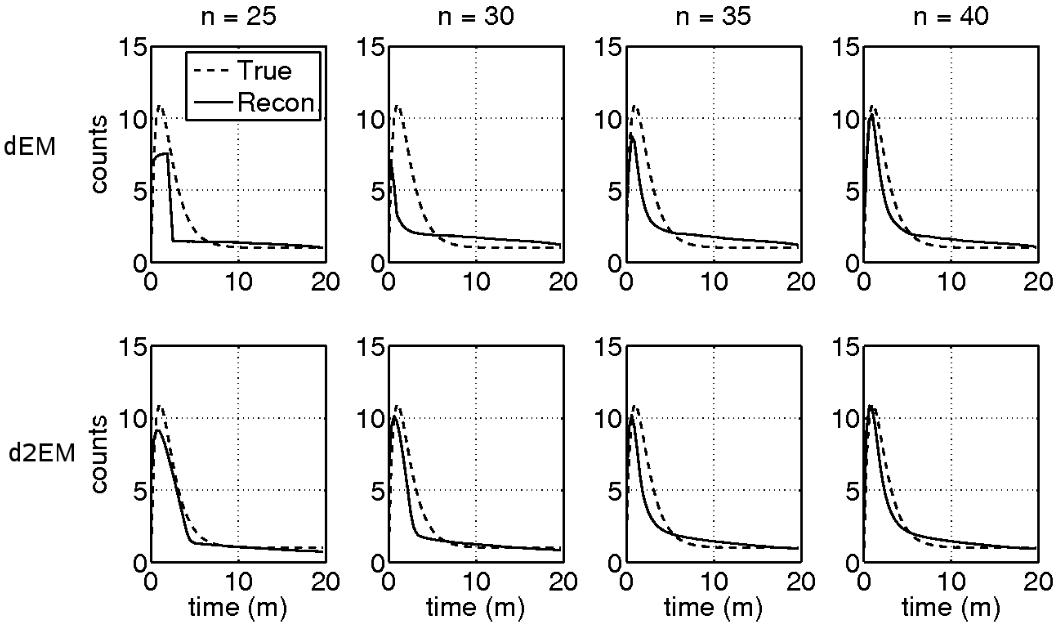

Figure 3.7: Non-monotonic convergence of dEM and d^{2}EM when the difference tensor is adjusted between iterations. The true TAC in region 2 of the concave-down-up ball phantom is shown as a dashed line, while the average TAC in r2 of the reconstructed dEM (top row) and d^{2}EM (bottom row) images is shown as a solid line. The error between the true and mean TAC increases briefly in iterations 30 and 35 as the algorithm determines the correct locations of peak activity (for dEM) or inflection point (d^{2}EM).

to better fit the data, even though the solution is actually farther from the truth than if the tensor is held fixed at the correct configuration. Thus, the method that provides the smallest residual is often not providing the most accurate image. This also held when comparing the images generated by dEM vs d^{2}EM for both the fixed and non-fixed experiments; in almost every case the method that provided the lower error (usually d^{2}EM) had the higher residual.

Finally, although the values of $E^{(n)}$ when the tensor was held fixed were always smaller than the corresponding values in the non-fixed case, the discrepancy was usually not large. This is somewhat surprising given that the true behaviour of the phantom was known in the fixed experiment, but had to be determined in the non-fixed case. Thus, the dEM and d^{2}EM algorithms were both able to determine the correct behaviour quickly when it was not known beforehand.

3.4 Experiment 2: comparison of transition schemes

Two methods for allowing d^{2}EM to adjust the assumed dynamic behaviour in a voxel were discussed in Section 2.3.2; the five-state transition scheme illustrated in Figure 2.4, and the two-state transition scheme illustrated in Figure 2.5. In this experiment, these two schemes were compared by re-running the d^{2}EM reconstructions from Experiment 1 without holding the tensor fixed, but with the initial assumption of concave-up-down behaviour with the inflection point occurring in the 32$^{\text{nd}}$ time frame. Concave-up-down behaviour is a poor initial assumption for both concave-down-up and concave-up-decreasing behaviour, since the inflection point must be shifted earlier through the concave-down and concave-down-up states before arriving at the correct one (see Figures 2.4 and 2.5). Thus, the choice of transition rule has a larger impact on the convergence of the algorithm than if an initial behaviour that is “close” to the true one is chosen, as was the case in Experiment 1.

Convergence results of this experiment are shown in Figure 3.8. These results clearly show the superiority of the two-state transition model, which provided much better convergence in the concave-up-decreasing and concave-down-up experiments. The five-state transition model struggled to successfully adjust to the correct behaviour in these cases, as a result of the fact that the transition from the concave-down state to the concave-down-up state required the concavity of TACs to approach zero in the final time frame. Figure 3.9 shows an example from the reconstruction of region 2 of the concave-down-up ball phantom. While the voxel-level TACs are able to adapt smoothly to the correct behaviour under the two-state transition model, when the five-state model is used, several TACs are “stuck” in the concave-down state, even after many iterations. The TACs that do adjust to the concave-down-up state have their magnitudes scaled to very high values to compensate for the voxels that are stuck in the concave-down state. As a result, the $E^{(\mathrm{n})}$ values shown in Figure 3.8 actually increased sharply after 150 iterations in these two cases.

The convergence for the phantom with concave-down TACs (right column, Figure 3.8) was essentially the same using either transition scheme. This is due to the fact that adjusting from concave-up-down behaviour to concave-down behaviour does not require passing through the concave-down state, which was the main obstruction to the convergence of the

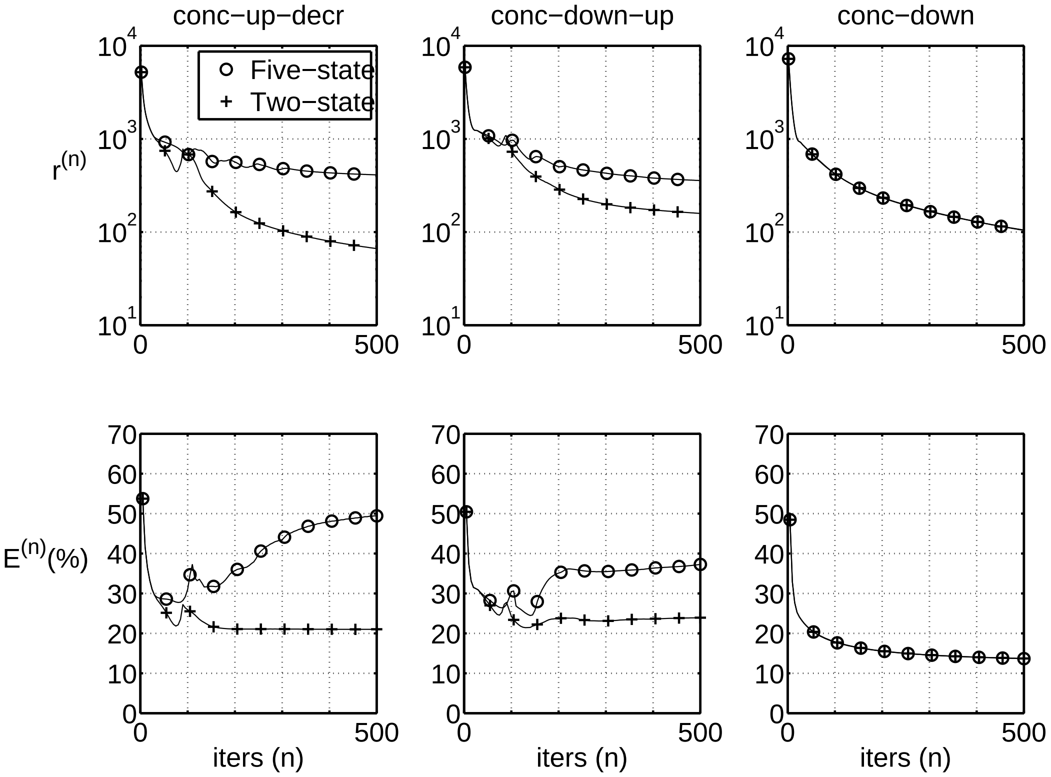

Figure 3.8: Comparison of the convergence behaviour of $r^{(\mathrm{n})}$ (top row) and $E^{(\mathrm{n})}$ (bottom row) for the three ball phantom experiments (left, middle and right columns), using d^{2}EM with both of the two proposed transition schemes. $r^{(\mathrm{n})}$ values are shown on a logarithmic scale. Results obtained for the annulus phantom were similar.

algorithm when the five-state model was used for the other two cases. This also illustrates that d^{2}EM is able to reconstruct concave-down TACs just as well when using the two-state model as when using the five-state model, despite the fact that the two-state model does not include the concave-down tensor (2.12). Finally, we note that even though the two-state model was successfully able to adapt to the correct behaviour despite the poor initial assumption, the error value to which it converged was still significantly larger than when a better initial estimate of concave-down-up behaviour was provided (cf. Figure 3.6, bottom row). This illustrates that the d^{2}EM method is sensitive to the initially assumed behaviour regardless of the transition rule that is used, and that one should take care to choose a

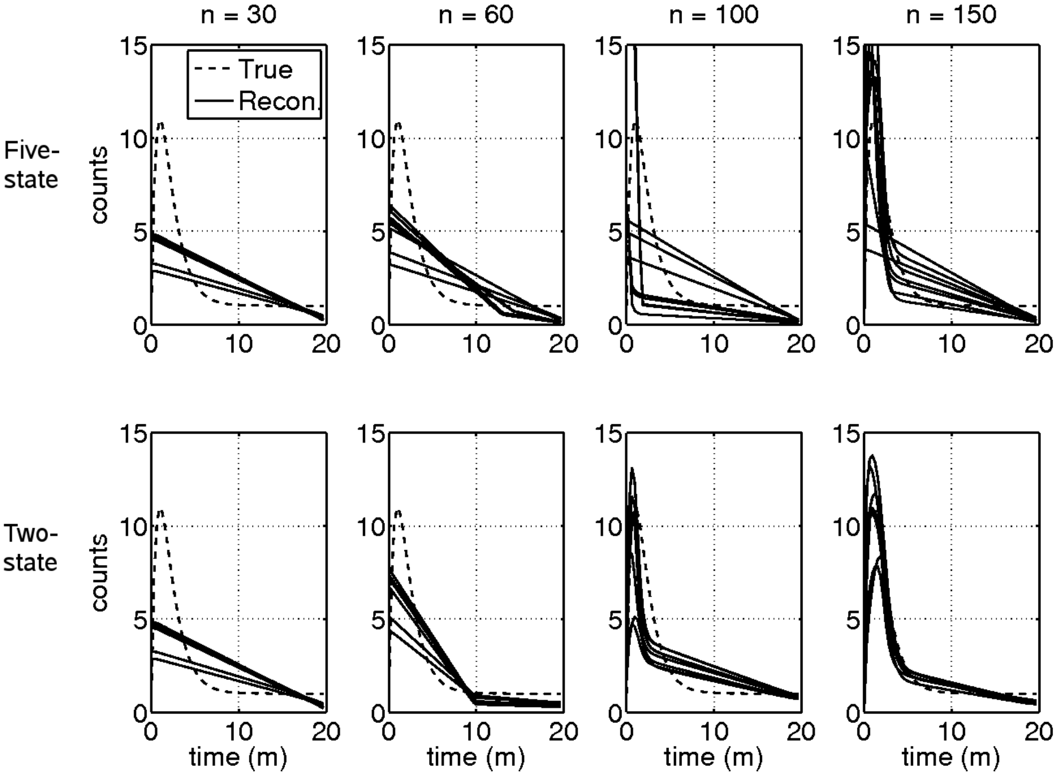

Figure 3.9: Illustration of the failure of the five-state model to adjust to correct kinetic behaviour. The true TAC in region 2 of the concave-down-up ball phantom is shown as a dashed line, while eight randomly selected voxel TACS extracted from r2 of the reconstructed d^{2}EM images using the five-state transition scheme (top row) and two-state transition scheme (bottom row) are shown as solid lines. Number of iterations is shown in column headings.

suitable initial condition, depending on what the expected kinetics are.

3.5 Experiment 3: effect of noise

In this experiment, Poisson noise was added to the projection data in order to assess its effect on reconstructions performed using the dEM and d^{2}EM algorithms. Three different levels of noise (high, medium and low) were added to every set of projection data. Since Poisson noise is proportional to the square root of the counts present in the projection data, the noise level was adjusted by scaling the counts prior to adding noise. Specifically, "medium-noise" projection data was generated by adding Poisson noise to the data used in the first two experiments; low-noise data was generated by multiplying the noiseless data by 4 before adding noise, and high-noise data by first dividing the noiseless data by a factor of 4. It is difficult to quantify the levels of noise absolutely, since they varied in time along with the count rates in the different dynamic regions. As an example, for the annulus phantom with concave down-up behaviour, the maximum pixel intensity at the five-minute mark for the "medium noise" projection data was 210, corresponding to a noise level of 7%; at the 15-minute mark it was 140, corresponding to a noise level of 8.5%. If noise is quantified in this way, then the "medium" noise level was 7 to 11% for the annulus phantom data, and slightly lower for the ball phantom data, since the dynamic regions were larger, which produced higher count levels in the projection data. The noise level was then twice as great in the high-noise data compared to the medium-noise data, and half as great in the low-noise data. Some examples of the noiseless and noisy projection data were presented in Figure 3.3.

Adding noise had little effect on the convergence of the residual; just as in the noiseless case, $r^{(\mathrm{n})}$ decreased monotonically with the number of iterations – aside from a brief period initially when the tensor was being adjusted. The algorithms were now simply fitting noisy instead of noiseless data. Convergence of $E^{(\mathrm{n})}$ was significantly different, however. In particular, after some number of iterations, $E^{(\mathrm{n})}$ began to monotonically *increase* as more iterations were performed. As discussed in Section 1.1.3, this phenomenon is well-documented for MLEM, and occurs because as the algorithm continues to maximize the likelihood that the image fits the noisy data, the image itself becomes noisier [30]. Figure 3.10 shows the behaviour of $E^{(\mathrm{n})}$ for several different noise levels and kinetic profiles. It is apparent from

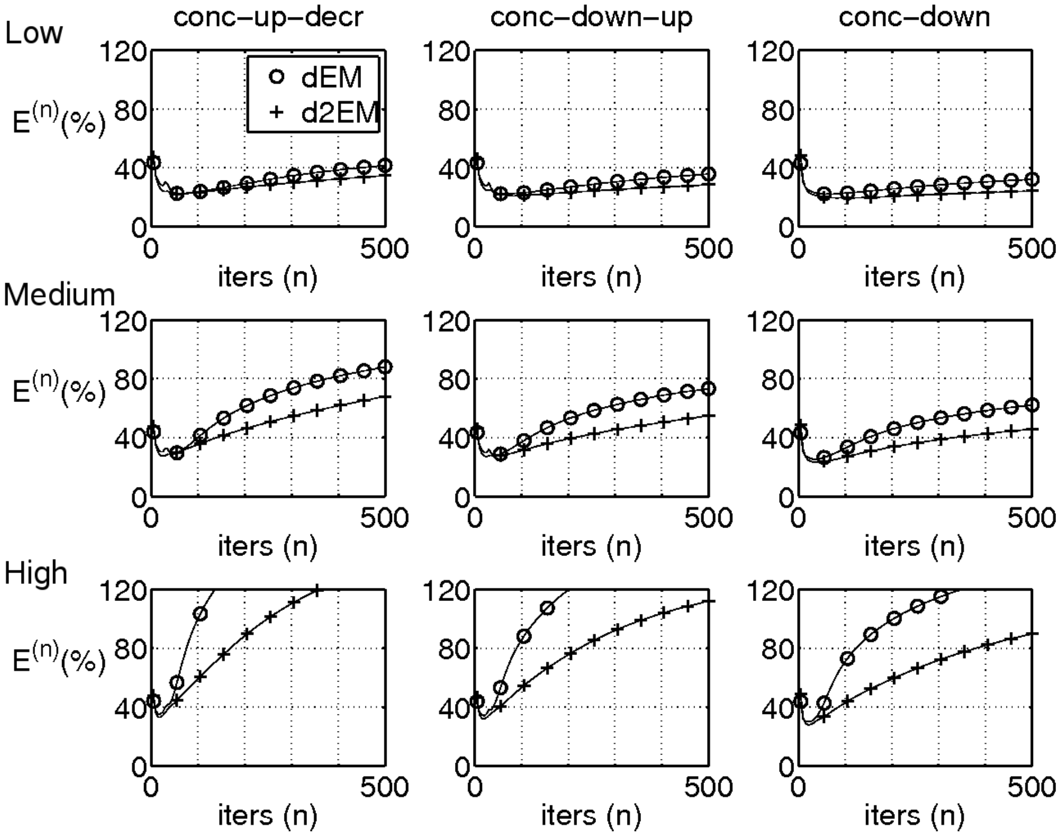

Figure 3.10: Effect of noisy projection data on the convergence of total relative error, $E^{(\mathrm{n})}$. Plots are shown for low (top row), medium (middle row) and high (bottom row) levels of noise, for the three ball phantoms. (Left, middle and right columns).

this figure that d^{2}EM performs better in the presence of noisy data than dEM does, especially if the level of noise in the projection data is high. For both algorithms, the solution diverges from the truth more quickly in the presence of more noise.

Based on the convergence plots and visual examination of the images, it was determined that 80 iterations was a reasonable cut-off point at which to analyze the actual images produced by dEM and d^{2}EM. Running further iterations made the images noisier without appreciably improving the accuracy of TACs, in general. Images from two of the phantom simulations are shown in Figure 3.11. Since a total of eighteen simulations were run (six phantoms, 3 noise levels), it is not possible to comprehensively show the results of all of them, but Figure 3.11 is representative of the results in general. Visually, the d^2EM images tended to be somewhat less noisy than the dEM reconstructed images. For instance, in the last column of both images shown in Figure 3.11, the d^2EM image is noticeably less speckled than the corresponding dEM image. Since the d^2EM constraint links time frames of the image together more strongly, the effect of noise on the images has been better controlled.

More differences are apparent when examining representative voxel-level TACs from the dEM and d^2EM images, as in Figure 3.12. The behaviour of the TACs in the dEM images is erratic and often incorrect. Many TACs contain sharp spikes as a result of the noise in the image. The d^2EM constraint prevents these spikes from occurring, since a sharp peak in one voxel would require that the concavity of the TAC change twice. The behaviour of TACs at the voxel level is not always correct in the d^2EM image either (for instance, many of the TACs in the d^2EM images shown in Figure 3.12 have washout rates that are too fast or too slow), but in general they have more consistent shapes and are in better agreement with the true TAC than those obtained from dEM. There is still considerable variation in magnitude among voxel level TACs in both the dEM and d^2EM images, however.

Figure 3.13 shows the mean TACs extracted from the four dynamic regions in the same two phantom reconstructions, for both the dEM and d^2EM images. At the low and medium noise levels, the discrepancy between dEM and d^2EM was not very apparent when looking at the mean TACs. For instance, in the top set of plots in Figure 3.13 (concave-down ball phantom, medium noise level), the mean TACs for the dEM and d^2EM images are quite similar. At the high noise level, more of a difference was visible as the mean TAC in the dEM images was more severely affected by the noise.

The error measures ε, $\bar{\sigma}$ and $\mathcal{S}$ (Equations 3.3 to 3.5) were calculated for each of the four dynamic regions in every image. The full results of the annulus and ball phantom simulations are tabulated in Tables A.1 and A.2 of Appendix A, respectively. Several summary statistics, presented in Table 3.2, were also computed by grouping the error measures together. The average of each error measure within a group was calculated for both the dEM and d^2EM reconstructions, and the percentage improvement was defined by

$$\text{Improvement (\%)} = \left(\text{dEM average} - \text{d}^2\text{EM average}\right) \Big/ \text{dEM average} \times 100\% \qquad (3.6)$$

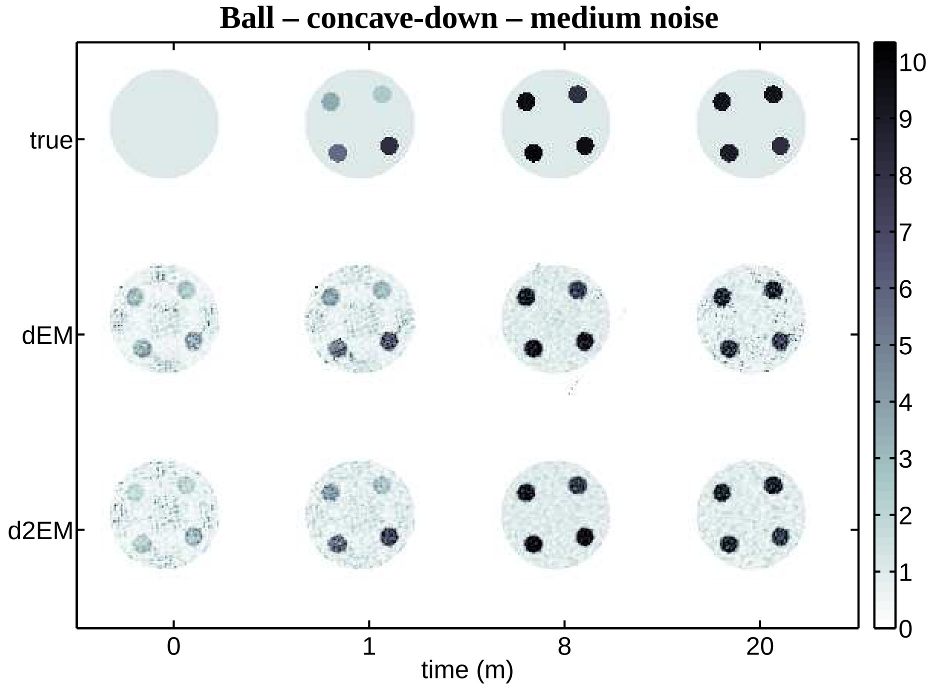

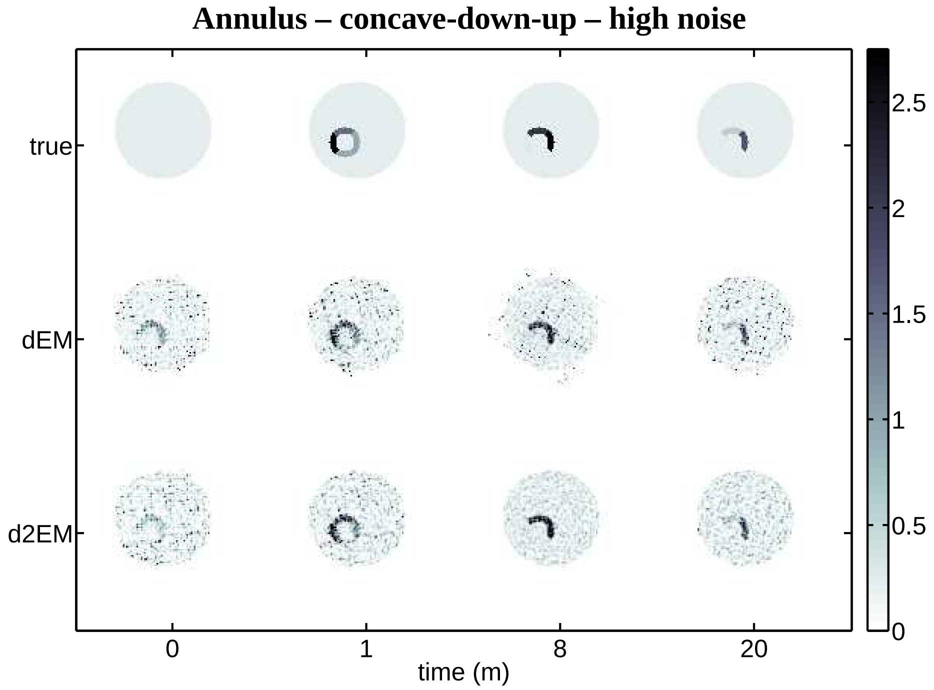

Figure 3.11: Images showing time frames from two representative reconstructed images after 80 iterations. Frames from the true image (top row), dEM reconstructed image (middle row) and d^{2}EM reconstructed image (bottom row) are shown at various time points (horizontal axis). Images are scaled to the maximum value in the true image.

Ball – concave-down – medium noise

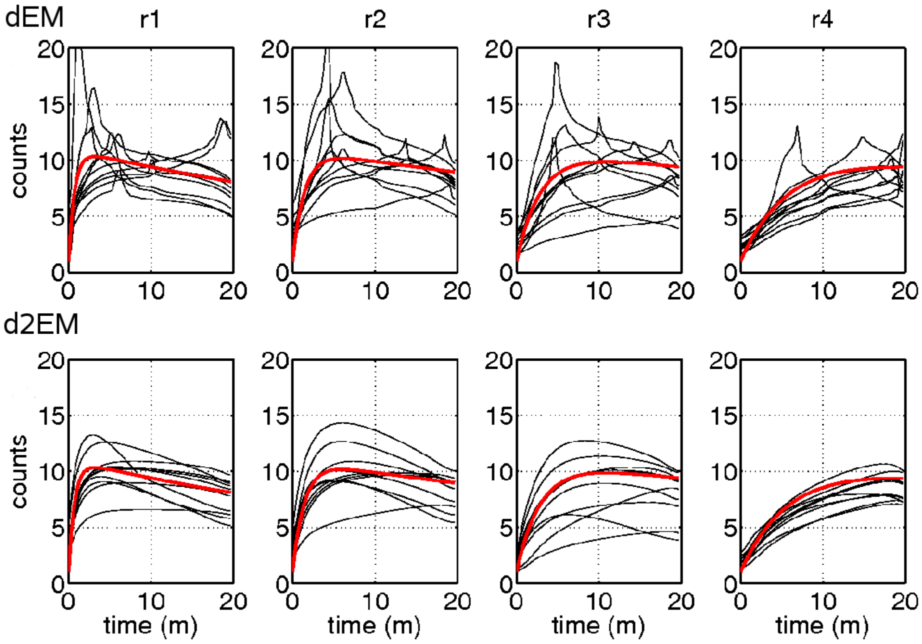

Annulus – concave-down-up – high noise

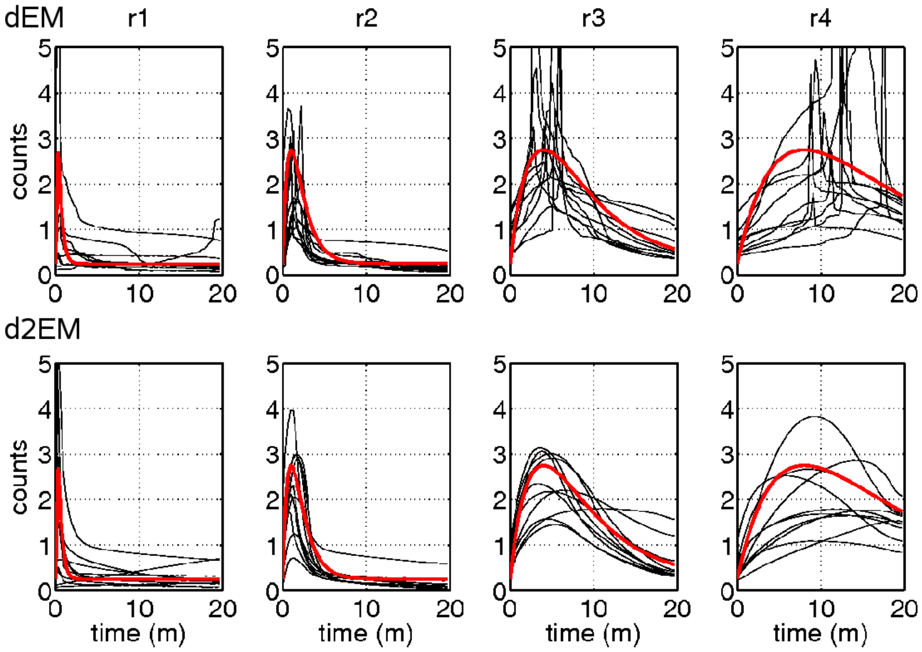

Figure 3.12: Representative TACs from voxels in the four different regions (r1, r2, r3 and r4) of the two selected reconstructed images after 80 iterations. Red line shows true TAC for that region, while thin black lines show TACs from 10 randomly selected voxels within the region. Top row of each set of plots corresponds to the dEM image, bottom row to the d^2EM image.

Ball – concave-down – medium noise

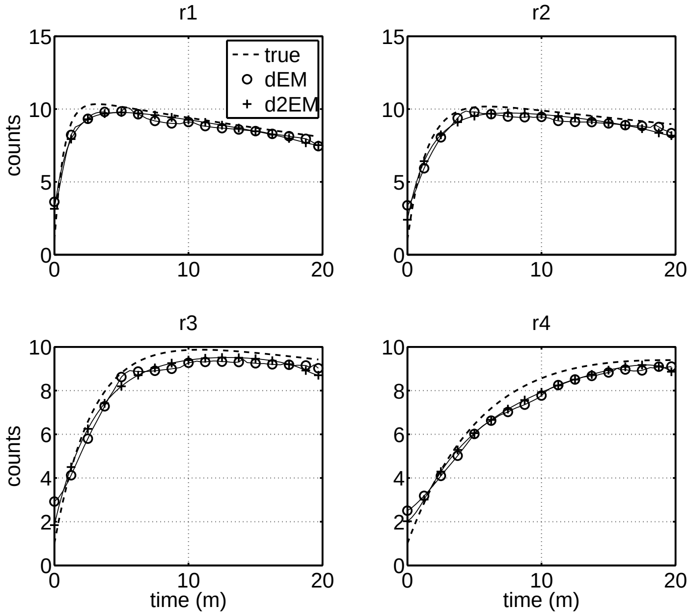

Annulus – concave-down-up – high noise

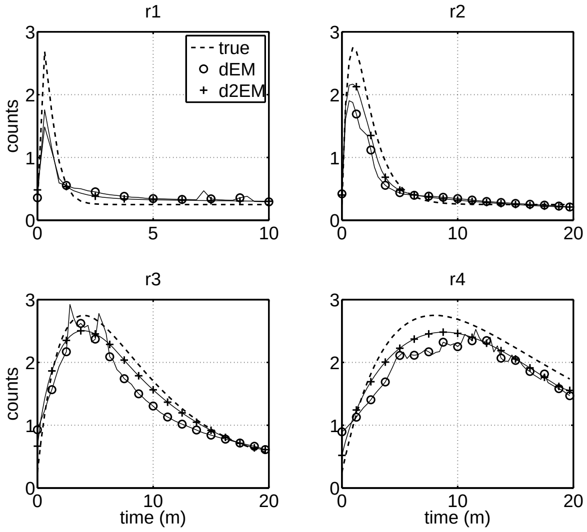

Figure 3.13: Mean time activity curves from the four different regions (r1, r2, r3 and r4) of the two selected reconstructed images after 80 iterations. Dashed line shows true TAC for that region, solid line with circles shows mean TAC for that region extracted from the dEM image, and solid line with crosses shows mean TAC extracted from d^{2}EM image.

Paired t-testing was also performed to compare the error measures obtained from the dEM and d^{2}EM images, in order to assess the significance of any improvements made by d^{2}EM. A p-value of 0.05 or less was considered to be a significant improvement.

To compute these summary statistics, the simulations were grouped in three ways: by noise level (high, medium or low), by kinetic behaviour (concave-up-decreasing, concave-down-up and concave-down) and by geometry (annulus, ball). So, for instance, the average value of ε for the low noise images reconstructed using dEM, which is the top left-hand value in Table 3.2, is the average of the 24 ε measures corresponding to the four regions in all six low-noise simulations (three annulus, three ball phantoms). A paired t-test was then performed on the same 24 values to produce the p-value given in the same table. The statistics grouped by noise and kinetic behaviour are all based on 24 values each, while the statistics grouped by geometry are based on 36 values each (four regions, times three noise levels, times three kinetic behaviours). A final set of statistics over all the simulations (72 values) is also given in Table 3.2.

Referring to Tables A.1 and A.2, the relative error in the mean TACs within regions, ε, was improved by using d^{2}EM in nearly every case. The lone exceptions were for region 1 of the phantoms with concave-up-decreasing and concave-down-up TACs. These two cases featured the fastest kinetic behaviour of any that were simulated, with wash-out half-lives of 15-30 seconds. Since the TACs in these regions changed rapidly, they were the least smooth, so the d^{2}EM constraint was not as effective as in regions where the kinetics were more gradual. In most regions, however, ε was considerably improved. Results of paired t-testing indicated a significant improvement over all groups of experiments (see Table 3.2). Improvements to ε were generally more significant at higher noise levels and for simulations with slower kinetic behaviour, such as those with concave-down TACs.

Improvements to the weighted standard deviation within regions, $\bar{\sigma}$, were not as great as to ε, and failed to pass the significance test in several cases. This is reflective of the fact that there is considerable deviation in magnitude among TACs in images reconstructed with both dEM and d^{2}EM, as is visible in Figure 3.12. Despite this fact, the paired t-test did indicate that d^{2}EM significantly improved $\bar{\sigma}$ in several cases, particularly in the simulations with high noise levels and slow tracer kinetics.

The shape error $\mathcal{S}$, which ignores the magnitudes of voxel TACs, was improved in most regions; again with the exception of those regions with very fast kinetic behaviour. Im-

	Noise				Kinetics				Geometry			
		ε	$\bar{\sigma}$	$\mathcal{S}$		ε	$\bar{\sigma}$	$\mathcal{S}$		ε	$\bar{\sigma}$	$\mathcal{S}$
dEM avg.	Low	13.1	23.2	14.7	c-u-d	17.1	34.3	21.5	Annulus	17.4	36.7	23.4
d^{2}EM avg.		11.7	22.5	12.5		14.7	34.3	19.7		14.3	35.0	18.2
Imprv. (%)		10.6	3.0	14.7		14.3	-0.2	8.6		17.6	4.7	22.4
p-value		1.8E-2	1.1E-1	1.7E-2		1.4E-4	4.5E-1	2.2E-2		1E-5	5.3E-3	2.1E-5
dEM avg.	Mid	14.4	30.0	19.9	c-d-u	18.5	39.4	26.7	Ball	12.5	32.1	20.4
d^{2}EM avg.		12.3	29.2	15.7		15.5	37.4	22.1		10.6	29.8	15.8
Imprv. (%)		14.4	2.6	16.7		16.2	5.1	17.3		15.3	7.2	22.6
p-value		1.4E-3	1.4E-1	4.5E-3		5.6E-3	3.8E-2	5.3E-3		7.5E-4	2.0E-3	4.5E-5
dEM avg.	High	17.4	50.1	32.1	c-d	9.2	29.5	17.5	All	14.9	34.4	21.9
d^{2}EM avg.		13.4	45.5	22.7		7.2	25.4	9.2		12.5	32.5	17.0
Imprv. (%)		23.0	9.2	29.4		21.8	13.9	47.5		16.6	5.9	22.5
p-value		3.9E-5	6.4E-5	2.3E-7		4.2E-7	1.3E-6	5.8E-9		5.1E-8	5.1E-5	5.2E-9

Table 3.2: Summary statistics of data presented in Tables A.1 and A.2. c-u-d, c-d-u and c-d refer to the concave-up-decreasing, concave-down-up and concave-down kinetic behaviours, respectively. “Imprv (%)” refers to the percent improvement (3.6). p-values obtained from paired t-testing are given in scientific notation.

provements in $\mathcal{S}$ were particularly noticeable in the simulations with concave-down TACs, which had the most gradual kinetic behaviour. In the dEM images, the shapes of voxel TACs in these simulations varied considerably, while in the d^{2}EM images they were much more consistent.

All three error measures tended to be larger in the annulus phantom experiments than in the ball phantom experiments, whether dEM or d^{2}EM were used. This discrepancy is reflective of the fact that the dynamic regions of the ball phantom were larger and better-separated than in the annulus phantom. The use of d^{2}EM over dEM reduced errors for both geometries, however. Taking the experiments as a whole, all three error measures were significantly reduced by using d^{2}EM over dEM. Improvements were the greatest in those simulations that involved high noise levels and/or more gradual tracer kinetics. Of the three error measures, ε and $\mathcal{S}$ were improved by a greater margin than $\bar{\sigma}$.

3.6 Experiment 4: d^{2}EM versus OSEM

A final experiment was run to provide context for some of the results of Experiment 3. Specifically, although using d^{2}EM over dEM generally reduced all three measures of error, some error values seemed large even when d^{2}EM was used. This was particularly true of $\bar{\sigma}$, which quantified the deviation among TACs within each homogenous dynamic region. It is not clear what constitutes a “low” value of $\bar{\sigma}$, however, since a value of zero would mean that the image has been perfectly reconstructed, which is not realistically achievable. In order to provide context, an additional set of images was produced using the static OSEM algorithm (described in Section 1.1.3).

Since OSEM is a static reconstruction algorithm, it is unable to produce a dynamic image from the slow-rotation data used by dEM and d^{2}EM, where only two views of the object are available for every time frame. For the OSEM reconstructions, then, projection data consisting of 64 views around the object for *each* of the 64 time frames was used, modeling a ring SPECT-like system with 64 detectors. Thus, 32 times as many views were acquired per time frame (compared to the projection data used by dEM and d^{2}EM), while the counts for each view were not reduced, as they would be by acquisition using a fast-rotating camera. This is a highly idealized situation; the intent was to provide a “gold standard” against which to compare the d^{2}EM images, using a well-established image reconstruction method. Six iterations of OSEM with 8 subsets were used to reconstruct each frame of the dynamic images separately. The same three kinetic profiles and three noise levels were used as in Experiment 3, but only the ball phantom geometry was used.

Time frames from two representative images are shown in Figure 3.14. Visually the OSEM images are superior, which is to be expected given the higher quality of the data used to reconstruct them. In particular, in the first frame of the d^{2}EM images, the outlines of the four dynamic regions are visible even though these regions do not yet contain any more activity than the background. This is a consequence of the fact that d^{2}EM (and dEM) link the time frames of the image together, so that information from projection data acquired later can influence earlier time frames. In the OSEM image, only the projection data corresponding to that time frame was used.

Regions with fast kinetics were also much better reconstructed using OSEM. Since d^{2}EM only had a small number of views around these regions during the time period when the kinetics were changing rapidly, it tended to underestimate the amount of activity in these regions as a result of blurring. For instance, in the concave-down-up reconstruction (bottom image, Figure 3.14), region 1 is apparent at 1 minute in the image reconstructed with OSEM, but is hardly visible in the image reconstructed with d^{2}EM. Aside from these regions, however, the visual quality of the d^{2}EM image was comparable to that obtained using OSEM, despite the much smaller amount of data used.

Representative voxel TACs from the d^{2}EM and OSEM images are shown in Figure 3.15. The TACs in the OSEM images oscillate considerably as a result of the fact that no temporal regularization was included in the reconstruction algorithm, and there is also considerable variation in the magnitude of the TACs in many regions. Mean TACs from two simulations are shown in Figure 3.16. In most regions, the mean TACs obtained from images reconstructed with either method are similar. Again, the exceptions are in the two regions with very fast kinetics (r1 of the phantoms with concave-up-decreasing and concave-down-up TACs), where the d^{2}EM TAC is underestimated as a result of blurring due to limited angular information[1].

The calculated error values for all the OSEM and d^{2}EM reconstructed images are tabulated in Table A.3. From these results, it is apparent that some variation among TACs, as quantified by $\bar{\sigma}$, is inevitable using either approach. For low-noise simulations, the value of

---

[1] This effect is discussed further in Chapter 4.

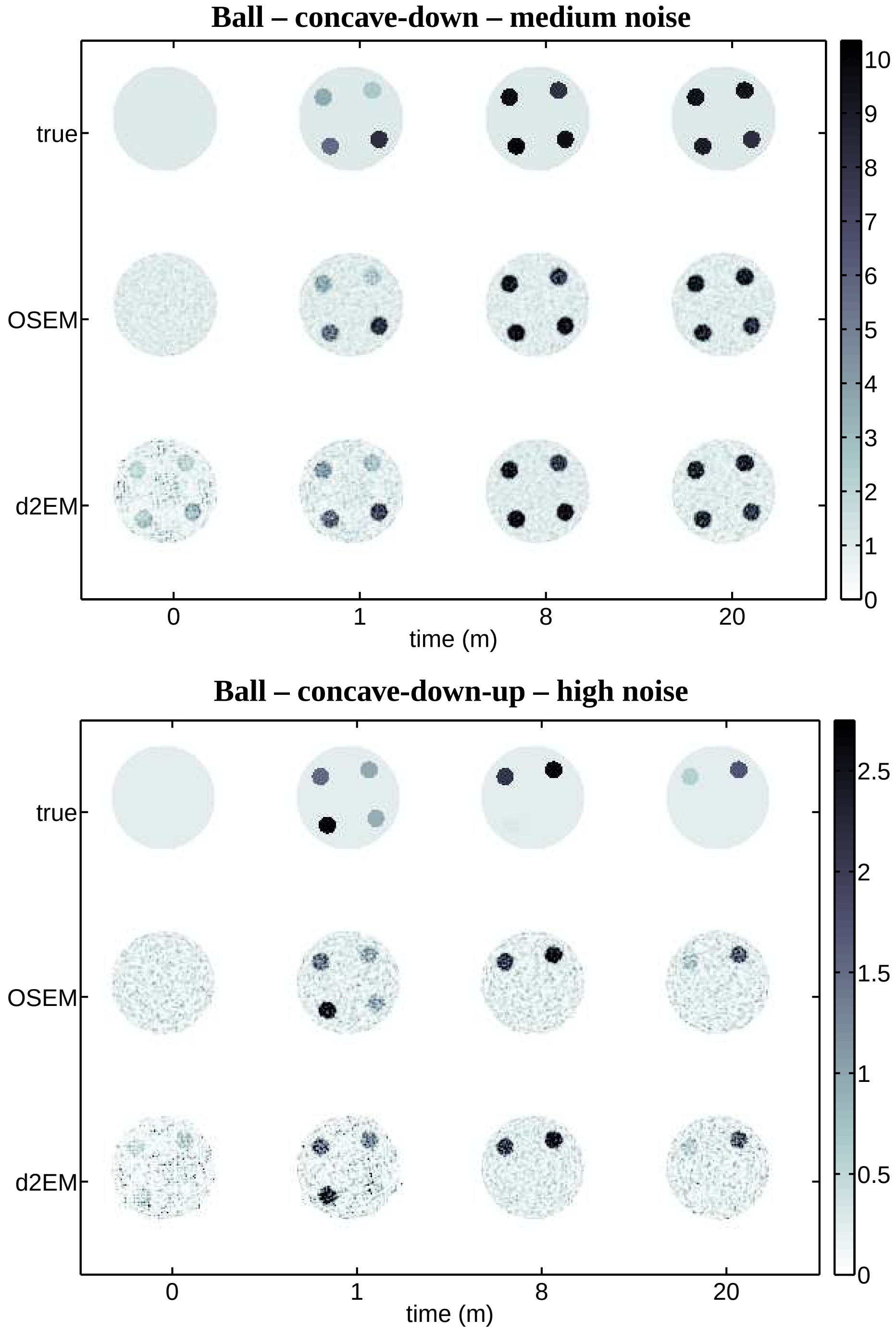
Ball – concave-down – medium noise

Ball – concave-down-up – high noise

Figure 3.14: Images showing time frames from two representative reconstructed images after six iterations of OSEM per frame (middle row) and 80 iterations of d^{2}EM (bottom row). Frames are shown at various time points (horizontal axis). Images are scaled to the maximum value in the true image (top row).

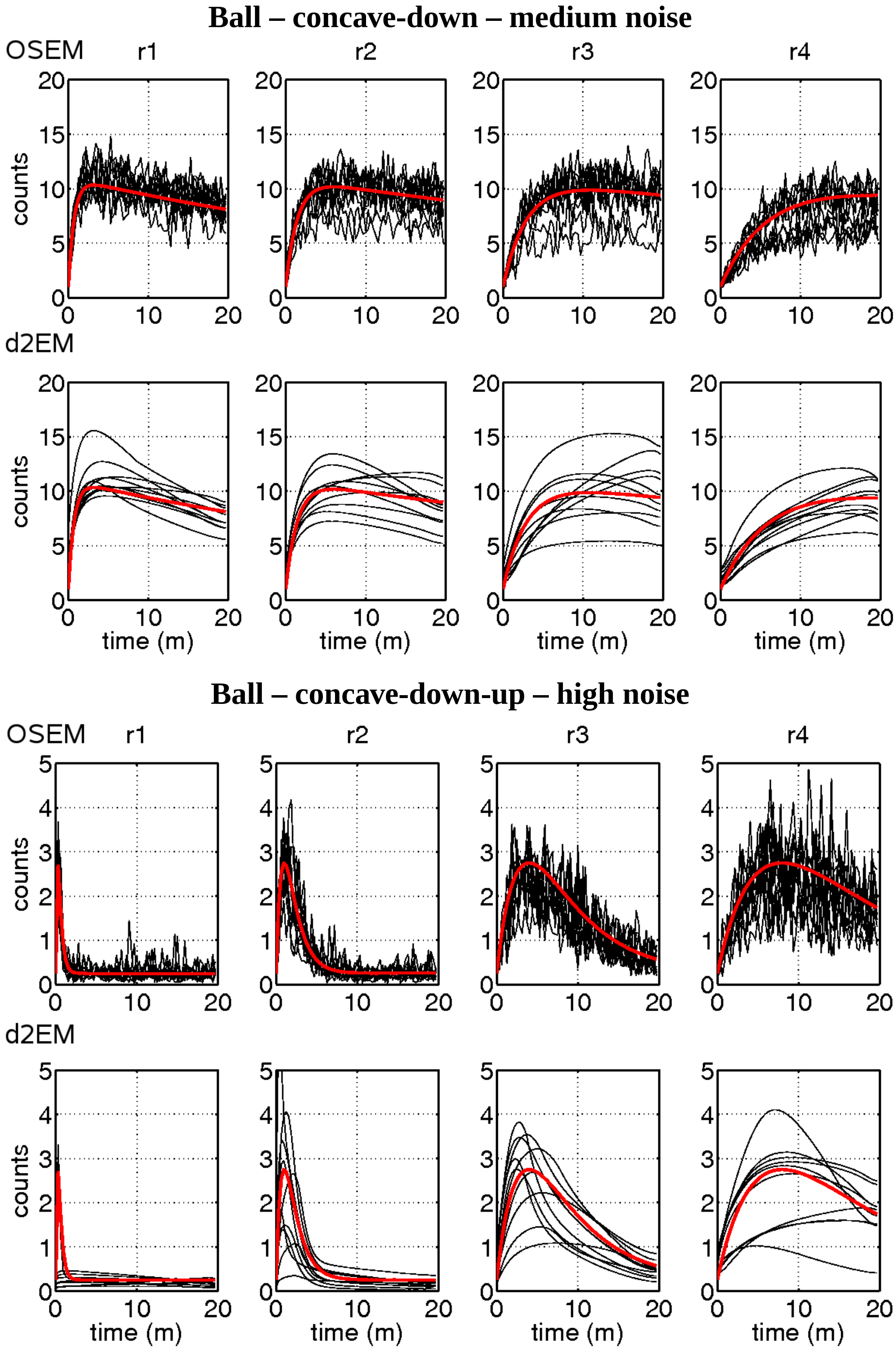

Figure 3.15: Representative TACs from voxels in the four different regions (r1, r2, r3 and r4) of the two selected reconstructed images after 6 iterations of OSEM (8 subsets) per frame (top row) and 80 iterations of d^{2}EM (bottom row). Red line shows true TAC for that region, while thin black lines show TACs from 10 randomly selected voxels within the region.

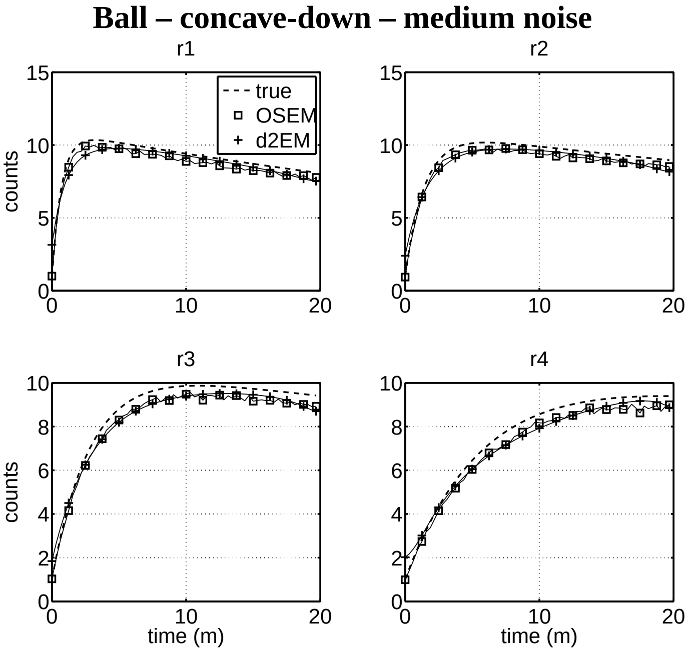

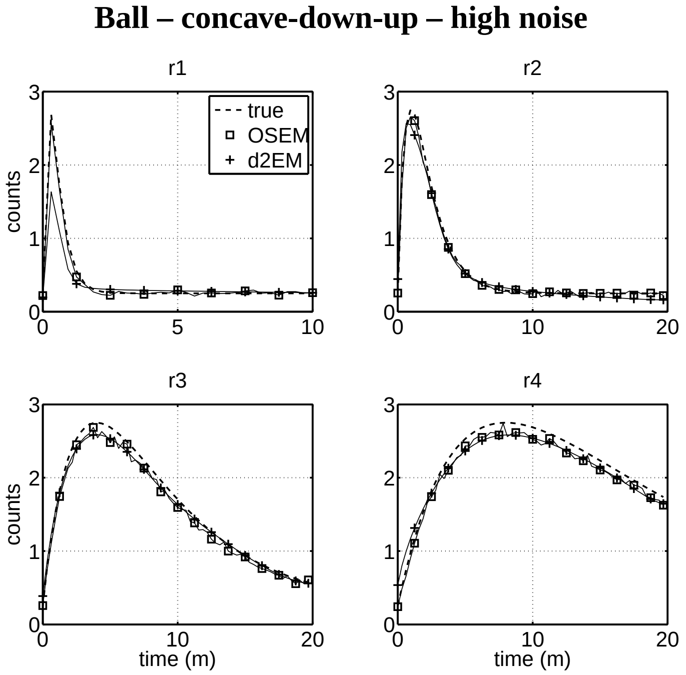

Figure 3.16: Mean time activity curves from the four different regions (r1, r2, r3 and r4) of the two selected reconstructed images after 6 iterations of OSEM (8 subsets) per frame and 80 iterations of d^{2}EM. Dashed line shows true TAC for that region, solid line with squares shows mean TAC for that region extracted from the OSEM image, and solid line with crosses shows mean TAC extracted from d^{2}EM image.

	ε	$\bar{\sigma}$	$\mathcal{S}$
OSEM avg.	5.1	24.2	16.5
d^2EM avg.	6.5	26.5	11.2
Improvement (%)	-26.6	-9.3	32.3
p-value	1.5E-4	6.0E-4	1.3E-6

Table 3.3: Summary statistics of error values presented in Table A.3, taken over all experiments.

$\bar{\sigma}$ within a region was never less than 15%, while in the high-noise simulations the values were typically in the range of 30-50%, using either method. Values of $\mathcal{S}$, on the other hand, were generally lower using d^2EM, aside from in regions with fast kinetics, as a result of the smoothness constraint imposed by d^2EM.

Summary statistics, calculated over all the experiments, are given in Table 3.3. These summaries exclude values from region 1 of the phantoms with concave-up-decreasing and concave-down-up TACs, which were considered to be outliers due to the poor performance of d^2EM in these regions. As mentioned previously, the dramatically larger error values for these regions obtained from d^2EM occurred largely as a result of the fast kinetics in these regions coupled with the limited projection data available to d^2EM. From the summary statistics, it is apparent that both ε and $\bar{\sigma}$ were significantly lower in the OSEM reconstructions, while $\mathcal{S}$ was significantly smaller using d^2EM. Nonetheless, this experiment has shown that the variation in TAC magnitudes observed in the d^2EM reconstructions is, to a large extent, intrinsic to the reconstruction problem itself. Given that this variation is visible even in images reconstructed using much more complete projection data and OSEM, it is not surprising that it is also apparent in the images reconstructed using d^2EM and dEM.

Chapter 4

Artifacts in slow-rotation dynamic SPECT

Single slow-rotation dynamic SPECT reconstruction is a very challenging problem, due to its highly underdetermined nature. Consider that in conventional SPECT reconstruction, it would be impossible to accurately reconstruct a image based on only one to three views of the object; yet in slow-rotation dynamic SPECT, this is typically the amount of data that is available for every time frame of the image. Approaches such as dEM and d^2EM are successful because the temporal constraints that they impose allow the reconstruction of any time frame of the image to be guided by geometric information acquired in earlier and later time frames. Nonetheless, there are consequences arising from the fact that the projection data corresponding to every time frame consists only of a small number of views.

In this chapter we identify and discuss artifacts that occur in dynamic SPECT images reconstructed from a single slow camera rotation, as a result of this fact. These artifacts can be divided into two categories: those caused by fast tracer kinetics, and those caused by the effects of attenuation and collimator blurring. Artifacts due to fast kinetics have been observed and discussed in other slow-rotation dynamic SPECT studies (e.g. [68, 16]), and we mention them here only briefly. Conversely, while the importance of correcting for attenuation (and to a lesser extent, collimator blurring) has been discussed in existing literature on slow-rotation dynamic SPECT (e.g. [20, 12, 16]), in this chapter we present new results and analysis indicating that past studies have not properly compensated for these effects. It is very challenging, in fact, to properly separate the effects of attenuation on projection data acquired by a slowly rotating camera from the effects of the actual tracer kinetics. In the last section of this chapter, we propose two post-reconstruction, template-based approaches to compensate for these artifacts. The effectiveness of these approaches is investigated in Chapter 5.

4.1 Artifacts due to fast kinetics

In many dynamic NM applications, the kinetic behaviour of the tracer is rapid compared to the acquisition time typically used in SPECT. Following injection of the tracer, for example, the concentration in the blood typically peaks sharply and then decreases to an equilibrium state in less than one minute. This means that if a region consisting of mostly blood (e.g. the right ventricle blood pool of the heart) is being imaged, then its dynamic behaviour is captured by only a small number of views acquired by a slowly rotating camera. Thus, there is insufficient angular information to accurately reconstruct these regions.

An analogy can be drawn to static SPECT reconstruction where views over fewer than 180° are acquired. Figure 4.1 shows an example from a simple digital phantom simulation. The geometry of this static phantom was the same as the ball geometry used in the phantom experiments of Chapter 3, with activity concentration of 10 units/voxel inside the four small regions and 1 unit/voxel in the background region. The projection data corresponding to the 180° acquisition (left column) consisted of 32 views, while the data used for the reconstruction in the right column simulated two detectors at 90° to one another, acquiring eight views each over 45°. Since the data used to reconstruct the images in the right column were incomplete, noticeable streaking is visible, and the circular regions themselves are distorted.

Similar effects are visible in images reconstructed using dEM or d^{2}EM, when rapid kinetics are present in some regions. Figure 4.2 shows reconstructions of the concave-down-up phantom used in Chapter 3, which featured relatively fast kinetics in regions 1 and 2. (See Figure 3.2 and Table 3.1 for the phantom description). The kinetics in region 1, in particular, consisted of complete uptake and washout of the tracer within the first two minutes, at which point each camera head in the simulated acquisition had rotated only about 33°. Thus, region 1 appears distorted in the images reconstructed using either dEM or d^{2}EM (bottom two rows of Figure 4.2, red circled region). The nature of this distortion is

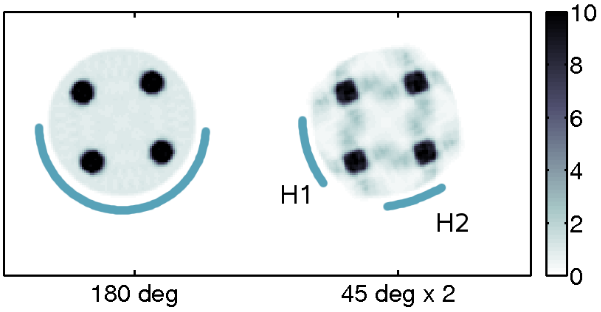

Figure 4.1: Simulation showing image artifacts caused by insufficient angular sampling in static SPECT reconstruction. Images were reconstructed using 20 iterations of MLEM. Arcs indicate the angles over which projection views were taken for both cases. Projection data did not include attenuation, collimator blurring or noise.

very similar to the one observed in the static image in Figure 4.1. If 64 views of the object are available for every time frame, as in the top row of the figure (where each frame was independently reconstructed using OSEM), this distortion is not present. Region 2 is also somewhat distorted in the images reconstructed with dEM and d^{2}EM, due to its relatively fast kinetics, while regions 3 and 4 are well-reconstructed. This effect was observed in Section 3.6 of the previous chapter, when comparing images reconstructed with d^{2}EM against the images reconstructed using OSEM based on complete angular information.

4.2 Artifacts due to attenuation

None of the simulations studied so far have included the effects of collimator blurring or attenuation. As discussed in Chapter 1, these physical factors degrade image quality if they are not accounted for in the reconstruction algorithm. In slow-rotation dynamic SPECT, it is particularly important to account for the effects of attenuation, since the varying amount of attenuating material between a dynamic region and the detector, caused by rotation of the camera, produces similar effects on the projection data as the actual kinetic behaviour of the tracer in that region. If the detected counts corresponding to some region diminish as the camera rotates, for instance, then this may occur as a result of washout of the tracer, or due to an increased amount of attenuating material between that region and the camera.

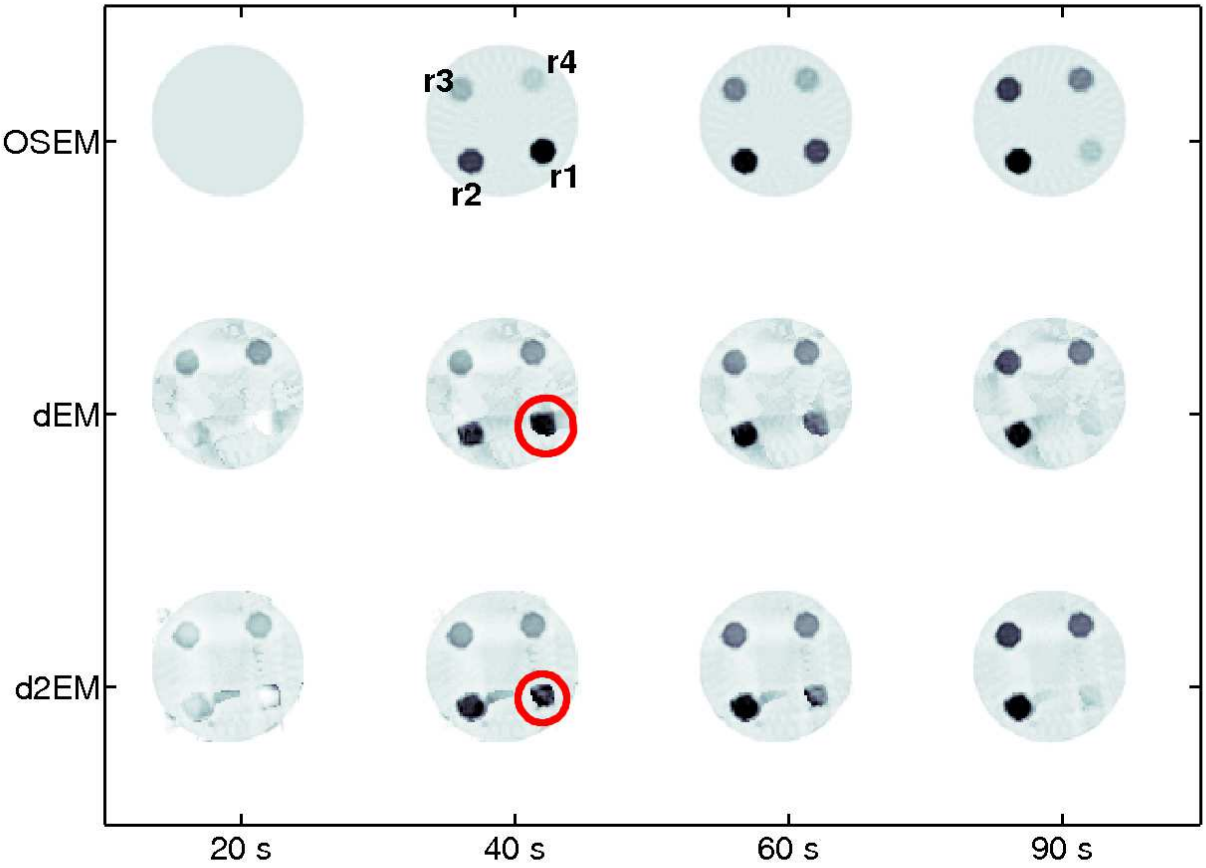

Figure 4.2: Image artifacts caused by fast kinetics in slow-rotation dynamic SPECT reconstruction. Top row: time frames of image reconstructed using 6 iterations of OSEM (8 subsets) with 64 views around the object for each time frame. Bottom two rows: time frames of images reconstructed using 80 iterations of dEM and d^{2}EM, respectively, with only two views of the object per time frame. X-axis shows the time frame (in seconds) corresponding to each column. The red circle indicates region 1, which was poorly reconstructed. Projection data did not include attenuation, collimator blurring or noise.

In conventional SPECT image reconstruction using iterative methods such as MLEM, the effects of attenuation and collimator blurring are typically included in the system matrix, ensuring that they are accounted for during the forward and backward projection steps of the reconstruction algorithm. Since the system matrix used in slow-rotation approaches such as dSPECT is simply a reordering of the conventional system matrix C into a block diagonal matrix C' (see Figure 1.7), it stands to reason that the effects of attenuation and collimator blurring can be accounted for in dSPECT simply by incorporating them into the dynamic system matrix. This has been the approach taken in previous dSPECT studies (e.g. [19, 12, 18]). In this section, however, we show that simply modeling attenuation and collimator blurring in the dynamic system matrix does not adequately correct for their effects during image reconstruction. We will focus on effects caused by attenuation, as they are much more severe than those caused by collimator blurring.

As in the previous section, an analogy can be made to static SPECT reconstruction. One established property of MLEM is that including attenuation and depth-dependent resolution in the system matrix does not uniformly correct for their effects in the reconstructed image [30]. An example is presented in Figure 4.3, using the same static phantom as in Figure 4.1, but including attenuation with coefficient $\mu = 0.15$ cm^{-1} within the object. The value $\mu = 0.15$ cm^{-1} was used because this is the attenuation coefficient for 140 kEV photons (such as those emitted by $^{99\text{m}}$Tc) in water. The phantom is 128×128 voxels, with a voxel size of 5 mm/side.

When views are only taken over a 180° arc (centre column of Figure 4.3), regions on the opposite side of the object (r3 and r4) are severely distorted due to attenuation. Many iterations of MLEM are required to eliminate this effect (see bottom row); typically, more iterations than are practical in the presence of noisy data. Only with views taken over 360° (right column) does MLEM accurately compensate for attenuation within a reasonable number of iterations, providing accuracy comparable to the case where no attenuation is present (left column). Even if views are taken over 360°, however, regions in the centre of an attenuating medium can suffer from similar effects; see Figure 2 in [30], for example.

We now extend this reasoning to single slow rotation dynamic SPECT. If a dual-head camera is used, the projection data corresponding to every time frame consists of only two views of the object – usually from heads placed at 90° to one another. In these two views, counts from regions on the far side of the object are more attenuated than from regions on

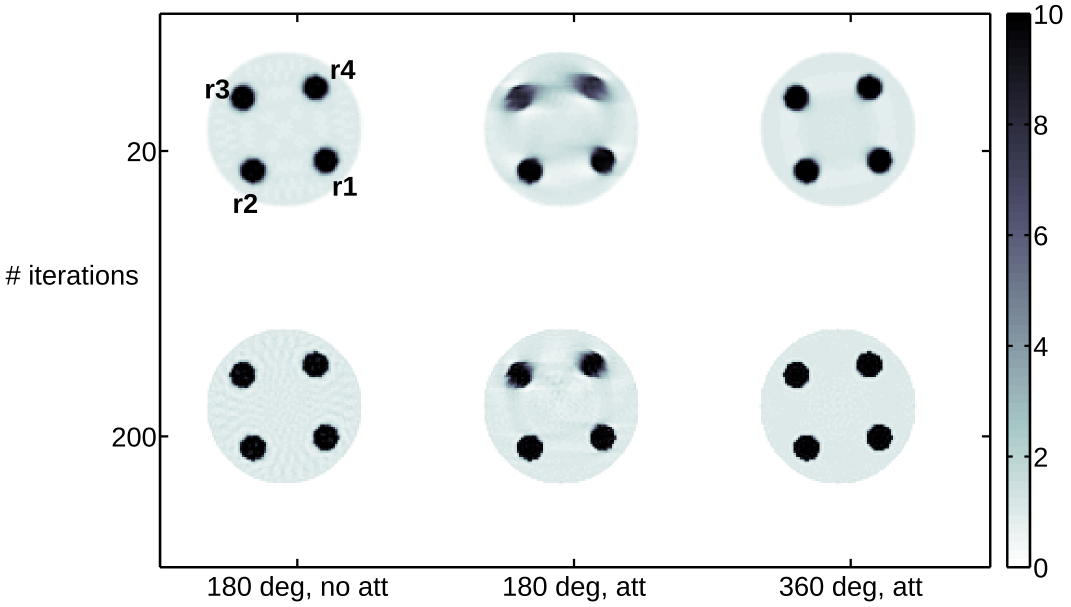

Figure 4.3: Simulation consisting of static images reconstructed after 20 and 200 iterations of MLEM, showing effects of attenuation. Image reconstructions in centre and right columns included attenuation with $\mu = 0.15$ cm^{-1} within the object. Projection data did not include noise or collimator blurring, and consisted of 32 views over the bottom 180° arc for left and middle columns, and 64 views over 360° for the right column.

the near side. As was the case in the static image reconstruction shown in Figure 4.3, the quality of the reconstructed image on the far side of the object at any time frame suffers as a result, despite the inclusion of attenuation modeling in the system matrix.

We demonstrate this fact with another simple phantom experiment using the ball geometry. In this experiment, all four dynamic regions had the same dynamic behaviour, corresponding to the TAC from region 3 of the concave down-up phantom (see Figure 3.2). Acquisition was once again modeled as a dual-head, 90° mode acquisition where each head made 64 stops over a 360° counterclockwise rotation, with the heads starting on the left and bottom sides of the object. Two sets of projection data were created: one without attenuation, and one assuming $\mu = 0.15$ cm^{-1} inside the object. Images were then reconstructed using 80 iterations of dEM, using the appropriate system matrix (i.e. with or without attenuation modeling). Noise and collimator blurring were not included in the projection data. Since the kinetic behaviour in each of the four regions (r1 – r4) was identical, any discrepancies in the TACs reconstructed in each region must have occurred as a result of attenuation effects.

Time frames of the reconstructed images, and mean TACs extracted from them, are shown in Figure 4.4. The mean TACs for the attenuation-free image (circular markers) are the same in all four regions, but the TACs in the image with attenuation (cross markers) vary considerably due to attenuation effects. For instance, since the heads remained close to r1 through the first 10 minutes of the acquisition, when the activity concentration was changing most rapidly, the effect of attenuation on the TAC for this region is negligible. In r3, which was on the opposite side of the object from the camera heads through much of the first 10 minutes of acquisition, the TAC is severely depressed. Effects due to attenuation are also visible in the TACs for r2 and r4.

The choice of reconstruction algorithm has an impact on the severity of these effects. Figure 4.5 shows results of the same experiment, using 80 iterations of d^{2}EM to reconstruct the images instead of dEM. The artifacts the TACs extracted from r2, r3 and r4 are now less severe, although in r4, a different artifact is present in the last 5 minutes of the TAC. It must be noted, however, that the reduction in the severity of artifacts does not occur because d^{2}EM compensates for attenuation any differently from dEM. Rather, its stronger constraint on the concavity of the TAC in every voxel has simply prevented the occurrance of some of the artifacts that were present in the images reconstructed using dEM.

Unlike the artifacts shown in the static MLEM reconstruction of Figure 4.3, these artifacts are not eliminated even after many iterations of dEM or d^{2}EM. This is likely due to the underdetermined nature of the slow-rotation dynamic reconstruction problem; the reconstructed image, although incorrect, still provides a good fit to the projection data. While the static reconstruction example was also solving an underdetermined problem – 32 views consisting of 128 bins were used to reconstruct a 128×128 voxel image – the solution space was not as large as in the dynamic case, and so the artifacts on the far side of the object eventually had to be resolved in order to fit the projection data.

Simulations where only the effects of collimator blurring were included show analogous results. The TACs for the regions that were farther from the two camera heads during the

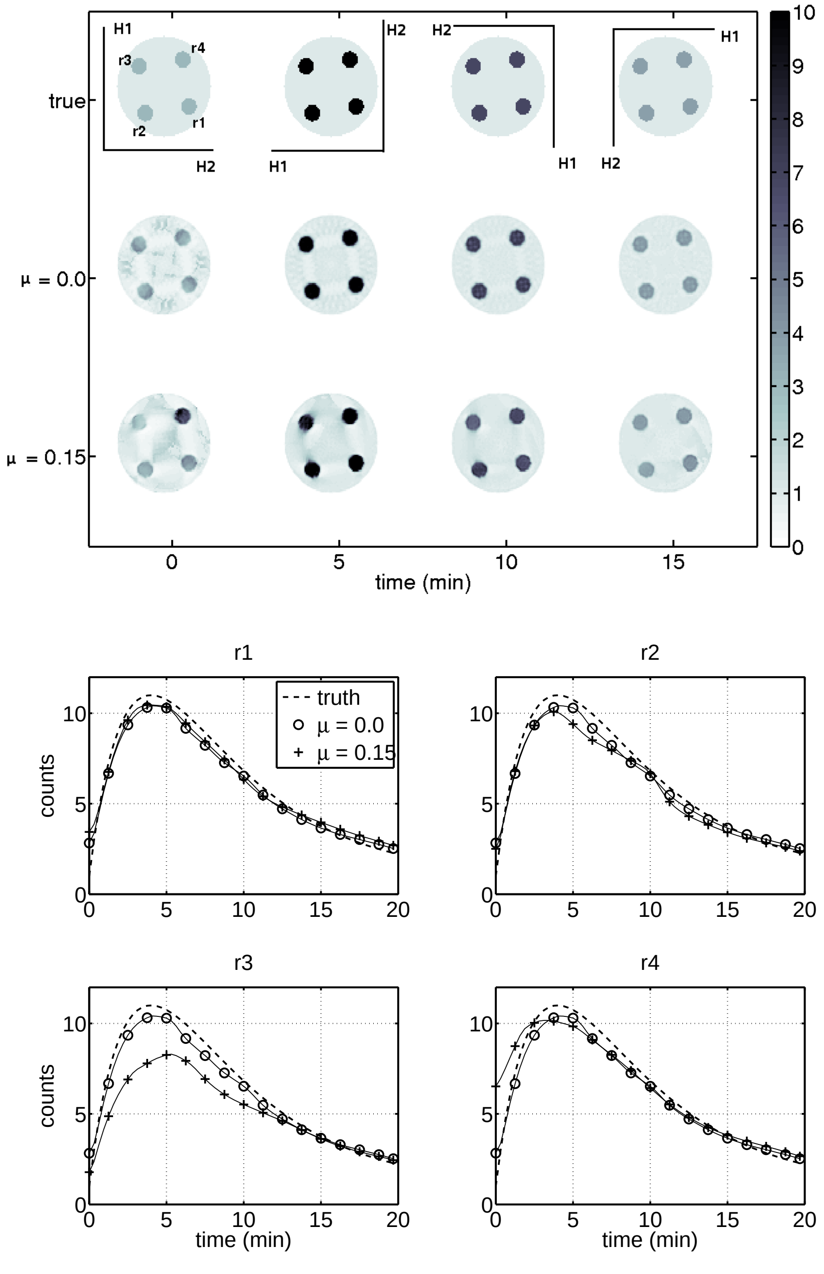

Figure 4.4: Images and TACs reconstructed using dEM, showing the effects of attenuation. Top figure: Top row shows time frames of true image, with position of camera heads (H1 and H2) at each time point; middle row corresponding frames from image reconstructed using 80 iterations of dEM, without any attenuation; bottom row shows frames from image reconstructed using 80 iterations of dEM including attenuation. Bottom figure: mean TACs extracted from each of the four dynamic regions r1–r4.

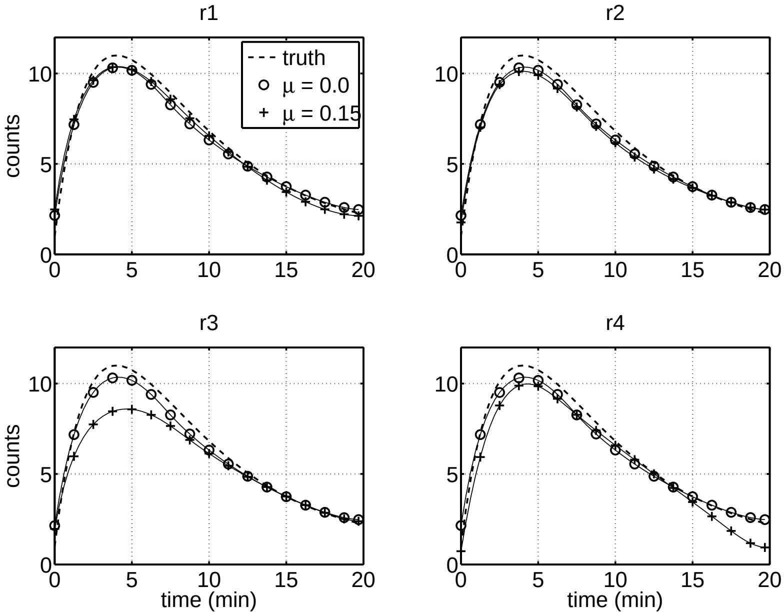

Figure 4.5: Mean TACs extracted from four dynamic regions in image reconstructed using 80 iterations of d^{2}EM. Compare to TACs shown in Figure 4.4.

early stage of the acquisition (e.g. r3) were underestimated compared to the TACs for regions that were close to them (e.g. r1). This occurs for the same reason as for the artifacts caused by attenuation: at every stop made by the camera, regions that are far from the camera are more blurred than regions that are close, and the inclusion of collimator blurring in the system matrix does not uniformly correct for this effect. For realistic levels of blurring, however, the effect was minor compared to the artifacts caused by attenuation.

It is interesting that these effects have not been noted in previous studies on slow-rotation dynamic SPECT. Indeed, one study specifically examined the inclusion of collimator blurring into dSPECT reconstruction [20], and many dSPECT studies have included attenuation effects [19, 12, 18]. All of these studies simply included attenuation and collimator blurring in the system matrix, which we have demonstrated to be insufficient to account for their effects. However, these studies usually featured centrally-located dynamic objects, for which the effects of attenuation or collimator blurring would not vary nearly as much during acquisition as in the examples considered here. Thus, any errors introduced by these effects would have been more subtle, and probably attributed to the difficult nature of the reconstruction problem. Some experiments have also used triple-head cameras, where attenuation effects would be less noticeable since the camera heads were evenly distributed around the object at 120° intervals.

One paper using FADS-based reconstruction[1], however, featured several digital phantom experiments which simulated dynamic renal studies, where attenuation between the camera and the two dynamic regions representing the kidneys varied considerably during acquisition [68]. Since the approach proposed in this paper uses data acquired with a single slow camera rotation, the same attenuation effects should have been apparent. While this paper did not note any such effects, the tabulated results (Table 1 in the paper) indicate that they may have been present. In several simulations modeling single and dual-head acquisitions, errors in the reconstructed TACs varied by up to 2-3 times in magnitude depending on the initial position of the camera heads. Failure of the algorithm to properly compensate for attenuation would seem to be the most likely reason for these discrepancies, since the effect of attenuation on the two dynamic regions would have been the factor that varied the most in these different acquisitions.

4.3 Template-based correction

We now consider how to correct for these artifacts in the reconstructed images. It is not clear how to accomplish this during the actual reconstruction of the image. In principle the physical effects are being modeled correctly in the system matrix; the root of the problem is the fact that only a small number of views corresponding to each time frame of the image are acquired – which is a fundamental component of single slow-rotation dynamic SPECT reconstruction. Thus, we consider how these artifacts can be treated after reconstruction of the image. A post-reconstruction approach is challenging as well, since the artifacts created in different regions of the image by attenuation depend on numerous factors such as the acquisition protocol, object geometry, tracer kinetics and reconstruction algorithm. In this section we propose two approaches.

The first approach is a modification to one that has previously been applied to partial volume effect (PVE) correction in static SPECT imaging [64]. The PVE occurs as a result of both the limited resolution of the SPECT system and the discretization of image space

---

[1] This method is described in Section 1.2.

into voxels, which make it impossible to determine the exact location of activity sources inside the object being imaged. The net effect is that the reconstructed activity concentrations along the borders of adjacent regions tend to mix, resulting in low contrast between these regions. A common example is "spill-out" of activity from regions of high intensity into the surrounding lower-intensity background. Since the severity of PVE depends on factors such as the geometry of the different ROIs and the relative concentrations of activity between adjacent regions, it is difficult to compensate for PVE during the actual reconstruction of the image. Hence, post-reconstruction corrections are often used [73].

In the method proposed in [64], a static image, x, is first reconstructed using OSEM, with full correction for attenuation, collimator blurring and scatter. A digital template image having the same dimensions as x, denoted y, is then created by segmenting the original image into several ROIs. The activity concentration in each ROI of the template is made spatially uniform, and proportional to the ratio of activity concentration in that region to the background. Projection data of the template image are then analytically created, simulating the same protocol that was used to acquire the measured data. This projection data is then input to OSEM and reconstructed using the same parameters as were used to reconstruct the original image. By comparing the reconstruction of the template, denoted $R(y)$, to the original template y, the severity of PVE in different regions of the image can be assessed and the original image, x, can be corrected. The assumption is that any artifacts present in $R(y)$ versus y are similar to those present in x versus the true distribution of activity.

Since the dynamic SPECT image artifacts we observed in the previous section depend on the time-varying concentration of activity within regions of the image, this method must be adapted to the dynamic context. The modified method, illustrated in Figure 4.6, is as follows:

1. The dynamic image x' is reconstructed from the acquired projection data. In principle any single slow-rotation dynamic SPECT algorithm could be used, though here we restrict ourselves to dEM and d^{2}EM.

2. The image is segmented into ROIs assumed to have consistent dynamic behaviour. Depending on the situation, this segmentation could be created based on the image x' itself, or on a co-registered CT image. The dynamic digital template, y', is then

created by extracting the average TAC from each ROI and assigning it to every voxel in that ROI.

3. Projections of y' are created by multiplying it by the dynamic system matrix C', including the effects of attenuation and collimator blurring, to simulate the same protocol that was used to acquire the measured data p.
4. These projection data are used as input to the reconstruction algorithm, to produce a reconstructed dynamic template $R(y')$.
5. A correction factor for every voxel at every time frame is determined by taking the ratio of y' to $R(y')$. The final, corrected image is thus given by

   $$x'_C = x' \times \frac{y'}{R(y')}, \tag{4.1}$$

   where all operations have been applied voxelwise in every time frame.

The main advantage of this method, which we denote as the “CF” (correction factor) approach, is that is models the introduction of artifacts by the reconstruction process, meaning that it is fairly generic and able to account for effects that are complicated and may be difficult to anticipate *a priori*. The method is, however, based on the assumption that any artifacts introduced during the reconstruction of the template image are similar to those introduced during the reconstruction of the original image. In the presence of moderate to severe artifacts in the original image reconstruction x', the template may be sufficiently different from the truth that the same artifacts will not be reproduced. In this case, the correction factor determined in the last step may be too large (resulting in overcompensation) or too small. Since the correction factor is applied as the final step of this approach, there is no mechanism to compensate for any errors in the correction.

Our second approach, then, integrates the use of the template into the reconstruction process. In this approach, the image is reconstructed and the template is created, as in the first approach. Instead of creating projections of the template, however, the template is used as an initial estimate in a second run of the reconstruction algorithm. This second run uses the original measured projection data as input; the only difference from the first run of the algorithm is that the template is used as an initial estimate, rather than a generic, uniform image. This approach is illustrated in Figure 4.7.

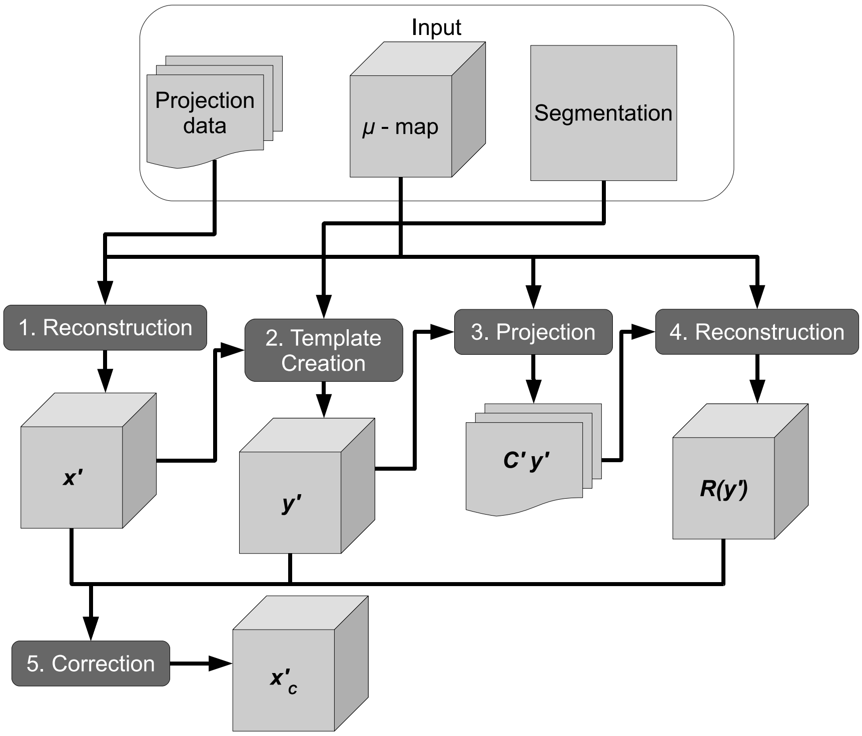

Figure 4.6: Flow diagram indicating steps and data used in CF-based dynamic template correction method.

The rationale for this approach is that the incorrect dynamic image containing attenuation artifacts is still a valid solution, in the sense that it provides a good fit to the projection data under the assumed system model. The correct dynamic image is also a valid solution, to which the reconstruction algorithm has failed to converge, due to the insufficient compensation for attenuation effects during the reconstruction. By starting with an initial estimate that is closer to the correct image than the generic initial estimate used to generate the first image, it may be possible to reduce the severity of the attenuation artifacts. This approach, which we denoted as the “IE” (initial estimate) approach, is somewhat safer than the CF approach since the correction occurs in the context of the reconstruction algorithm. Since the final corrected image represents a fit to the measured projection data, it is less likely that it will contain overcorrections or other errors that could result from the application of the CF method. This approach does not, however, attempt to model or determine

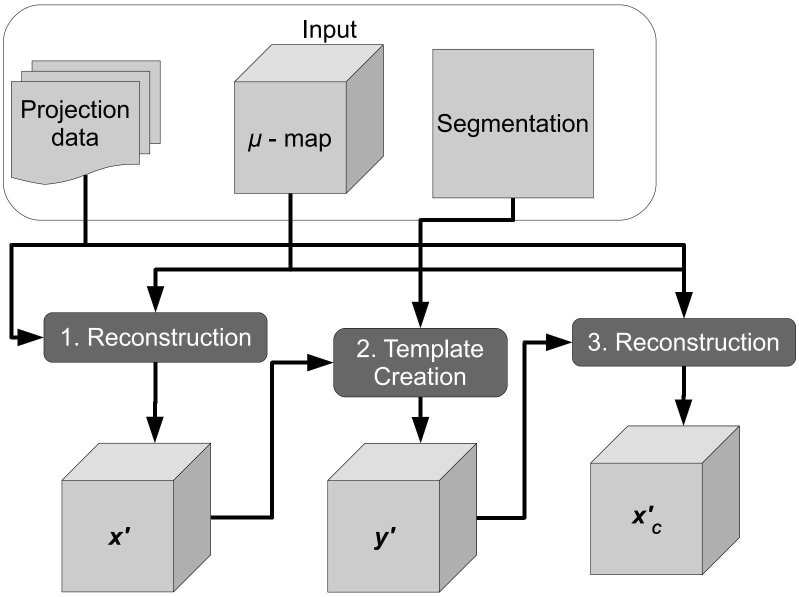

Figure 4.7: Flow diagram indicating steps and data used in IE-based dynamic template correction method.

the nature of any artifacts that are present in the original reconstruction.

Both the CF and IE approaches require additional reconstruction time, since they require a second run of the reconstruction algorithm. For the CF approach, the reconstruction time is doubled since the same number of iterations must be run as were run in the original reconstruction, in order to properly replicate image artifacts. In the IE approach, fewer iterations may be necessary in the second run, since it begins with a better initial estimate. The accuracy of both methods will also be affected by the quality of the segmentation, and how well the the true dynamic distribution of activity can be modeled as a group of ROIs with spatially homogeneous behaviour.

Figure 4.8 shows the result of applying these two correction methods to the simulation shown in Figure 4.4. In this case, the segmentation used to create the template was based on the true boundaries of the four dynamic regions, which were known from the phantom. For the IE method, only 40 iterations of dEM were performed in the second run, which is half the number used in the first run. Both methods have introduced similar improvements to regions 1, 2 and 4 of the image. In region 2, the corrected TACs are in much better

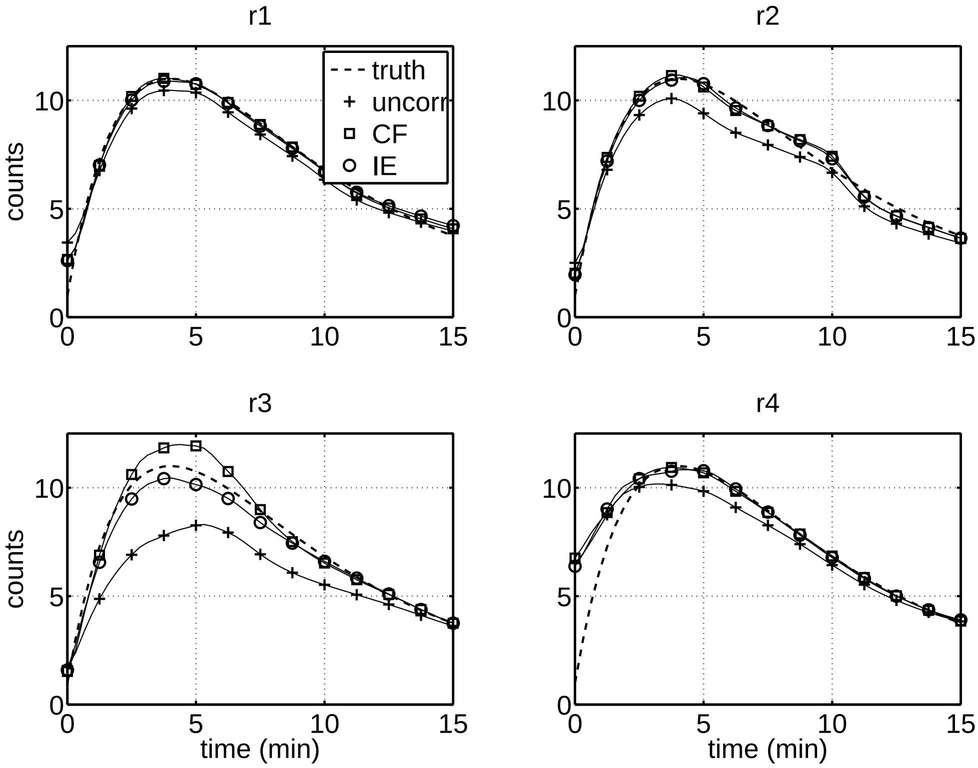

Figure 4.8: Results of applying the CF and IE template corrections to the 2D phantom simulation shown in Figure 4.4. Plots show the true TAC for each region, as well as the mean TACs extracted from the uncorrected image, the image corrected with the CF method, and the image corrected with the IE method.

agreement with the truth than the uncorrected TAC; however, an artifact that caused the TAC to flatten slightly between 6 and 10 minutes has persisted. In region 4, neither method was able to correct for a sizeable overestimation in the first three minutes, although the agreement of the reconstructed TACs with the truth has been improved in later time frames. Region 3 is the only one wherein the correction introduced by the CF approach differed substantially from that introduced by the IE approach. The CF approach has resulted in an overcorrection between the 3rd and 7th minutes, while the IE approach has not. The IE-corrected image underestimates the TAC slightly, but overall the correction seems better than that provided by the CF method.

Overall, these approaches have been successful in correcting for some mild artifacts, but not for more severe ones. It must be noted that the most severe artifacts occurred in r3 and r4, which were on the opposite side of the object at the beginning of the acquisition. In a real-life study, this acquisition protocol would not have been chosen if r3 and r4 were the most important regions to be imaged. Thus, the choice of a sensible acquisition protocol, in addition to the application of one of these corrections, is essential to reduce any artifacts caused by attenuation. Accordingly, in the next chapter we investigate the effects of realistic acquisition protocols on a 3D simulation of a dynamic renal scan, and assess the effectiveness of these methods in correcting for any artifacts.

Chapter 5

3D simulations and experiments

One potential clinical application of dynamic SPECT is assessment of renal function by examining washout of the tracer $^{99\mathrm{m}}$Tc-DTPA in the kidneys. $^{99\mathrm{m}}$Tc-DTPA is an imaging agent which is excreted by the kidneys in a process known as glomerular filtration. Following injection, the tracer enters the renal cortex (the outer shell of the kidney, illustrated in Figure 5.1) via the renal arteries. During glomerular filtration, the tracer filters into the medulla before collecting in urine in the centrally located renal pelvis. From there, it is transported through the ureter into the bladder [75].

Current clinical protocol for dynamic renal imaging using $^{99\mathrm{m}}$Tc-DTPA consists of a planar dynamic renogram acquired posteriorly. By drawing 2D ROIs over the regions of the image corresponding to the left and right kidneys (excluding the pelvis), it is possible to obtain a TAC for each kidney as a qualitative measure of renal function. Impaired function or obstruction in either kidney is typically indicated by high retention of the tracer within the kidney. Accurately compensating for patient-specific attenuation and effects due to organ overlap is impossible in a planar scan, although approximate corrections are often used. As a result, one cannot obtain reliable quantitative information from these scans. Both of these effects could be accounted for using the 3D information present in a dynamic SPECT scan, which would allow for a more reliable quantitative assessment of renal function.

In this chapter we investigate reconstruction of dynamic renal SPECT images based on slow-rotation data, using digital phantom simulations as well as two sets of real-life data. Attenuation artifacts of the type discussed in the previous chapter may be especially problematic for renal scans, since the effects of attenuation on either kidney varies consid-

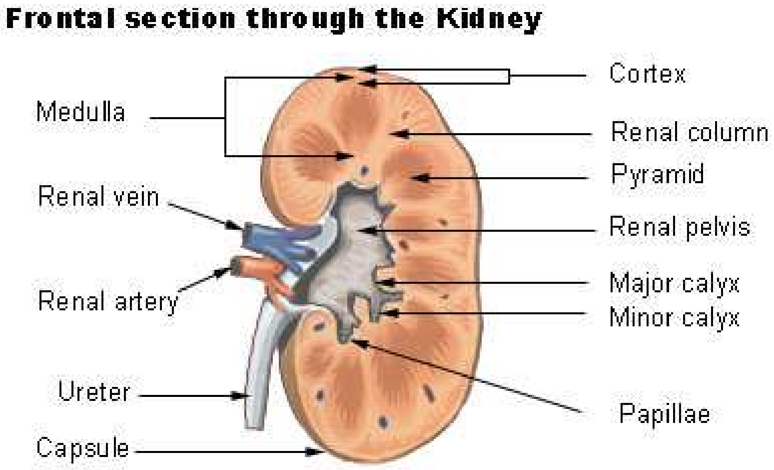

Figure 5.1: Diagram of renal anatomy, showing the renal cortex, medulla and pelvis. Retrieved from the U.S. National Cancer Institute's Surveillance, Epidemiology and End Results (SEER) website, `http://training.seer.cancer.gov/anatomy/urinary/components/kidney.html` on June 7, 2011.

erably during the acquisition of projection data. Assessing the severity of these effects on the reconstructed images is one goal of the experiments in this chapter. We also assess the effectiveness of the methods proposed in Chapter 4 to correct for any artifacts introduced by attenuation, as well as continue to investigate the performance of d^{2}EM versus dEM.

5.1 3D renal phantom

5.1.1 Phantom construction

A dynamic renal phantom was created in two stages. First, an anatomical map consisting of 64×64×64 voxels (voxel size 9.3mm/side) was created using the 3D NCAT digital phantom, which provides a realistic, 3D model of the human torso [63]. NCAT was used to create an attenuation map of the phantom, and to determine organ boundaries corresponding to dynamic regions in the left and right kidneys, left and right ureters, and bladder. In this simulation the region corresponding to each ureter also included the renal pelvis. In the second step, tracer kinetics modeling the uptake and washout of ^{99m}Tc-DTPA in the renal system were simulated using a compartmental model, illustrated in Figure 5.2. This compartmental model describes the absorption of $^{99\mathrm{m}}$Tc-DTPA from the blood into the kidneys, followed by transit through the pelves and ureters into the bladder. Uniform background activity is modeled, but no modeling of uptake in other organs (e.g. the liver or lungs) is included. The compartmental model is described by a system of ordinary differential equations (ODEs):

$$\begin{aligned}
\frac{\mathrm{d}}{\mathrm{dt}}A_{Bl}(t) &= I(t) - 5(k_{BRK} + k_{BLK})A_{Bl}(t) \\
\frac{\mathrm{d}}{\mathrm{dt}}A_{RK}(t) &= k_{BRK}A_{Bl}(t) - k_{RKU}A_{RK}(t) \\
\frac{\mathrm{d}}{\mathrm{dt}}A_{LK}(t) &= k_{BLK}A_{Bl}(t) - k_{LKU}A_{LK}(t) \\
\frac{\mathrm{d}}{\mathrm{dt}}A_{RU}(t) &= k_{RKU}A_{RK}(t) - k_{RUBd}A_{RU}(t) \\
\frac{\mathrm{d}}{\mathrm{dt}}A_{LU}(t) &= k_{LKU}A_{LK}(t) - k_{LUBd}A_{LU}(t) \\
\frac{\mathrm{d}}{\mathrm{dt}}A_{Bd}(t) &= k_{RUBd}A_{RU}(t-\delta) + k_{LUBd}A_{LU}(t-\delta) \\
\frac{\mathrm{d}}{\mathrm{dt}}A_{Bg}(t) &= 4(k_{BRK} + k_{BLK})A_{Bl}(t)
\end{aligned} \tag{5.1}$$

The seven time-dependent functions A_{Bl}, A_{RK}, A_{LK}, A_{RU}, A_{LU}, A_{Bd} and A_{Bg} correspond to the total activities in the compartments representing the blood, right kidney, left kidney, right ureter, left ureter, bladder and background, respectively. $I(t)$ is the input function, which was represented by an initial impulse equivalent to an injection of 370 MBq of tracer. The subscripted k values represent transfer coefficients between the compartments (see Figure 5.2), and were varied to simulate different behaviours, as described later. Since only 20% of the injected dose of $^{99\mathrm{m}}$Tc-DTPA is typically taken up in the renal system, the transfer coefficient to the background is defined to be four times larger than the sum of the coefficients for the left and right kidneys. Due to the much larger size of the background region, however, the actual concentration of tracer in the background was only roughly 5% that of the peak concentration in the kidneys, in the actual phantom. A value of $\delta = 7.5$ seconds was used in order to simulate delayed uptake in the bladder.

The system of ODEs was solved numerically to determine the time-dependent total

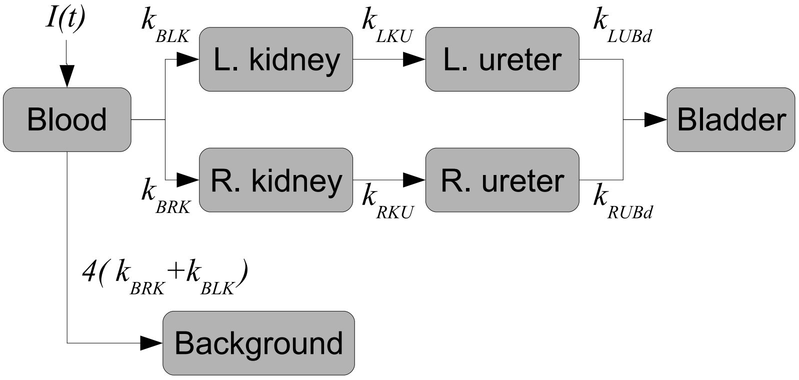

Figure 5.2: Compartmental model used to generate TACs for the different anatomical regions in the dynamic digital phantom. Differential equations governing the compartmental model are provided in Equation (5.1).

activity in each region. These curves were integrated in 20 second intervals to provide a total activity value for each region during every 20 second frame. This activity value was then divided by the total number of voxels to provide a uniform concentration inside each region. The blood activity, $A_B(t)$, was not assigned to any voxels in the image; it simply served as input to the compartmental model. Two types of renal behaviour, healthy and unhealthy, were modeled. The parameter values used to generate these two behaviours, along with the time of peak activity ($T_{\max}$) and effective half-life ($T_{\frac{1}{2}}$) which resulted are shown in Table 5.1. These values were chosen to simulate dynamic behaviours that were similar to those in sample planar renogram obtained from a local hospital. Six different cases (denoted A–F), summarized in Table 5.2, were simulated using different combinations of healthy and unhealthy behaviour in either kidney.

Projections of the phantom were computed using the Analytic Photon Distribution with Interpolation (APDI) method [79, 76]. This method created noiseless projections of the activity distribution, including the effects of depth-dependent resolution and attenuation. A general-purpose collimator (hole length 42 mm, hole width 1.78 mm) was simulated. The APDI method was used so that the system matrix used to generate the projections was not the same as the one used in the reconstruction algorithm, as would be the case

	k_{BRK}, k_{BLK}	k_{RKU}, k_{LKU}	k_{RUBd}, k_{LUBd}	T_{max}	$T_{\frac{1}{2}}$
Healthy	0.2	0.3	1.0	100	290
Unhealthy	0.2	0.03	0.1	200	2135

Table 5.1: Kinetic coefficient values used in the compartmental model (Figure 5.2) to generate the healthy and unhealthy kinetic behaviours in each organ. Unhealthy behaviour was simulated by kidney-to-ureter and ureter-to-bladder coefficients that were 10% the value of the healthy coefficients. T_{max} and $T_{\frac{1}{2}}$ values are given in seconds.

Case	Left kidney	Right kidney
A	healthy	healthy
B	unhealthy	unhealthy
C	unhealthy	healthy
D	healthy	unhealthy
E	33% unhealthy	healthy
F	healthy	33% unhealthy

Table 5.2: Description of the dynamic behaviour in each kidney for the six renal phantom simulations. Healthy or unhealthy behaviour (see Table 5.1) was simulated in either kidney. In cases E and F, the unhealthy behaviour was present in the bottom 33% of the specified kidney, with the rest of the kidney having healthy behaviour.

with data acquired on a real system. Poisson noise was added to the projection data after computation. Based on the maximum pixel intensity in the regions corresponding to the kidney, the noise level was roughly 5–6%. Since the generation of projections using APDI simulates a realistic acquisition, the images reconstructed from APDI projection data had to be scaled by a normalization factor in order to directly compare them to the original phantom. Based on a point source simulation, this normalization factor was determined to be 1.0087×10^{-4}.

5.1.2 Experiment 1: Effect of acquisition

As seen in Chapter 4, the effects of attenuation on the projection data as the camera rotates can cause substantial errors in the TACs extracted from dynamic regions. Tomographic dynamic renal scans may be particularly affected, since the two kidneys are located off-centre, meaning that the effects of attenuation on each kidney will vary more during acquisition than they would for a centrally-located object. This could have serious implications in evaluation of renal function, since the split function (i.e. the proportion of total renal function attributed to each of the kidneys) is often a quantity of interest. If the reconstructed TACs corresponding to either kidney are differently affected by attenuation, then an incorrect evaluation of split function could occur.

In order to assess the potential severity of such artifacts, we simulated four different acquisitions for each of the four renal phantoms A–D. Cases E and F were omitted in this experiment. The four acquisitions, which were numbered I–IV, all consisted of two detectors at 90° to one another, each making 48 stops over a 360° rotation, with each stop lasting 20 seconds. The two parameters that were varied were the initial position of the detectors and the direction of rotation, although all four acquisitions were chosen sensibly so that the camera acquired data posteriorly during the early part of the scan. The projection data were then input to both the dEM and d^2EM algorithms to produce reconstructed images. Sixty iterations of dEM were used to generate each image, while eighty iterations of d^2EM were run, since its convergence was slower than dEM's in some cases. Mean TACs for the left and right kidneys were extracted from each image using the true organ boundaries, and the relative error in the mean TAC, ε, which was used in the 2D phantom experiments of Chapter 3, was computed. Full results of the experiment are presented in Table 5.3, and summarized in Table 5.4. Figure 5.3 shows an example of the reconstructed mean TACs for the simulation using Phantom D.

Several trends are apparent from the statistics presented in Table 5.4. In the experiments as a whole, the errors in the right kidney tended to be larger than errors in the left kidney, possibly due to the fact that the right kidney was approximately 10% smaller than the left kidney in the NCAT geometry. The right kidney's smaller size likely made it more challenging to reconstruct accurately. Also, the value of ε when the kidney featured healthy behaviour (fast washout) was typically larger than when the kidney featured unhealthy behaviour (slow washout), due to the fact that the relative underestimation was more severe, particularly at the point of maximum activity. This discrepancy is consistent with the results of the 2D phantom experiments of Chapter 3, where it was found that TACs corresponding to faster tracer kinetics tended to be underestimated more severely than those corresponding to slower kinetics.

After taking these facts into account, it is clear that each of the four acquisition protocols considered in this experiment reconstructed the TAC in one kidney more accurately than in the other. Specifically, acquisitions I and III both consistently gave less accurate results for the right kidney than for the left kidney, while the opposite was true of acquisitions II and IV. The accuracy of the TAC corresponding to either kidney is directly affected by whether the amount of attenuating material between that kidney and the camera increased or decreased during certain periods of the acquisition. For instance, although acquisition III started with one head on the phantom's right side and the other behind the phantom (i.e., with little attenuating material between the camera and the right kidney, initially), the heads rotated away from the right kidney and towards the left kidney during the first four minutes of the acquisition. As a result, the TAC in the left kidney was reconstructed more accurately, since the right kidney TAC was underestimated during the first four minutes.

As indicated by the "Max Δ" results in Table 5.4, which show the greatest difference in ε values for each simulation over the four acquisitions, the accuracy of the reconstructed TAC varied considerably depending on the acquisition. For instance, for the reconstruction of phantom C using d^{2}EM, the error in the left kidney TAC in the image corresponding to acquisition IV was 80% larger than in the image corresponding to acquisition I. Of the four acquisition protocols that were considered, it is apparent from the results tabulated in the right half of Table 5.4 that the bias introduced by acquisitions II and III was less severe

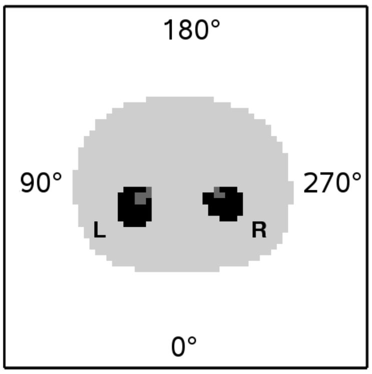

Acquisition		I		II		III		IV	
Initial pos.		135° + 45°		90° + 0°		270° + 0°		225° +315°	
Rotation		360° ccw		360° ccw		360° cw		360° cw	
		LK	RK	LK	RK	LK	RK	LK	RK
A	dEM	16.0	22.1	20.5	15.6	16.4	23.7	22.4	15.9
	d^2EM	12.3	16.6	15.6	11.7	12.4	17.8	16.3	12.7
B	dEM	12.9	16.4	15.7	16.4	16.9	19.5	16.8	13.8
	d^2EM	11.2	19.9	12.2	16.7	15.5	14.1	20.0	12.0
C	dEM	12.9	23.0	15.9	17.1	16.6	24.5	16.4	16.8
	d^2EM	11.0	15.6	12.1	12.1	15.4	17.4	20.3	13.5
D	dEM	15.9	16.4	21.5	16.8	15.7	19.8	22.6	14.0
	d^2EM	12.2	19.6	16.2	16.7	12.3	13.8	15.8	11.7

Table 5.3: Relative error in mean TAC values, ε, for different acquisitions. The angular conventions used to indicate initial position of heads are shown in top figure, along with a transaxial slice through the phantom showing the kidneys, ureters, and background region. “cw” and “ccw” in the column headings refer to clockwise and counterclockwise rotations; “LK” and “RK” to the errors for the left and right kidneys, respectively.

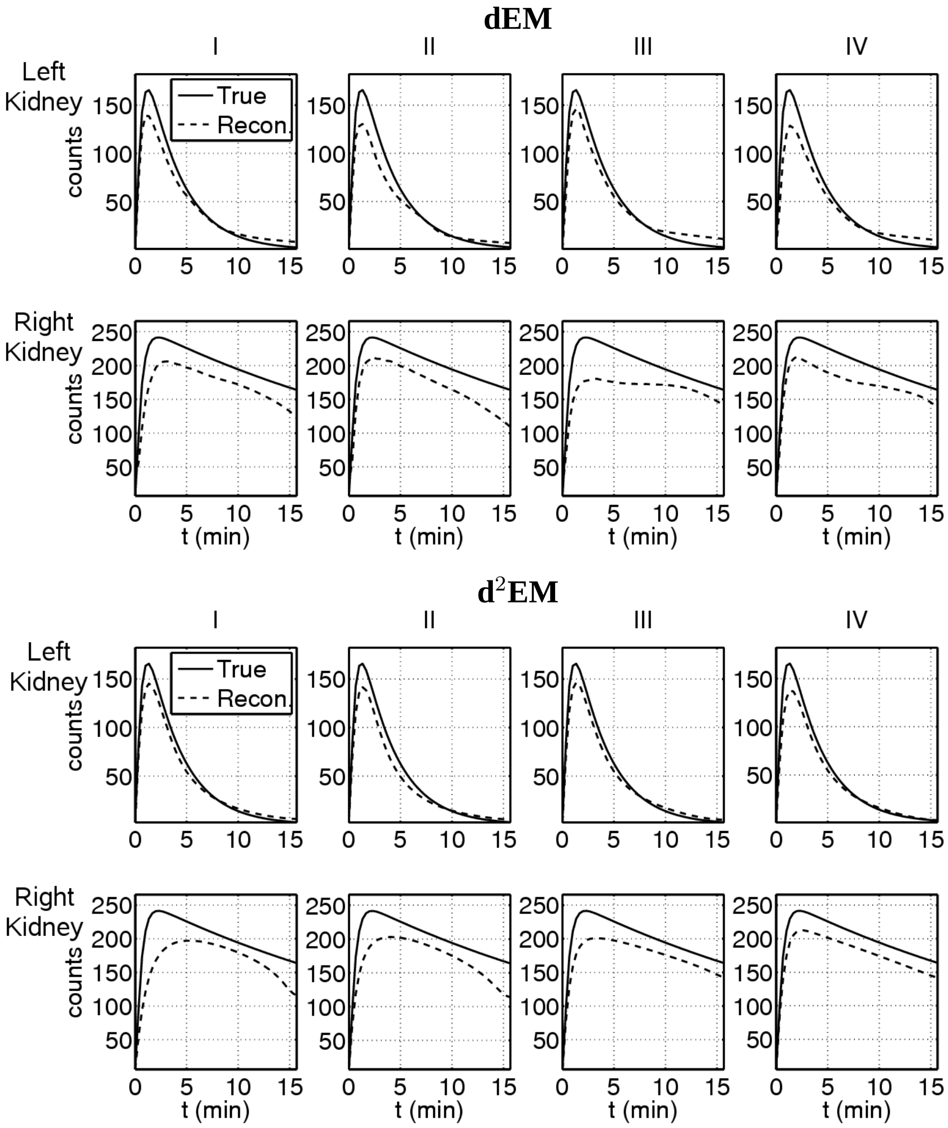

Figure 5.3: Mean TACs (dashed lines) extracted from reconstructed images of Phantom D, using dEM (top figure) and d^{2}EM (bottom figure). True TAC shown as a solid line in each plot. Columns correspond to acquisition protocols used to acquire the data.

Simulation		Avg. value LK	Avg. value RK	Max Δ LK	Max Δ RK	Acquisition		Avg. value LK	Avg. value RK
A	dEM	18.8	19.3	6.4	8.2	I	dEM	14.4	19.5
	d^{2}EM	14.2	14.7	4.0	6.1		d^{2}EM	11.7	17.9
B	dEM	15.6	16.5	3.9	5.7	II	dEM	18.4	16.5
	d^{2}EM	14.7	15.6	8.8	8.0		d^{2}EM	14.0	14.3
C	dEM	15.4	20.4	3.7	7.7	III	dEM	16.4	21.9
	d^{2}EM	14.7	14.7	9.2	5.3		d^{2}EM	13.9	15.8
D	dEM	18.9	16.7	7.0	5.9	IV	dEM	19.6	15.1
	d^{2}EM	14.2	15.5	4.0	7.9		d^{2}EM	18.1	12.5

Table 5.4: Summary of the results presented in Table 5.3. Avg. value refers to the average ε value over the four acquisitions for each simulation (in the left half of the table) or to the average ε value over the four simulations for each acquisition (in the right half of the table). Max Δ is the greatest difference in ε values over the four acquisitions for each simulation. "LK" and "RK" refer to errors in the left and right kidneys, respectively.

than that introduced by acquisitions I and IV.

The results also indicate that overall, d^{2}EM provided more accurate TACs than dEM, in terms of the error ε. In some cases where unhealthy behaviour was present in the kidney on the far side of the initial position of the camera (e.g. the left kidney of Phantom B, using acquisition IV), d^{2}EM did perform more poorly than dEM. For acquisitions II and III, however, ε values from images reconstructed using d^{2}EM were always smaller or roughly the same size as those obtained from the images reconstructed using dEM. Thus, the errors caused by attenuation in images reconstructed using d^{2}EM was generally less severe than in images reconstructed using dEM, provided that a sensible acquisition protocol was used.

Finally, it is apparent from Figure 5.3 that the TACs in both kidneys are noticeably underestimated, regardless of which acquisition protocol was used. In addition to the effects of attenuation, there appears to be some amount of spill-out from both kidney ROIs into the surrounding background. In Figure 5.4, we show the total counts reconstructed inside the left and right kidney ROIs for the simulation using Phantom B and acquisition II, with and without attenuation present. While TACs within the true boundaries of the left and right

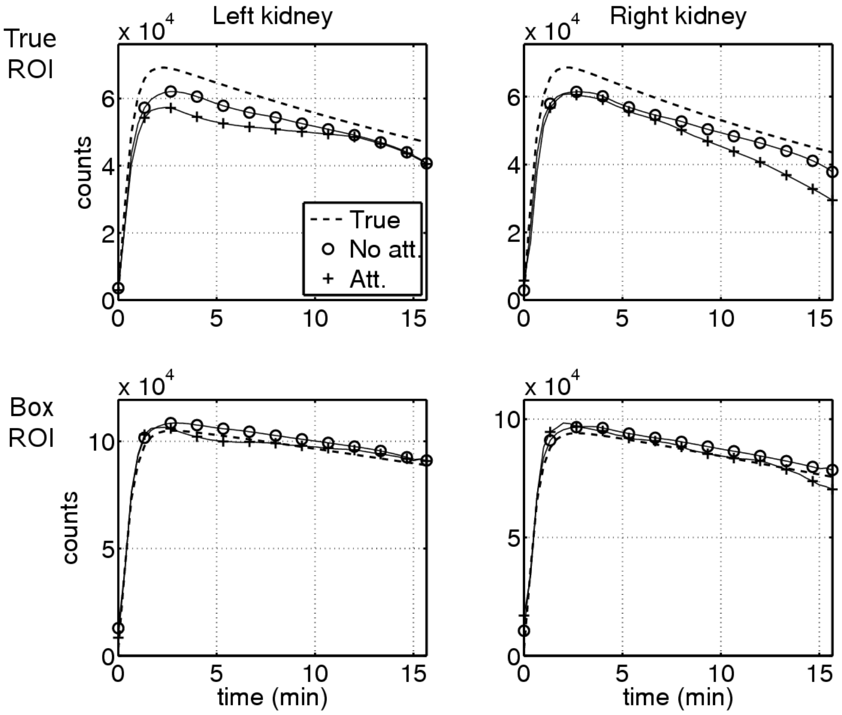

Figure 5.4: Summed TACs extracted from images of Phantom B, acquisition II, reconstructed using 60 iterations of dEM. TACs corresponding to the simulation without attenuation (circular marker) and with attenuation (square marker) are shown, along with the true TAC (dashed line). The summed TACs for the left and right kidneys were computed using the true organ boundaries (top row) as well as rectangular box-shaped ROIs that encompassed each kidney and some surrounding background (bottom row).

kidneys (top row) for the simulation without attenuation were closer to the truth than when attenuation was included, they were still underestimated by roughly 10%. When the counts were summed over a larger, rectangular ROI that included each kidney as well as some of the surrounding background (bottom row), the true TAC and the TACs reconstructed with and without attenuation were all in good agreement with one another. Thus, it is apparent that activity from the kidneys has spilled out into the surrounding region in both cases. This spill-out effect was not prevalent in the 2D experiments of Chapter 3, and so it may be related to the more complicated 3D geometry of this simulation, or to the fact that a different method (APDI) was used to generate the projection data.

5.1.3 Experiment 2: Application of template corrections

In the preceding experiment, all four of the simulated acquisition protocols resulted in a more accurate reconstruction of one kidney over the other, due to effects of attenuation on the reconstructed image. While it may be possible to find an acquisition protocol that reduces this bias, it is impossible to ensure that the effects of attenuation on both kidneys will be the same. Thus, these artifacts will always be present to some extent. In this experiment, we investigate whether the CF and IE methods proposed in Chapter 4 can successfully reduce these artifacts. We consider only the images reconstructed using acquisition II from the previous section. This protocol was found to have a bias towards the right kidney, due to the fact that it rotates away from the left kidney initially, increasing the amount of attenuating tissue between that kidney and the detectors.

The CF and IE corrections were applied to reconstructed images corresponding to the six simulations A–F described in Table 5.2. A third correction, denoted CF-IE, was also applied to each reconstructed image. In this approach, the image x'_C resulting from the application of the CF correction (see Figure 4.6) was used in place of the original reconstructed image x' to create the template used in the IE correction (Figure 4.7); that is, the two correction approaches were applied serially. It was expected that this correction would combine the benefits of both the CF and IE approaches; namely, explicit modeling of artifacts introduced during reconstruction, through the CF method, and a subsequent fit to the projection data using the IE method. In these experiments, the second run of the reconstruction algorithm used in the IE and CF-IE approaches consisted only of 40 iterations, as further iterations did not appreciably improve the accuracy of the corrected image.

Since both the CF and IE methods require a segmentation of the image, the accuracy of this segmentation has an impact on their effectiveness. We investigated two segmentation methods: the true segmentation based on the known region boundaries from the phantom, and a computed, probabilistic segmentation based only on the reconstructed dynamic image. The probabilistic segmentation was created by loading each reconstructed image into a user-assisted dynamic segmentation program [62]. Using this program, the user placed "seeds" in voxels of the reconstructed image to identify segments corresponding to different organs. The program then generated a probabilistic field using a random walk approach, which took into account both the proximity of each voxel to the seeds, as well as the similarity between TACs in each voxel within a segment. Each voxel was thus assigned a probability of belonging to each of the segments, and was made part of the segment corresponding to the highest probability.

After this semi-automatic process, the user was able to view the segmented volume and make corrections if required. For instance, if a voxel that was clearly part of the right kidney was mistakenly assigned to the left kidney, it could be reassigned to the right kidney. This procedure only allowed for the correction of obvious errors, however. Thus, the probabilistic method allowed us to assess the impact of using an imperfect segmentation when applying the CF and IE correction methods. An example of one of the segmented volumes generated using this method is shown in Figure 5.5. Although the segmented volume shown in this figure is fairly similar to the true segmentation, it does contain errors, particularly in the right kidney. The probabilistic method provided a fast, repeatable method of segmentation that did not require drawing ROIs by hand, or knowing the truth.

For both segmentation methods, the image was segmented into regions corresponding to background, the left and right kidneys, left and right pelves (including ureters) and the bladder. Simulations E and F included unhealthy behaviour in only a small part of one kidney, in order to see if the proposed correction methods could be successfully applied to small adjacent regions with different dynamic behaviour. For these simulations, two situations were tested. In the first, the small unhealthy regions were segmented separately from the healthy portion of the kidney; in the second situation, the entire kidney was considered as a single segment. This second situation modeled the case where the segmentation was created based purely on anatomy, without recognizing that the unhealthy region had

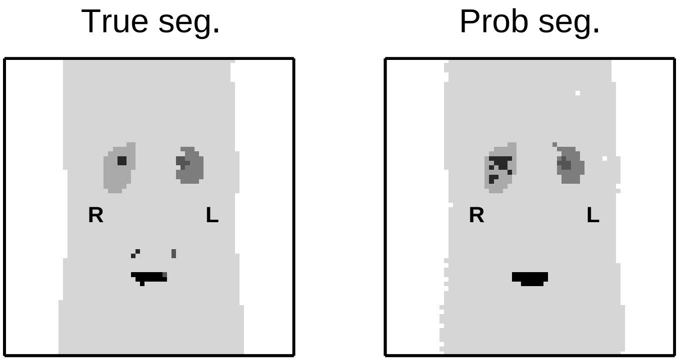

Figure 5.5: Example segmentations used for CF and IE corrections. Left figure shows coronal slice through the segmented volume based on true organ boundaries, right figure the same slice through the volume generated from the probabilistic segmentation of the dEM reconstruction of Phantom A. Different shades of grey indicate the segment to which each voxel belonged.

different dynamic behaviour. It was expected that the effectiveness of the correction methods would suffer as a result. This incorrect segmentation was only tested using the true organ boundaries; since the small regions had clearly different dynamic behaviour than the rest of the kidneys, it was apparent when performing the probabilistic segmentation that they should be segmented separately. After applying the three different correction approaches, the error measures ε, $\bar{\sigma}$ and $\mathcal{S}$ (as described in Chapter 3, Equations (3.3), (3.4) and (3.5), respectively) were computed within the dynamic regions of interest. The true organ boundaries were used for these calculations, regardless of whether the true or probabilistic segmentation was used during the correction.

Since a large number of simulations were run, only summary statistics for the simulations involving phantoms A–D are provided in Table 5.5. The full results of these experiments are tabulated in Tables A.4 to A.9 in Appendix A. All three correction approaches resulted in a substantial improvement to ε, both when the exact boundaries and the probabilistic segmentation were used to generate the template. As expected, the correction was more effective when the true organ boundaries were used. The improvement to ε was generally comparable regardless of whether the CF, IE, or CF-IE approach was used. Figure 5.6 shows the mean TACs in the left and right kidneys before and after the application

True boundaries

		Uncorrected		CF method		IE method		CF-IE method	
		LK	RK	LK	RK	LK	RK	LK	RK
ε	dEM	18.4	16.5	3.2	4.2	3.3	4.4	**2.6**	**3.7**
	d^{2}EM	14.0	14.3	3.0	**3.7**	**2.6**	4.8	3.0	3.8
$\bar{\sigma}$	dEM	31.9	32.4	21.0	20.0	12.8	13.3	**10.8**	**11.0**
	d^{2}EM	28.4	28.2	18.6	17.4	12.3	11.7	**9.7**	**9.2**
$\mathcal{S}$	dEM	16.9	18.6	12.4	13.8	6.6	8.5	**6.5**	**7.0**
	d^{2}EM	11.5	12.6	8.7	8.9	6.1	6.6	**4.5**	**4.4**

Probabilistic segmentation

		Uncorrected		CF method		IE method		CF-IE method	
		LK	RK	LK	RK	LK	RK	LK	RK
ε	dEM	18.4	16.5	**3.9**	**4.7**	4.5	5.1	4.2	5.4
	d^{2}EM	14.0	14.3	4.1	4.9	**3.4**	**4.7**	4.0	5.9
$\bar{\sigma}$	dEM	**31.9**	32.4	37.7	27.5	33.7	23.7	34.1	**21.5**
	d^{2}EM	28.4	28.2	28.7	26.2	25.5	22.3	**25.5**	**21.0**
$\mathcal{S}$	dEM	16.9	18.6	17.1	15.7	**12.8**	11.6	13.7	**10.6**
	d^{2}EM	11.5	12.6	10.9	10.3	9.2	**8.2**	**8.1**	9.0

Table 5.5: Average error values ε, $\bar{\sigma}$ and $\mathcal{S}$ before and after application of template-based corrections, for experiments involving Phantoms A–D. Values shown are the average error in each kidney over the four simulations. The smallest error for either kidney is bolded in every row.

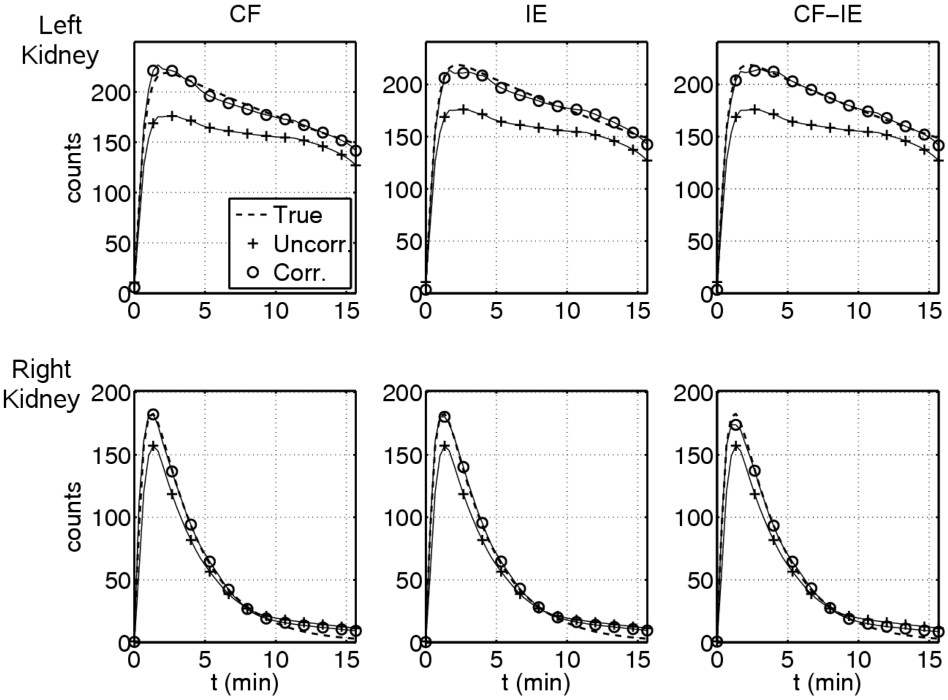

Figure 5.6: Mean TACs extracted from the left and right kidney ROIS of the dEM reconstruction of Phantom C, before and after application of each correction method. Dashed line in each plot represents true TAC, circular markers the uncorrected TAC, and cross markers the corrected TAC. Columns correspond to the three correction methods. Segmentation based on the true organ boundaries was used

of the three correction methods (using the true segmentation), for the dEM reconstruction of Phantom C. Again, this figure is a representative sample of the many simulations that were run. From this figure, it is clear that all three correction methods have compensated for the spill-out effect noted in the last section, as well as the effect of attenuation on the TACs. For instance, the TAC in the left kidney of the uncorrected image was more severely underestimated during the first eight minutes than during the last eight minutes, since the amount of attenuating material between the detector and the left kidney increased during this period; in the corrected images, this discrepancy has been eliminated.

It is somewhat surprising that all three correction methods have a comparable effect on the mean TAC in each region. Although both the CF and IE methods use the same template as part of the correction, the mechanism that they employ to produce the final corrected image is quite different. It is particularly interesting that the corrected TACs resulting from the application of the IE method appear to be free of any errors caused by attenuation, since unlike the CF approach, this method does not explicitly attempt to correct for these errors at any point. It appears that when the reconstruction algorithm is started from a generic, uniform initial estimate, it converges to a local minimum (the image which suffers from attenuation artifacts); when it is started from a better initial estimate (the template), it avoids this local minimum and converges to a more accurate minimizer (the image which is largely free of these errors).

When the true organ boundaries were used to create the template, $\bar{\sigma}$ and $\mathcal{S}$ were also improved by the application of the corrections. It is apparent from the top set of plots in Figure 5.7, which shows some of the reconstructed TACs at the voxel level in the corrected and uncorrected images, that the TACs are more tightly clustered around the true TAC after application of the correction methods. The IE and CF-IE methods provided a greater reduction in these error measures than the CF method. This result is not surprising, since the CF method simply applied a correction factor to each voxel of the uncorrected image, while the IE and CF-IE methods restarted the reconstruction algorithm from an initial estimate that was spatially uniform within each ROI (the template). Thus, provided that this initial estimate was reasonably accurate, these TACs remained fairly consistent during the second run of the reconstruction algorithm. As was the case in the phantom experiments of Chapter 3, the images reconstructed using d^{2}EM tended to have smaller values of $\bar{\sigma}$ and $\mathcal{S}$ than those reconstructed using dEM.

When the probabilistic segmentation was used by the correction methods, improvements to $\bar{\sigma}$ and $\mathcal{S}$ were not as large; in some cases, the application of the template corrections actually increased the value of $\bar{\sigma}$. (See Table A.7). This increase in $\bar{\sigma}$ can be attributed to the errors present in the segmentation. For instance, in the third row of Figure 5.7, two of the twelve TACs that are shown for the left kidney have very low activity after the application of the corrections. These TACs correspond to voxels of the left kidney that were incorrectly assigned to the background region by the probabilistic segmentation algorithm, meaning that they were adjusted as if they were part of this region. These errors persisted even when the IE and CF-IE methods were applied, despite the fact that these methods attempted to correct for errors of this nature by fitting the template to the data in the second

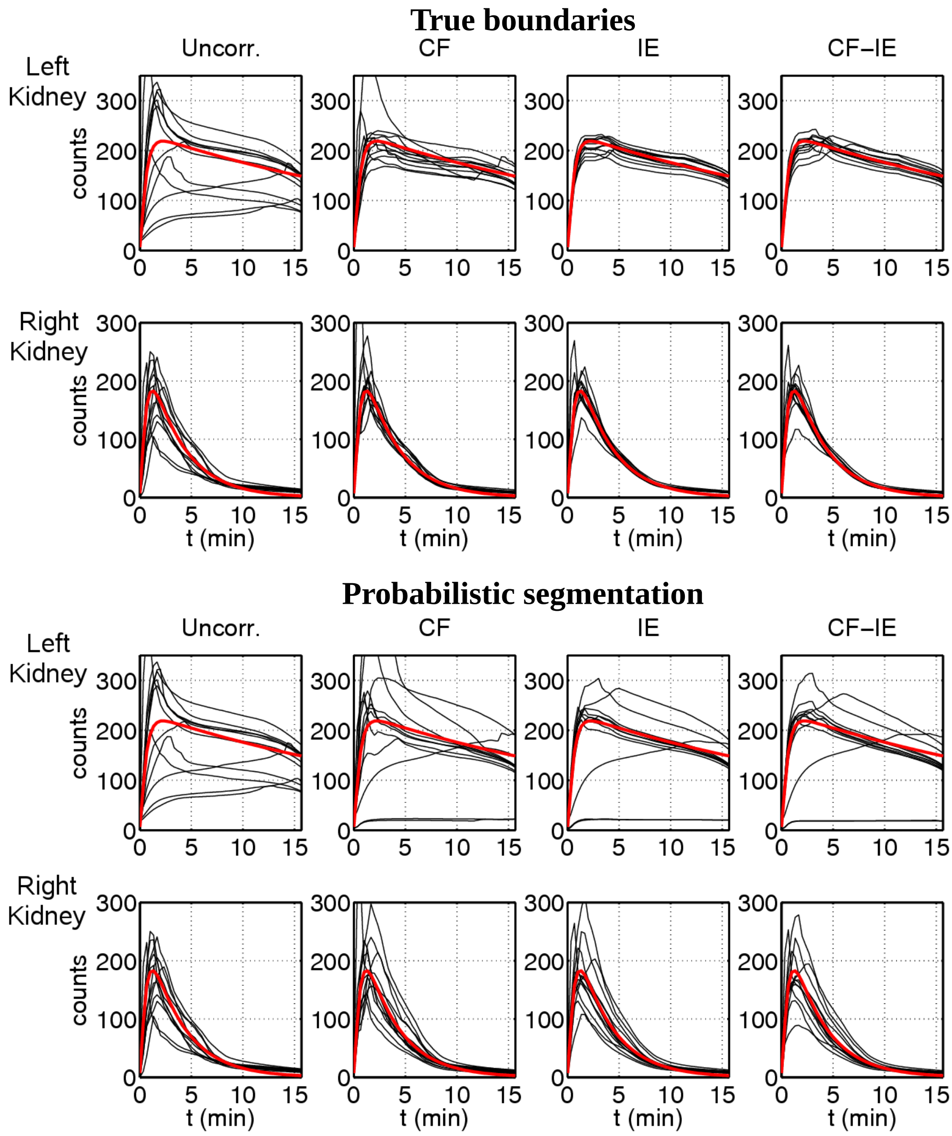

Figure 5.7: Voxel-level TACs within the left and right kidney ROIs of the dEM reconstruction of Phantom C, before and after application of each correction method. True TAC is shown in red, with 12 randomly-selected voxel level TACs shown as solid black lines. Columns correspond to the uncorrected image and each of the three corrected images. Top plot shows the application of corrections using template based on true organ boundaries, while the bottom plot shows the same corrections applied using the probabilistic segmentation.

run of the reconstruction algorithm.

The results for phantom experiments E and F, which included unhealthy behaviour in only a portion of either kidney, are tabulated in Tables A.10 to A.12 in Appendix A. When the "correct" segmentation was used (true boundaries, with the unhealthy portion segmented separately), the results were similar to those obtained for the experiments with Phantoms A-D; specifically, ε was improved considerably by all three methods, while the IE and CF-IE methods were the most successful in reducing $\bar{\sigma}$ and $\mathcal{S}$. When the "incorrect" segmentation was used, in which the partially unhealthy kidney was considered as a single segment, the resulting template was inaccurate since the regions corresponding to the partially unhealthy kidney were assigned a TAC that was a combination of the healthy and unhealthy behaviours. As a result, the two regions of the partially unhealthy kidney were not adjusted based on an accurate approximation to their true dynamic activity, resulting in much larger errors than when the correct segmentation was used.

Results using the probabilistic segmentation were also poorer than when the true segmentation was used, and in many cases, worse than when the "incorrect" segmentation was applied as well. The diminished effectiveness of the correction methods in this case can be attributed to problems in segmenting the partially unhealthy kidney, which featured three relatively small dynamic regions (the healthy portion, the unhealthy portion, and the pelvis/ureter) in close proximity to one another. The probabilistic segmentation method had difficulty distinguishing between these three regions, due to their close proximity and small size, which resulted in errors in the segmented volume. Even when the incorrect or probabilistic segmentation were used, however, the error measures were still smaller in the corrected images than in the uncorrected images in nearly every case, aside from a few cases where $\bar{\sigma}$ was increased.

Overall, this experiment has indicated that all three correction methods substantially reduce errors in the mean TAC in each kidney, even if the segmentation used in the creation of the template is imperfect. Errors in the segmentation do reduce the extent of the improvement to the mean TAC, however. Consistency of TACs inside each ROI may also be improved by the application of these methods, but any improvement is more heavily dependent on the accuracy of the segmentation. If the segmentation contains errors, the overall consistency of TACs may not be improved, and could even be worsened with respect to the uncorrected image. Provided that the segmentation was accurate, however, the CF-IE method typically provided the greatest improvement of the three methods.

5.2 Renal volunteer experiment

5.2.1 Methodology

In this section, we apply the techniques discussed so far to dynamic renal images produced of two consenting healthy adult volunteers. A 370 MBq (10 mCi) injection of ^{99m}Tc-DTPA was used in both studies. The data were acquired using a dual-head Siemens Symbia T2 SPECT/CT system with detectors positioned at 90°, and attenuation correction data provided by the 2 slice CT scanner. The camera heads started behind the volunteer and on their left side, and completed a 360° rotation consisting of 64 stops of 20 seconds each. Images consisting of 128×128-voxel slices and sixty-four 20 second time frames were reconstructed using 60 iterations of dEM and 80 iterations of d^{2}EM. Voxels were 4.79 mm per side, and the effects of attenuation and collimator blurring were incorporated into the system matrix. A planar renogram of both volunteers, taken two days prior to the SPECT scan, indicated that both had healthy renal function.

The three correction methods studied in the previous section were applied to the reconstructed images. For this experiment, the segmented volumes used by the correction methods were generated by hand. Specifically, the CT map that was acquired during the SPECT scan was examined slice-by-slice to identify the left and right kidneys, while the renal pelvis in each kidney was identified by looking at slices of the reconstructed image that had been summed over time. The pelves were clearly visible in this summed image since they had much higher intensity than the cortex. This segmentation process is illustrated in Figure 5.8.

5.2.2 Effect on mean TAC

We first examine the effect of these corrections on the mean TAC for each kidney. Based on the results of the phantom experiments in the previous section, the uncorrected TACs reconstructed in both kidneys are probably underestimated relative to the true TAC, as a result of spill-out effects. Furthermore, since the acquisition used here was the same as acquisi-

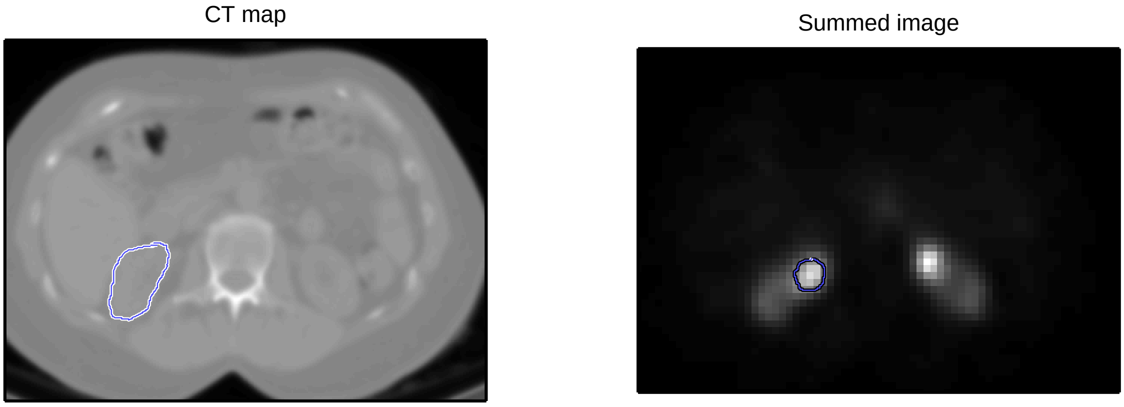

Figure 5.8: Illustration of process used to generate segmentations for the two sets of renal data. Left: Transaxial slices of the CT map were viewed, and regions of interest were drawn around the right and left kidneys. Right: The corresponding slice of the image reconstructed using dEM, summed over all time frames, was viewed and ROIs were drawn around the right and left pelves.

tion II in the phantom experiments, the left kidney should be underestimated by a greater margin than the right kidney due to attenuation effects, as the camera rotated away from the left kidney during the early phase of the acquisition. To assess the effectiveness of the correction methods on reducing these effects, we compared the peak values of the TACs in the left and right kidneys before and after the application of each correction method. Since there was not a known, true TAC against which to compare the reconstructed TACs, we simply measured the relative increase in the left and right kidney peak activities after applying each correction (denoted LK+ and RK+, respectively), as well as the relative difference between the peak activity in the left and right kidneys (denoted Δ_{RL}). Specifically:

$$\begin{aligned} \text{LK+} &= \left(\tau^{\text{max}}_{\text{LK, corr}} - \tau^{\text{max}}_{\text{LK, uncorr}}\right) \Big/ \tau^{\text{max}}_{\text{LK, uncorr}} \times 100\%, \\ \text{RK+} &= \left(\tau^{\text{max}}_{\text{RK, corr}} - \tau^{\text{max}}_{\text{RK, uncorr}}\right) \Big/ \tau^{\text{max}}_{\text{RK, uncorr}} \times 100\%, \\ \Delta_{RL} &= \left(\tau^{\text{max}}_{\text{RK}} - \tau^{\text{max}}_{\text{LK}}\right) \Big/ \tau^{\text{max}}_{\text{LK}} \times 100\%, \end{aligned} \tag{5.2}$$

where $\tau^{\max}_{\text{LK, corr}}$ refers to the peak activity in the left kidney of the corrected image, and correspondingly for the other quantities. Results are tabulated in Table 5.6, and an example of the mean TACs before and after application of the correction methods is shown in Figure 5.9.

The results in Table 5.6 show that all three correction methods have similar effects on the mean TACs in this case as they did in the phantom experiments. The TACs in both the left and right kidneys have been scaled upwards by a factor of 20 to 45%. Looking back at the phantom experiments of the previous section, the analogous relative increases RK+ and LK+ (which were not tabulated in that section, but can be easily calculated) were generally lower than the values observed here, typically on the order of 15 to 25%. As such, the corrected TACs here may have been overestimated slightly, although it is not possible to know for certain. The value of LK+ was greater than RK+ in every case, indicating that the left kidney was almost certainly underestimated more severely than the right kidney, as was predicted by the phantom experiments. As a result of the corrections, the discrepancy between the left and right kidneys, Δ_{RL}, was reduced by the correction approaches in every case but one. The extent of this reduction varied depending on the reconstruction algorithm used and the correction that was applied.

5.2.3 Effect on consistency of TACs

In the absence of the known truth against which to compare the reconstructed images, it was also not possible to use the same measures of TAC consistency, $\bar{\sigma}$ and $\mathcal{S}$, as were used in the phantom experiments. Furthermore, in reality the kidney itself is comprised of numerous individual lobes, which may contain different concentrations of activity or exhibit slightly different regional dynamic behaviour. Thus, assuming uniform dynamic behavior in the entire kidney when calculating $\bar{\sigma}$ or $\mathcal{S}$ could be a misleading measure of image accuracy.

So, in order to assess the consistency of TACs in the reconstructed images, small cubes consisting of several voxels were first defined in the inferior and superior regions of each kidney, yielding four ROIs in total, as illustrated in Figure 5.10. In the first volunteer, each cube was 4×4×4 voxels in size (corresponding to a volume of approximately 7 cc). Since the second volunteer had smaller kidneys, smaller cubes of 3×3×3 voxels were used. Due to the small size of each ROI, the true behavior within them was expected to be

		Uncorr.	CF			IE			CF-IE		
		Δ_{RL}	LK+	RK+	Δ_{RL}	LK+	RK+	Δ_{RL}	LK+	RK+	Δ_{RL}
Volunteer #1	dEM	12.1	27.0	22.3	7.9	30.0	27.3	9.8	34.1	31.0	9.5
	d^{2}EM	14.7	24.9	20.8	10.9	27.0	25.3	13.1	29.1	25.7	11.7
Volunteer #2	dEM	11.4	30.3	28.9	10.1	39.2	28.8	3.1	43.2	33.9	4.1
	d^{2}EM	4.2	27.1	27.7	4.7	38.8	36.8	2.7	42.9	40.6	2.5

Table 5.6: Effect on the mean TACs of each of the three correction methods, for the two sets of volunteer data. Formulas for LK+, RK+ and Δ_{RL} are given in Equation (5.2).

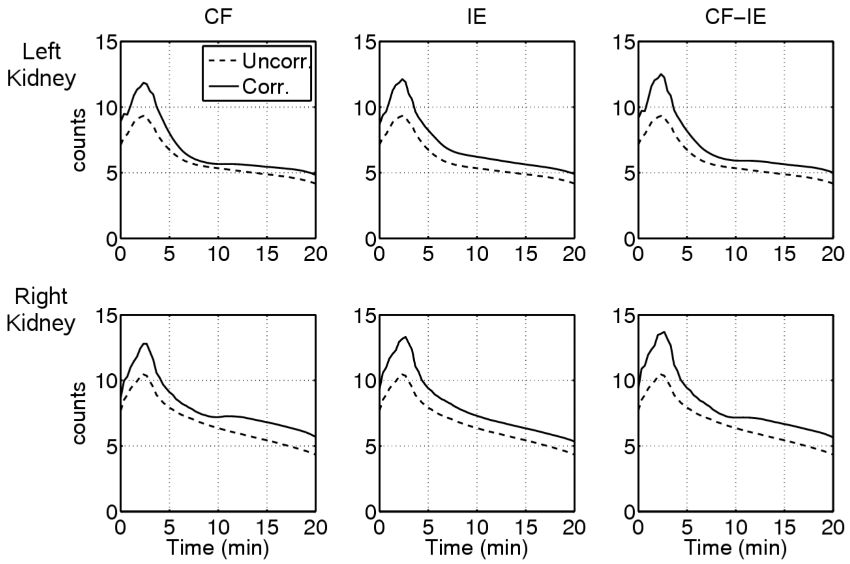

dEM image

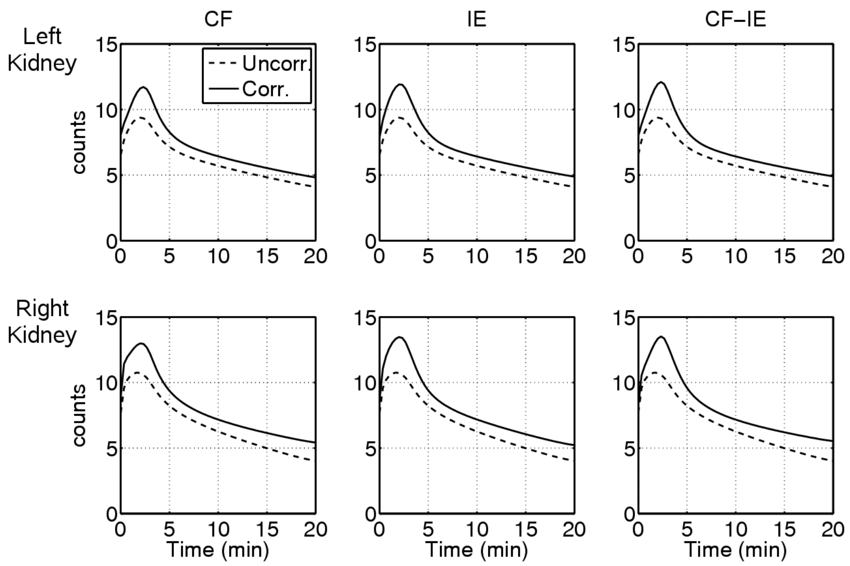

d^{2}EM image

Figure 5.9: Mean TACs extracted from left and right kidney regions of reconstructed images of Volunteer #1, before and after application of correction methods. Top plots are of the dEM reconstruction, bottom plots of the d^{2}EM reconstruction. Dashed line shows the mean TAC extracted from uncorrected image, while solid line shows the mean TAC after the application of the CF, IE, and CF-IE corrections.

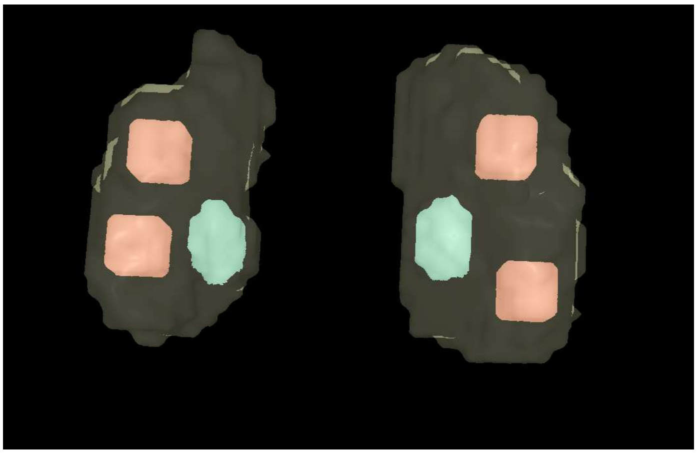

Figure 5.10: Volume rendering of the regions of interest used to assess consistency of TACs within the reconstructed images. Image is of the ROIs used for the first volunteer (posterior view). Faint outline shows left and right kidneys, with pelves shown in blue and ROIs shown as red cubes. Light patches around edges appear due to the volume rendering. *Figure prepared with the assistance of A. Saad. [62]*

fairly consistent. Values of $\bar{\sigma}$ and $\mathcal{S}$ inside each of the ROIs were then calculated using a modified formula. Since the true TAC was not known, the mean TAC for each region was used as a surrogate in the error formulas (3.4) and (3.5). We denote these modified error measures by $\bar{\sigma}^*$ and $\mathcal{S}^*$, respectively, to distinguish them from the ones used in the phantom experiments. This modification changes the nature of these error measures to some extent; in the phantom experiment, $\bar{\sigma}$ and $\mathcal{S}$ measured the consistency of the TAC in every voxel with the true TAC, while here, $\bar{\sigma}^*$ and $\mathcal{S}^*$ simply measure consistency with the mean TAC, regardless of how accurate that mean TAC is.

Full results of these experiments are presented in Tables A.13 and A.14, and summarized in Table 5.7. The results presented in Table A.13 indicate that the effect of the correction methods on $\bar{\sigma}^*$ is unpredictable. In half of the cases, applying any of the three methods caused $\bar{\sigma}^*$ to increase, while in the other half, at least one of the three methods reduced $\bar{\sigma}^*$. It is surprising that the application of IE and CF-IE methods could result in a larger $\bar{\sigma}^*$ value, since these methods initialized the second run of the reconstruction using the template, which one would expect would result in less variance between TACs. Figure 5.11 shows a sampling of the voxel-level TACs within the four small regions of the

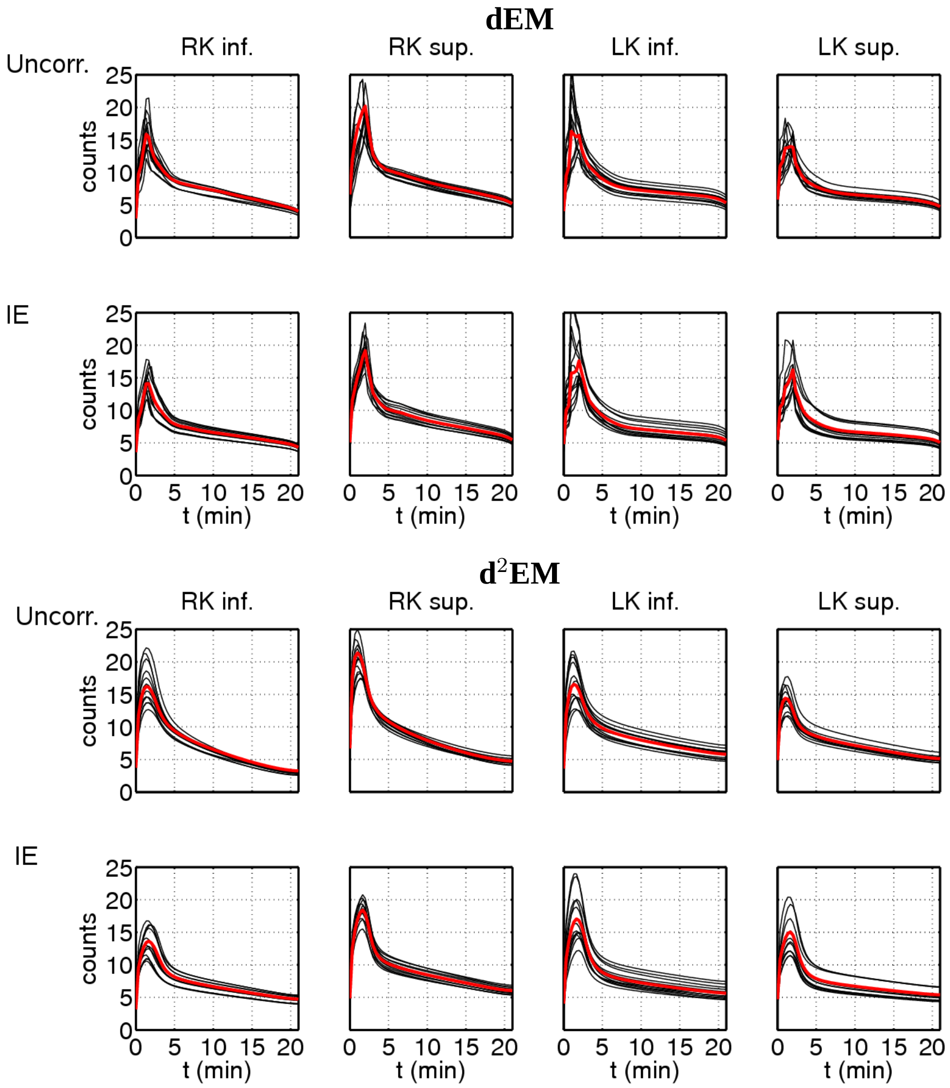

Figure 5.11: Voxel-level TACs within the four ROIs defined in the kidney regions of images of Volunteer #2, before and after application of the IE correction method. Top plot shows results for image reconstructed using dEM, bottom plot for image reconstructed using d^{2}EM. True TAC is shown in red, with 12 randomly-selected voxel level TACs shown as solid black lines. Columns correspond to the each of the four regions.

		Volunteer #1				Volunteer #2			
		Uncorr.	CF	IE	CF-IE	Uncorr.	CF	IE	CF-IE
$\bar{\sigma}^*$	dEM	**14.0**	15.1	14.6	14.6	**12.0**	16.1	13.7	14.9
	d^{2}EM	15.6	17.3	**14.4**	14.6	**12.3**	15.8	13.8	15.0
$\mathcal{S}^*$	dEM	7.0	6.3	**5.8**	**5.8**	8.0	7.9	**6.1**	6.5
	d^{2}EM	6.0	7.0	**4.3**	**4.3**	6.1	6.1	**4.1**	4.2

Table 5.7: Average values of $\bar{\sigma}^*$ and $\mathcal{S}^*$ before and after application of the template-based corrections. Averages were taken over the four ROIs defined in the kidneys. The smallest error value in each row is bolded.

reconstructed image corresponding to Volunteer #2, before and after application of the IE method. In this case, $\bar{\sigma}$ was reduced in the two ROIs of the right kidney after application of the IE method, but increased in the two ROIs of the left kidney. It is apparent from these images that there is more variation among the TACs within these two left kidney regions after the IE correction was applied, but it is difficult to ascertain why this is the case. It may in fact be that the behaviour within even these small ROIs was not homogenous in reality.

Conversely, the relative shape error $\mathcal{S}^*$ was consistently reduced by the application of the IE and CF-IE methods. So, although the use of the template as an initial estimate did not prevent the TACs within each ROI from diverging in magnitude, it did generally result in more consistent shapes within each ROI. The use of d^{2}EM over dEM also consistently resulted in lower values of $\mathcal{S}^*$, both before and after application of the correction methods. This improvement is apparent in Figure 5.11, particularly in the inferior left kidney region. In the images reconstructed using dEM, the mean TAC for the region peaks twice as a result of inconsistencies at the voxel level. In the images reconstructed using d^{2}EM, the mean TAC corresponding to this region is smoother and appears to be much more physiologically realistic.

Chapter 6

Conclusions and future work

6.1 Conclusions

In this thesis, we have investigated the reconstruction of dynamic SPECT images from data acquired using a single slow camera rotation. The investigation has focused on two main areas: the use of a temporal concavity constraint (the d^{2}EM method) to promote smoothness and consistency of time activity curves within regions of interest, and a discussion of artifacts – particularly those due to effects of attenuation – that occur in dynamic images reconstructed from slow-rotation data, as well as methods to potentially correct for them.

The phantom experiments of Chapter 3 have demonstrated that, compared to dEM, d^{2}EM provides TACs with smoother, more consistent shapes in dynamic regions of interest. In these experiments, images reconstructed using d^{2}EM were more accurate than the corresponding images reconstructed using dEM, as indicated by significant improvements in all three measures of error that were computed. The improvements provided by d^{2}EM were especially noticeable in phantom simulations with high levels of noise and relatively gradual tracer kinetics. The stronger constraint used by d^{2}EM meant that the algorithm was more resistant to the effects of noise, such as spurious “spikes” in activity occurring in a single time frame.

The experiments using renal data indicated that d^{2}EM can be successfully applied to a real-life clinical application, and that it provides some improvements over dEM in this situation as well. TAC shapes were again found to be more consistent within small ROIs of the kidneys, and the mean TACs for those regions were smoother and more physiologically realistic as a result. The fact that TAC shapes at voxel level were more consistent with the mean TAC in the d^{2}EM images is important, because it provides more confidence that averaging the TAC over that ROI accurately represents the kinetics in that region. If TAC shapes vary drastically within a region, it is not clear whether the mean TAC is physically meaningful.

In the second part of the thesis, we identified several types of artifact that occur in dynamic images reconstructed from slow-rotation data. Artifacts caused by the effects of attenuation were shown to be particularly severe, resulting in the underestimation of regional TACs during time periods corresponding to those when the amount of attenuating material between that region and the camera increased during the acquisition of projection data. These effects occur as a result of the relatively small amount of projection data used in single slow-rotation dynamic SPECT imaging. Inclusion of attenuation modeling in the system matrix used to reconstruct the image does not account for these effects, and the artifacts that result persist even after many iterations of the reconstruction algorithm. In 3D phantom simulations of a dynamic renal SPECT study, it was shown that as a result of these effects, the accuracy of the reconstructed TAC corresponding to either kidney varied depending on the protocol used to acquire the data.

Three different methods to correct for these effects were investigated, all of which made use of a numerical template to approximate the true dynamic distribution of activity. In phantom experiments, all three of these methods were found to substantially increase the accuracy of the mean TAC corresponding to each kidney, and provided correction for the differing effects of attenuation on either kidney. The effect of the correction methods on the consistency of TACs within each ROI was unpredictable, however, as the use of these methods was found in some cases to increase the variation among TACs within ROIs. Of the three correction methods that were investigated, the two that used a template as the initial estimate to a second run of the reconstruction algorithm (the IE and CF-IE methods) generally resulted in better uniformity than the third (CF) approach. In the experiments with real-life renal data, the effect of these correction methods on the mean TACs in either kidney were shown to be similar to those seen in the phantom experiments.

6.2 Future work

The findings in this thesis suggest several avenues for further investigation. The artifacts identified in Chapter 4 appear to be somewhat problematic for slow-rotation dynamic SPECT. While the correction methods investigated in this thesis are able to reduce these artifacts to a large extent, these methods are not ideal in some respects. In particular, their effectiveness depends to some extent on the accuracy of the segmentation, and they assume that the true distribution of activity is well-approximated by a template consisting of a small number of regions with spatially homogenous dynamic behaviour. This assumption may not be justified in real-life situations, and application of these techniques could lead to errors or bias as a result. The development of a more elegant approach to correct for attenuation artifacts would be useful, although at the present time it is not clear how this can be accomplished. It must be noted that these artifacts are just one of many sources of error that are present in any image reconstructed from SPECT data. Even if they cannot be corrected for fully, it is still possible to obtain useful information from a slow-rotation dynamic SPECT study provided that one is aware that these artifacts may be present.

A considerable amount of variation in TAC magnitudes was apparent in images reconstructed by both dEM and d^{2}EM. In 2D phantom experiments, images were also produced using OSEM to reconstruct each time frame independently, based on more complete projection data. The magnitude of TACs also varied noticeably in these images (see Figure 3.15), although less so than in the images reconstructed with d^{2}EM. Nonetheless, this indicates that even in idealized situations (i.e., the availability of complete dynamic projection data), variation among voxel-level TACs is inevitable if no spatial smoothing is performed. Investigating the use of spatial smoothing in tandem with d^{2}EM would be worthwhile. This could possibly be achieved by including a prior in the reconstruction algorithm, as is done in *maximum a posteriori* reconstruction for static imaging.

Testing the d^{2}EM algorithm in different clinical situations, such as dynamic cardiac imaging, would provide more context on its ability to recover accurate, three-dimensional information about dynamic *in vivo* processes. Dynamic cardiac imaging using a slow-rotating camera is challenging since the kinetic behaviour of tracer in some regions (e.g. the blood pool of the heart) is very rapid, meaning that reconstruction of these regions could be hampered by blurring effects such as those discussed in Chapter 4. Regions with different dynamic behaviour are also not as well-separated in cardiac studies as in the renal studies considered here. The fact that voxels in the heart region may contain a mixture of blood and myocardial tissue could be particularly problematic. Since the blood TAC features a sharp early peak followed by rapid washout, while the uptake and washout of tracer in the myocardium is more gradual, a mixture of the two may produce a TAC with two peaks, which dEM and d^{2}EM expressly forbid.

The development of new-model cardiac SPECT systems which acquire multiple simultaneous views of the patient has the potential to be a boon to dynamic cardiac SPECT imaging [69]. Although it is possible to produce dynamic images from data acquired on these systems by using a conventional algorithm such as OSEM to reconstruct each time frame independently, the use of an integrated approach such as dEM or d^{2}EM could provide benefits, since they process the entire dynamic data set simultaneously. Although the application of the dSPECT approach to this situation would be fundamentally the same as in the case of a slowly rotating camera, the system matrix used by the current dSPECT software would have to be altered in order to properly model the complicated geometry of these systems.

Appendix A

Full experimental results

This appendix contains full tabulated results from the experiments run in Chapters 3 and 5. Tables A.1 to A.3 contain results for the 2D phantom simulations of Chapter 3, while Tables A.4 to A.12 and Tables A.13 to A.14 contain results from the 3D phantom simulations and renal volunteer experiments of Chapter 5, respectively.

			Concave-up-decreasing			Concave-down-up			Concave-down		
			ε	$\bar{\sigma}$	$\mathcal{S}$	ε	$\bar{\sigma}$	$\mathcal{S}$	ε	$\bar{\sigma}$	$\mathcal{S}$
low noise	r1	dEM:	31.4	33.6	29.8	28.6	47.8	32.5	8.8	21.5	12.3
		d^{2}EM:	29.0	36.7	32.1	34.7	54.0	42.3	8.4	19.2	7.9
	r2	dEM:	20.0	25.7	19.8	25.8	34.2	25.1	8.2	21.1	11.6
		d^{2}EM:	13.2	23.3	13.3	17.8	31.5	19.3	7.2	18.9	5.3
	r3	dEM:	9.5	21.2	11.6	12.9	23.2	14.2	9.1	21.3	10.0
		d^{2}EM:	6.8	20.8	11.5	10.3	21.2	9.9	7.9	20.4	5.9
	r4	dEM:	8.8	20.1	7.9	11.5	22.3	12.3	9.9	21.3	8.9
		d^{2}EM:	7.2	20.2	7.6	9.4	20.4	7.5	8.3	20.9	5.7
mid noise	r1	dEM:	35.3	41.5	30.3	32.4	52.5	39.5	9.2	24.3	15.2
		d^{2}EM:	32.7	45.0	32.0	36.7	60.3	50.1	8.1	22.6	9.9
	r2	dEM:	20.1	36.1	26.3	30.2	44.5	31.7	10.2	25.4	14.8
		d^{2}EM:	13.0	33.1	20.6	21.3	41.9	23.6	8.5	22.6	7.8
	r3	dEM:	13.0	27.3	15.2	12.2	29.1	19.1	9.5	26.7	13.6
		d^{2}EM:	9.2	25.7	12.7	9.0	26.8	12.5	7.7	24.4	7.9
	r4	dEM:	8.4	21.4	9.6	12.8	27.2	15.5	10.7	25.6	10.6
		d^{2}EM:	6.9	21.4	8.9	10.0	24.4	9.1	8.8	24.9	7.2
high noise	r1	dEM:	28.7	73.7	40.5	34.0	84.2	50.8	13.6	47.6	32.8
		d^{2}EM:	28.6	76.6	41.2	37.9	79.9	55.1	10.4	37.4	15.3
	r2	dEM:	22.5	58.2	36.9	33.5	59.6	45.7	13.9	43.9	33.1
		d^{2}EM:	14.9	57.2	27.8	20.0	60.8	32.3	10.3	34.9	14.9
	r3	dEM:	17.2	45.4	25.3	16.2	43.6	32.7	11.4	40.0	27.1
		d^{2}EM:	13.5	44.3	18.9	8.8	34.5	16.2	6.8	34.3	13.1
	r4	dEM:	17.6	41.9	23.6	16.6	43.9	30.4	12.3	45.6	25.3
		d^{2}EM:	15.0	42.3	19.2	9.8	34.1	14.3	7.7	42.5	14.4

Table A.1: Error values after 80 iterations, 2D annulus phantom experiments.

			Concave-up-decreasing			Concave-down-up			Concave-down		
			ε	$\bar{\sigma}$	$\mathcal{S}$	ε	$\bar{\sigma}$	$\mathcal{S}$	ε	$\bar{\sigma}$	$\mathcal{S}$
low noise	r1	dEM:	28.2	23.8	22.8	22.8	24.5	23.7	6.1	20.4	12.5
		d^{2}EM:	30.2	27.0	28.7	26.8	30.3	32.7	6.5	17.2	6.5
	r2	dEM:	9.3	20.9	14.1	14.4	24.7	17.7	6.5	19.8	12.0
		d^{2}EM:	6.6	18.7	10.6	7.9	21.2	12.0	5.8	16.5	5.3
	r3	dEM:	9.2	18.3	10.8	7.5	17.9	8.7	6.4	19.1	10.6
		d^{2}EM:	8.2	17.0	9.6	5.2	16.6	5.4	5.3	16.8	4.8
	r4	dEM:	5.2	16.1	6.9	7.2	17.6	9.2	6.4	19.8	7.2
		d^{2}EM:	5.0	15.9	5.8	6.8	16.4	6.2	5.5	18.6	4.4
mid noise	r1	dEM:	29.7	36.4	27.7	24.0	36.3	29.8	6.4	25.4	15.4
		d^{2}EM:	33.9	40.9	35.5	25.8	45.1	39.5	5.9	21.3	8.5
	r2	dEM:	11.7	30.9	19.8	15.6	34.5	23.4	6.6	24.3	14.8
		d^{2}EM:	7.8	29.4	14.2	8.3	31.3	15.4	5.5	20.9	8.5
	r3	dEM:	11.8	26.8	16.5	7.1	26.9	14.6	6.7	27.2	13.6
		d^{2}EM:	9.9	25.4	13.1	3.8	24.6	8.4	5.3	24.6	7.0
	r4	dEM:	5.1	21.9	10.5	8.3	25.2	14.9	7.4	21.5	10.7
		d^{2}EM:	4.2	21.7	9.8	7.0	22.2	8.6	5.9	20.0	6.7
high noise	r1	dEM:	34.3	55.4	39.4	28.4	85.6	55.7	9.4	45.1	28.2
		d^{2}EM:	35.4	60.4	42.6	33.3	73.2	53.9	6.5	36.3	15.0
	r2	dEM:	13.9	51.9	31.9	21.9	56.9	37.2	9.1	39.8	26.2
		d^{2}EM:	8.0	48.7	23.2	10.0	57.0	27.0	6.4	30.8	12.5
	r3	dEM:	13.8	41.3	21.9	10.5	42.1	28.8	11.3	42.4	27.3
		d^{2}EM:	10.5	40.0	17.9	5.1	38.1	15.7	7.1	31.4	12.1
	r4	dEM:	6.6	32.7	16.9	9.9	42.2	28.0	10.5	38.6	25.0
		d^{2}EM:	3.0	32.2	15.1	6.2	32.6	13.2	5.8	31.5	13.2

Table A.2: Error values after 80 iterations, 2D ball phantom experiments.

			Concave-up-decreasing			Concave-down-up			Concave-down		
			ε	$\bar{\sigma}$	$\mathcal{S}$	ε	$\bar{\sigma}$	$\mathcal{S}$	ε	$\bar{\sigma}$	$\mathcal{S}$
low noise	r1	OSEM:	4.8	16.5	11.9	4.7	17.0	11.5	5.1	17.5	6.5
		d^{2}EM:	30.2	27.0	28.7	26.8	30.3	32.7	6.5	17.2	6.5
	r2	OSEM:	5.1	16.4	9.6	4.6	16.8	8.9	5.0	17.3	6.4
		d^{2}EM:	6.6	18.7	10.6	7.9	21.2	12.0	5.8	16.5	5.3
	r3	OSEM:	5.1	16.4	8.7	4.6	16.6	7.3	4.9	17.7	6.7
		d^{2}EM:	8.2	17.0	9.6	5.2	16.6	5.4	5.3	16.8	4.8
	r4	OSEM:	4.7	16.5	7.9	4.5	16.6	6.7	5.2	17.7	6.9
		d^{2}EM:	5.0	15.9	5.8	6.8	16.4	6.2	5.5	18.6	4.4
mid noise	r1	OSEM:	4.6	27.7	19.8	4.0	27.8	19.1	4.9	20.5	12.8
		d^{2}EM:	33.9	40.9	35.5	25.8	45.1	39.5	5.9	21.3	8.5
	r2	OSEM:	5.4	24.3	17.4	4.9	24.3	16.1	5.0	20.5	12.9
		d^{2}EM:	7.8	29.4	14.2	8.3	31.3	15.4	5.5	20.9	8.5
	r3	OSEM:	4.8	22.7	16.5	5.1	20.7	13.9	5.0	20.7	12.8
		d^{2}EM:	9.9	25.4	13.1	3.8	24.6	8.4	5.3	24.6	7.0
	r4	OSEM:	5.1	21.5	15.7	4.7	20.0	13.1	5.5	21.1	13.5
		d^{2}EM:	4.2	21.7	9.8	7.0	22.2	8.6	5.9	20.0	6.7
high noise	r1	OSEM:	6.3	52.2	36.5	6.0	53.4	35.7	5.4	29.8	25.0
		d^{2}EM:	35.4	60.4	42.6	33.3	73.2	53.9	6.5	36.3	15.0
	r2	OSEM:	5.3	44.1	33.2	4.9	42.0	29.4	5.5	30.0	25.0
		d^{2}EM:	8.0	48.7	23.2	10.0	57.0	27.0	6.4	30.8	12.5
	r3	OSEM:	5.8	38.1	31.0	5.6	32.2	26.4	5.7	29.9	25.0
		d^{2}EM:	10.5	40.0	18.0	5.1	38.1	15.7	7.1	31.4	12.1
	r4	OSEM:	5.9	34.6	29.6	5.2	29.4	24.7	5.7	31.6	26.4
		d^{2}EM:	3.0	32.2	15.1	6.2	32.6	13.2	5.8	31.5	13.2

Table A.3: Error values after 80 iterations of d^{2}EM versus 6 iterations of frame-by-frame OSEM with 8 subsets, 2D phantom experiments.

		Uncorrected		CF		IE		CF-IE	
		LK	RK	LK	RK	LK	RK	LK	RK
A	dEM	20.5	15.6	3.9	4.3	4.2	4.5	**3.4**	**4.0**
	d^{2}EM	15.6	11.7	**3.8**	**3.7**	4.9	3.8	4.1	4.5
B	dEM	15.7	16.4	2.3	3.1	2.1	4.0	**1.4**	**3.0**
	d^{2}EM	12.2	16.7	2.0	3.6	**0.9**	5.2	1.6	**2.1**
C	dEM	15.9	17.1	2.6	5.9	2.3	5.0	**1.5**	**4.7**
	d^{2}EM	12.1	12.1	2.1	**3.5**	**0.8**	4.9	1.9	5.5
D	dEM	21.5	16.8	**4.0**	3.3	4.5	4.1	**4.0**	**3.3**
	d^{2}EM	16.2	16.7	4.2	4.0	**3.9**	5.3	4.7	**3.0**
Avg.	dEM	18.4	16.5	3.2	4.2	3.3	4.4	**2.6**	**3.7**
	d^{2}EM	14.0	14.3	3.0	**3.7**	**2.6**	4.8	3.0	3.8

Table A.4: Error values ε before and after application of template correction for Phantoms A-D. Segmentation based on the true organ boundaries was used to create the template. The smallest error in each row for either kidney is bolded.

		Uncorrected		CF		IE		CF-IE	
		LK	RK	LK	RK	LK	RK	LK	RK
A	dEM	20.5	15.6	**3.8**	**5.2**	4.2	6.0	4.4	6.5
	d^{2}EM	15.6	11.7	4.4	5.1	**4.1**	**2.6**	4.6	6.8
B	dEM	15.7	16.4	**2.7**	**3.4**	4.4	4.1	3.2	4.3
	d^{2}EM	12.2	16.7	3.1	5.0	2.4	6.5	**2.3**	**4.6**
C	dEM	15.9	17.1	3.7	**6.0**	4.2	6.1	**3.5**	6.6
	d^{2}EM	12.1	12.1	3.7	4.3	**2.8**	**2.8**	3.3	7.2
D	dEM	21.5	16.8	**5.3**	**4.1**	5.3	4.1	5.7	4.3
	d^{2}EM	16.2	16.7	5.3	5.3	**4.1**	6.6	5.6	**5.1**
Avg.	dEM	18.4	16.5	**3.9**	**4.7**	4.5	5.1	4.2	5.4
	d^{2}EM	14.0	14.3	4.1	4.9	**3.4**	**4.7**	4.0	5.9

Table A.5: Error values ε before and after application of template correction for Phantoms A-D. Probabilistic segmentation was used to create the template. The smallest error in each row for either kidney is bolded.

		Uncorrected		CF		IE		CF-IE	
		LK	RK	LK	RK	LK	RK	LK	RK
A	dEM	34.2	33.2	23.0	22.0	16.3	16.4	**13.4**	**14.0**
	d^{2}EM	30.1	28.4	20.5	18.6	14.8	14.0	**11.4**	**10.8**
B	dEM	28.4	30.3	18.0	17.1	8.5	9.7	**7.5**	**7.4**
	d^{2}EM	25.3	27.1	14.8	15.0	8.5	9.3	**6.6**	**6.6**
C	dEM	29.3	36.2	17.6	24.0	8.2	17.8	**7.3**	**15.4**
	d^{2}EM	26.2	30.7	15.5	22.2	9.1	15.0	**7.3**	**12.6**
D	dEM	35.7	30.0	25.3	17.0	18.3	9.3	**15.2**	**7.3**
	d^{2}EM	32.2	26.4	23.6	13.8	17.0	8.4	**13.5**	**6.8**
Avg.	dEM	31.9	32.4	21.0	20.0	12.8	13.3	**10.8**	**11.0**
	d^{2}EM	28.4	28.2	18.6	17.4	12.3	11.7	**9.7**	**9.2**

Table A.6: Error values $\bar{\sigma}$ before and after application of template correction for Phantoms A-D. Segmentation based on the true organ boundaries was used to create the template. The smallest error in each row for either kidney is bolded.

		Uncorrected		CF		IE		CF-IE	
		LK	RK	LK	RK	LK	RK	LK	RK
A	dEM	**34.2**	33.2	37.1	29.9	35.0	26.7	35.4	**25.7**
	d^{2}EM	30.1	28.4	29.9	29.9	27.0	25.7	**26.8**	**25.5**
B	dEM	**28.4**	30.3	35.3	23.8	30.3	19.2	30.2	**15.1**
	d^{2}EM	25.3	27.1	22.9	21.1	20.1	18.1	**19.5**	**14.4**
C	dEM	**29.3**	36.2	37.5	34.4	31.4	31.6	32.3	**30.1**
	d^{2}EM	26.2	30.7	28.6	33.9	25.5	**28.5**	**25.4**	29.8
D	dEM	**35.7**	30.0	41.1	22.0	38.1	17.4	38.4	**15.0**
	d^{2}EM	32.2	26.4	33.4	19.8	**29.3**	17.1	30.3	**14.1**
Avg.	dEM	**31.9**	32.4	37.7	27.5	33.7	23.7	34.1	**21.5**
	d^{2}EM	28.4	28.2	28.7	26.2	25.5	22.3	**25.5**	**21.0**

Table A.7: Error values $\bar{\sigma}$ before and after application of template correction for Phantoms A-D. Probabilistic segmentation was used to create the template. The smallest error in each row for either kidney is bolded.

		Uncorrected		CF		IE		CF-IE	
		LK	RK	LK	RK	LK	RK	LK	RK
A	dEM	19.1	18.8	13.7	14.3	8.6	10.3	**8.1**	**9.5**
	d^{2}EM	11.8	12.0	8.7	9.9	7.3	7.4	**5.7**	**5.4**
B	dEM	14.3	17.8	11.2	13.3	4.4	6.4	**4.4**	**4.1**
	d^{2}EM	10.6	13.3	8.0	8.1	4.2	5.8	**2.6**	**2.8**
C	dEM	14.8	20.0	10.8	14.5	**3.9**	10.6	4.3	**9.8**
	d^{2}EM	10.8	12.6	8.3	10.1	4.7	7.7	**2.6**	**6.5**
D	dEM	19.5	17.8	13.9	13.1	9.3	6.8	**9.0**	**4.5**
	d^{2}EM	12.6	12.6	9.7	7.6	8.1	5.7	**7.1**	**2.8**
Avg.	dEM	16.9	18.6	12.4	13.8	6.6	8.5	**6.5**	**7.0**
	d^{2}EM	11.5	12.6	8.7	8.9	6.1	6.6	**4.5**	**4.4**

Table A.8: Error values $\mathcal{S}$ before and after application of template correction for Phantoms A-D. The smallest error in each row for either kidney is bolded.

		Uncorrected		CF		IE		CF-IE	
		LK	RK	LK	RK	LK	RK	LK	RK
A	dEM	19.1	18.8	18.5	15.3	**14.9**	11.8	15.1	**11.5**
	d^{2}EM	11.8	12.0	11.4	10.8	10.4	8.2	**9.2**	**7.6**
B	dEM	14.3	17.8	15.5	15.8	**11.0**	10.9	12.4	**9.1**
	d^{2}EM	10.6	13.3	9.8	9.9	7.2	**8.3**	**6.0**	10.6
C	dEM	14.8	20.0	15.1	16.5	**9.2**	13.2	11.3	**12.7**
	d^{2}EM	10.8	12.6	10.4	11.0	8.0	8.9	**7.2**	**8.4**
D	dEM	19.5	17.8	19.0	14.9	**15.9**	10.6	16.1	**9.1**
	d^{2}EM	12.6	12.6	12.1	9.3	11.0	**7.5**	**10.1**	9.1
Avg.	dEM	16.9	18.6	17.1	15.7	**12.8**	11.6	13.7	**10.6**
	d^{2}EM	11.5	12.6	10.9	10.3	9.2	**8.2**	**8.1**	9.0

Table A.9: Error values $\mathcal{S}$ before and after application of template correction for Phantoms A-D. Probabilistic segmentation was used to create the template. The smallest error in each row for either kidney is bolded.

Phantom E

		Uncorrected			CF			IE			CF-IE		
		LKu	LKh	RK	LKu	LKh	RK	LKu	LKh	RK	LKu	LKh	RK
Corr. Seg.	dEM	18.4	22.7	15.1	2.6	3.8	6.2	2.1	**3.3**	5.9	**1.7**	3.4	**4.9**
	d^2EM	14.2	17.8	10.5	1.9	4.7	**4.0**	**0.7**	5.0	5.4	1.9	**4.3**	5.0
Incorr. Seg.	dEM	18.4	22.7	15.1	5.0	8.9	6.0	**2.9**	**7.8**	5.9	3.8	8.2	**5.0**
	d^2EM	14.2	17.8	10.5	**3.3**	8.3	**4.2**	4.8	9.3	5.4	4.8	**8.1**	4.9
Prob. Seg.	dEM	18.4	22.7	15.1	9.0	**10.0**	5.9	9.2	10.0	**5.7**	**5.9**	10.0	6.5
	d^2EM	14.2	17.8	10.5	9.5	10.6	4.9	**9.4**	**10.4**	**3.6**	11.1	11.2	6.4

Phantom F

		Uncorrected			CF			IE			CF-IE		
		LK	RKu	RKh	LK	RKu	RKh	LK	RKu	RKh	LK	RKu	RKh
Corr. Seg.	dEM	19.3	18.8	21.7	3.8	4.7	8.3	4.3	4.2	8.3	**3.2**	**3.6**	**7.6**
	d^2EM	14.2	20.2	15.3	**2.5**	6.7	6.0	4.4	7.6	6.5	2.6	**4.7**	**5.7**
Incorr. Seg.	dEM	19.3	18.8	21.7	3.7	8.4	**15.2**	4.3	**6.8**	15.6	**3.2**	6.8	16.9
	d^2EM	14.2	20.2	15.3	**2.5**	**7.7**	**14.9**	4.4	10.9	15.9	**2.5**	8.1	16.8
Prob. Seg.	dEM	19.3	18.8	21.7	**3.9**	10.1	**11.8**	4.4	9.2	12.1	4.3	**8.9**	12.6
	d^2EM	14.2	20.2	15.3	3.6	9.6	**8.4**	**3.1**	10.1	9.0	3.8	**8.5**	10.9

Table A.10: Error values ε before and after application of template-based corrections for Phantoms E and F. “LKu/RKu” refer to the unhealthy portion of the left or right kidney (bottom 33%), while “LKh/RKh” refer to the healthy portion (the remainder of that kidney). “Corr. Seg.” refers to the correct segmentation using the true organ boundaries, where the unhealthy region was segmented separately; “Incorr. Seg” to the incorrect segmentation using the true organ boundaries, where the partially unhealthy kidney was assigned to a single segment; and “Prob. Seg” to the probabilistic segmentation, which included a separate segment for the unhealthy portion of the kidney. The smallest error in each row for each ROI is bolded.

Phantom E

		Uncorrected			CF			IE			CF-IE		
		LKu	LKh	RK	LKu	LKh	RK	LKu	LKh	RK	LKu	LKh	RK
Corr. Seg.	dEM	29.6	37.4	40.4	18.4	22.5	25.6	**7.7**	15.8	19.4	8.0	**15.2**	**16.8**
	d^{2}EM	25.8	34.4	34.9	15.5	22.4	23.2	**10.1**	15.8	16.4	11.0	**13.8**	**13.2**
Incorr. Seg.	dEM	29.6	37.4	40.4	19.1	29.6	25.6	**11.2**	**24.5**	19.4	11.9	25.1	**16.8**
	d^{2}EM	25.8	34.4	34.9	16.4	28.7	23.1	12.3	24.3	**12.3**	**11.5**	**22.6**	13.2
Prob. Seg.	dEM	29.6	37.4	40.4	29.1	25.1	31.3	**24.5**	19.9	27.3	24.8	**19.8**	**26.1**
	d^{2}EM	25.8	34.4	34.9	27.3	25.3	29.1	**26.2**	19.8	24.6	27.2	**19.3**	**22.7**

Phantom F

		Uncorrected			CF			IE			CF-IE		
		LK	RKu	RKh	LK	RKu	RKh	LK	RKu	RKh	LK	RKu	RKh
Corr. Seg.	dEM	35.8	30.8	41.0	23.2	16.8	27.4	17.8	10.1	21.5	**13.8**	**7.8**	**19.6**
	d^{2}EM	32.4	26.5	35.6	21.5	13.5	30.7	15.8	9.8	19.6	**11.5**	**7.5**	**15.6**
Incorr. Seg.	dEM	35.8	30.8	41.0	23.2	18.3	38.5	17.8	15.6	**33.9**	**13.9**	**14.4**	34.6
	d^{2}EM	32.4	26.5	35.6	21.5	25.9	47.4	15.9	17.1	33.1	**11.5**	**13.9**	**32.0**
Prob. Seg.	dEM	**35.8**	30.8	41.0	37.9	24.7	37.7	36.6	21.6	33.3	38.1	**21.4**	**33.0**
	d^{2}EM	**32.4**	26.5	35.6	37.7	21.0	51.4	35.8	21.2	**33.5**	37.6	**19.8**	33.7

Table A.11: Error values $\bar{\sigma}$ before and after application of template-based corrections for Phantoms E and F. "LKu/RKu" refer to the unhealthy portion of the left or right kidney (bottom 33%), while "LKh/RKh" refer to the healthy portion (the remainder of that kidney). "Corr. Seg." refers to the correct segmentation using the true organ boundaries, where the unhealthy region was segmented separately; "Incorr. Seg" to the incorrect segmentation using the true organ boundaries, where the partially unhealthy kidney was assigned to a single segment; and "Prob. Seg" to the probabilistic segmentation, which included a separate segment for the unhealthy portion of the kidney. The smallest error in each row for each ROI is bolded.

Phantom E

		Uncorrected			CF			IE			CF-IE		
		LKu	LKh	RK	LKu	LKh	RK	LKu	LKh	RK	LKu	LKh	RK
Corr. Seg.	dEM	15.1	20.1	20.4	10.5	12.8	14.6	**4.4**	8.8	10.7	4.9	**8.3**	**10.2**
	d^{2}EM	11.7	13.7	13.0	8.2	9.3	10.0	6.0	7.9	7.4	**5.1**	**5.3**	**5.9**
Incorr. Seg.	dEM	15.1	20.1	20.4	13.8	16.3	14.9	**7.6**	**12.1**	10.8	7.6	12.2	**10.2**
	d^{2}EM	11.7	13.7	13.0	11.0	12.5	10.0	7.6	12.2	7.4	**6.4**	**10.7**	**5.9**
Prob. Seg.	dEM	15.1	20.1	20.4	11.6	14.1	17.0	**5.9**	10.0	13.4	7.2	**9.4**	**13.2**
	d^{2}EM	11.7	13.7	13.0	10.6	9.9	12.7	**8.4**	8.7	10.4	9.2	**6.3**	**9.1**

Phantom F

		Uncorrected			CF			IE			CF-IE		
		LK	RKu	RKh	LK	RKu	RKh	LK	RKu	RKh	LK	RKu	RKh
Corr. Seg.	dEM	19.3	17.6	22.7	13.2	13.6	16.2	9.1	7.1	12.7	**8.8**	**4.8**	**11.1**
	d^{2}EM	12.4	12.3	14.9	9.0	7.4	11.4	7.5	7.5	9.8	**5.3**	**4.7**	**7.5**
Incorr. Seg.	dEM	19.3	17.6	22.7	13.2	16.0	22.0	9.2	11.7	**18.5**	**8.8**	**10.1**	19.1
	d^{2}EM	12.4	12.3	14.9	9.0	17.2	20.8	7.5	12.3	**17.1**	**5.3**	**8.5**	17.7
Prob. Seg.	dEM	19.3	17.6	22.7	16.7	16.3	19.3	**14.0**	10.8	**17.0**	14.3	**9.3**	17.9
	d^{2}EM	12.4	12.3	14.9	12.5	10.5	16.9	11.8	13.0	14.4	**10.3**	**10.3**	**14.2**

Table A.12: Error values $\mathcal{S}$ before and after application of template-based corrections for Phantoms E and F. “LKu/RKu” refer to the unhealthy portion of the left or right kidney (bottom 33%), while “LKh/RKh” refer to the healthy portion (the remainder of that kidney). “Corr. Seg.” refers to the correct segmentation using the true organ boundaries, where the unhealthy region was segmented separately; “Incorr. Seg” to the incorrect segmentation using the true organ boundaries, where the partially unhealthy kidney was assigned to a single segment; and “Prob. Seg” to the probabilistic segmentation, which included a separate segment for the unhealthy portion of the kidney. The smallest error in each row for each ROI is bolded.

		Volunteer #1				Volunteer #2			
		Uncorr.	CF	IE	CF-IE	Uncorr.	CF	IE	CF-IE
RK Inf.	dEM	**16.1**	20.7	20.7	21.8	12.6	12.7	**11.6**	13.5
	d^{2}EM	**17.1**	22.8	19.9	21.5	17.4	14.0	**12.7**	13.7
RK Sup.	dEM	12.3	**9.0**	9.4	9.8	12.9	13.9	**10.7**	11.6
	d^{2}EM	14.3	14.3	**8.7**	9.1	10.8	12.8	**9.3**	10.9
LK Inf.	dEM	**13.5**	18.5	17.1	16.0	**12.0**	17.4	14.8	15.1
	d^{2}EM	**14.5**	18.7	17.5	17.0	**11.2**	17.8	15.2	15.4
LK Sup.	dEM	14.0	12.3	11.1	**10.8**	**10.4**	20.3	17.8	19.5
	d^{2}EM	16.7	13.3	11.2	**10.9**	**9.9**	18.3	17.7	19.8
Average	dEM	**14.0**	15.1	14.6	14.6	**12.0**	16.1	13.7	14.9
	d^{2}EM	15.6	17.3	**14.4**	14.6	**12.3**	15.8	13.8	15.0

Table A.13: Relative weighted standard deviation values $\bar{\sigma}^*$ before and after application of template-based corrections. Row headings refer to the inferior and superior cube-shaped ROIs in the left and right kidneys. Smallest value in each row is bolded.

		Volunteer #1				Volunteer #2			
		Uncorr.	CF	IE	CF-IE	Uncorr.	CF	IE	CF-IE
RK Inf.	dEM	7.9	**7.7**	7.9	7.8	7.3	7.1	**5.7**	7.0
	d^{2}EM	5.6	10.0	**5.1**	5.5	9.6	7.5	5.0	**5.0**
RK Sup.	dEM	5.2	**5.0**	5.9	6.1	10.7	10.6	**6.7**	6.9
	d^{2}EM	5.8	6.3	**3.9**	**3.9**	7.2	8.1	**4.4**	4.5
LK Inf.	dEM	10.4	8.0	5.7	**5.7**	7.8	8.3	**7.3**	7.4
	d^{2}EM	8.4	7.4	5.5	**5.2**	**4.2**	4.7	4.2	4.5
LK Sup.	dEM	4.6	4.4	**3.6**	**3.6**	6.3	5.5	**4.5**	4.6
	d^{2}EM	4.0	4.3	2.7	**2.7**	3.5	4.0	**2.7**	2.8
Average	dEM	7.0	6.3	**5.8**	**5.8**	8.0	7.9	**6.1**	6.5
	d^{2}EM	6.0	7.0	**4.3**	**4.3**	6.1	6.1	**4.1**	4.2

Table A.14: Relative shape error values $\mathcal{S}^*$ before and after application of template-based corrections. Row headings refer to the inferior and superior cube-shaped ROIs in the left and right kidneys. Smallest value in each row is bolded.

Bibliography

[1] H. Akahira, H. Shirakawa, H. Shimoyama, M. Tsushima, H. Arima, K. Nigawara, T. Funyu, M. Sato, and T. Suzuki. Dynamic SPECT evaluation of renal plasma flow using technetium-99m MAG3 in kidney transplant patients. *J. Nucl. Med. Technol.*, 27:32–37, 1999.

[2] D.C. Barber. The use of principal components in the quantitative analysis of gamma camera dynamic studies. *Phys. Med. Biol.*, 25(2):283–292, 1980.

[3] H.H. Bauschke, D. Noll, A. Celler, and J.M. Borwein. An EM algorithm for dynamic SPECT. *IEEE Trans. Med. Imag.*, 18(3):252–261, 1999.

[4] S. Blinder, D. Noll, X. Hatchondo, A. Celler, J.-P. Esquerre, P. Payoux, and P. Gantet. Fully 4D dynamic image reconstruction by nonlinear constrained programming. In *Nuclear Science Symposium Conference Record, 2003 IEEE*, pages 3161–3165 Vol.5, 2003.

[5] C. Blondel, D. Noll, J. Maeght, A. Celler, and T. Farncombe. Comparison of different figure of merit functions for dynamic single photon emission computed tomography (dSPECT). *IEEE Trans. Nucl. Sci.*, 49(3):761–767, 2002.

[6] B.D. Bok, A.N. Bice, M. Clausen, D.F. Wong, and H.N. Wagner. Artifacts in camera based single photon emission computed tomography due to time activity variation. *European Journal of Nuclear Medicine and Molecular Imaging*, 13(9):439–442, 1987.

[7] J.M. Borwein and W. Sun. The stability analysis of dynamic SPECT systems. *Numerische Mathematik*, 77(3):283–298, 1997.

[8] P Bruyant. Analytic and iterative reconstruction algorithms in SPECT. *J. Nucl. Med.*, 43(10):1343–1358, 2002.

[9] T. Budinger, L. Araujo, N. Ranger, P. Coxson, G. Klein, R. Huesman, and A. Alavi. Dynamic SPECT feasibility studies [abstract]. *J. Nucl. Med.*, 32(5 (suppl.)):955, 1991.

[10] R. L. Burden and J. D. Faires. *Numerical analysis: Seventh Edition*, pages 408–409. Brooks/Cole, 2001.

[11] A. Celler, J.K. Bong, S. Blinder, R. Attariwala, D. Noll, L. Hook, T. Farncombe, and R. Harrop. Preliminary results of a clinical validation of the dSPECT method for determination of renal glomerular filtration rate (GFR). In *Nuclear Science Symposium Conference Record, 2001 IEEE*, pages 1079–1082 vol.2, 2001.

[12] A. Celler, T. Farncombe, C. Bever, D. Noll, J. Maeght, R. Harrop, and D. Lyster. Performance of the dynamic single photon emission computed tomography (dSPECT) method for decreasing or increasing activity changes. *Phys. Med. Biol.*, 45(12):3525–3543, 2000.

[13] A. Celler, T. Farncombe, R. Harrop, D. Noll, J. Maeght, and D. Lyster. Three approaches to dynamic SPECT imaging. In *Nuclear Science Symposium Conference Record, 1997 IEEE*, pages 1451–1455, 1997.

[14] P-C. Chiao, E.P. Ficaro, F. Dayanikli, W.L. Rogers, and M. Schwaiger. Compartmental analysis of Technetium-99m-Teboroxime kinetics employing fast dynamic SPECT at rest and stress. *J. Nucl. Med.*, 35(8):1265–1273, 1994.

[15] R. Di Paola, J.P. Bazin, F. Aubry, A. Aurengo, F. Cavailloles, J.Y. Herry, and E. Kahn. Handling of dynamic sequences in nuclear medicine. *IEEE Trans. Nucl. Sci.*, 29(4):1310–1321, 1982.

[16] T. Farncombe. *Functional dynamic SPECT imaging using a single slow camera rotation*. PhD thesis, University of British Columbia, Vancouver, Canada, 2000.

[17] T. Farncombe, S. Blinder, A. Celler, D. Noll, J. Maeght, and R. Harrop. A dynamic expectation maximization algorithm for single camera rotation dynamic SPECT

(dSPECT). In *Nuclear Science Symposium Conference Record, 2000 IEEE*, pages 15/31–15/35 vol.2, 2000.

[18] T. Farncombe, A. Celler, C. Bever, D. Noll, J. Maeght, and R. Harrop. The incorporation of organ uptake into dynamic SPECT (dSPECT) image reconstruction. *IEEE Trans. Nucl. Sci.*, 48(1):3–9, 2001.

[19] T. Farncombe, A. Celler, D. Noll, J. Maeght, and R. Harrop. Dynamic SPECT imaging using a single camera rotation (dSPECT). *IEEE Trans. Nucl. Sci.*, 46(4):1055–1061, 1999.

[20] T. Farncombe, M. King, A. Celler, and S. Blinder. A fully 4D expectation maximization algorithm using gaussian diffusion based detector response for slow camera rotation dynamic SPECT. In *Sixth meeting on fully three-dimensional image reconstruction in radiology and nuclear medicine*, 2001.

[21] B. Feng, P.H. Pretorius, T. Farncombe, S. Dahlberg, M. Narayanan, M. Wernick, A. Celler, J. Leppo, and M. King. Simultaneous assessment of cardiac perfusion and function using 5-dimensional imaging with Tc-99m teboroxime. *Journal of Nuclear Cardiology*, 13(3):354 – 361, 2006.

[22] L.R. Furenlid, D.W. Wilson, Y-C. Chen, H. Kim, P.J. Pietraski, M.J. Crawford, and H.H. Barrett. FastSPECT II: A second-generation high-resolution dynamic SPECT imager. *IEEE Trans. Nucl. Sci.*, 51(3):631–635, 2004.

[23] S.S. Gambhir, D.S. Berman, J. Ziffer, M. Nagler, M. Sandler, J. Patton, B. Hutton, T. Sharir, Sh. Ben Haim, and Si. Ben Haim. A novel high-sensitivity rapid-acquisition single-photon cardiac imaging camera. *J. Nucl. Med.*, 50(4):635–643, 2009.

[24] R. Gordon, R. Bender, and G.T. Herman. Algebraic reconstruction techniques (ART) for three-dimensional electron microscopy and X-ray photography. *Journal of Theoretical Biology*, 29:471–481, 1970.

[25] P. Green. Bayesian reconstructions from emission tomography data using a modified EM algorithm. *IEEE Trans. Med. Imag.*, 9(1), 1990.

[26] G. T. Gullberg, B. W. Reutter, A. Sitek, J. S. Maltz, and T. Budinger. Dynamic single photon emission computed tomography – basic principles and cardiac applications. *Phys. Med. Biol.*, 55(20):R111–R191, 2010.

[27] E. Haber, D. Oldenburg, T. Farncombe, and A. Celler. Direct estimation of dynamic parameters in SPECT tomography. *IEEE Trans. Nucl. Sci.*, 44:2425–2430, 1997.

[28] H.M. Hudson and R.S. Larkin. Accelerated image reconstruction using ordered subsets of projection data. *IEEE Trans. Med. Imag.*, 13(4):601–609, 1994.

[29] R.H. Huesman, B.W. Reutter, G.L. Zeng, and G.T. Gullberg. Kinetic parameter estimation from SPECT cone-beam projection measurements. *Phys. Med. Biol.*, 43(4):973–982, 1998.

[30] B.F. Hutton, J. Nuyts, and H. Zaidi. *Quantitative analysis in Nuclear Medicine Imaging*, chapter 4. Iterative Reconstruction Methods. Springer, 2006.

[31] M. Jin, Y. Yang, and M. King. Reconstruction of dynamic gated cardiac SPECT. *Med. Phys.*, 33(11):4384–4394, 2006.

[32] S. Kaczmarz. Approximate solution of systems of linear equations (trans. P.C. Parks). *International Journal of Control*, 57(3):1269–1271, 1993. (Originally published as: Angenäherte Auflösung von Systemen linearer Gleichunger. *Bulletin International de l'Academie Polonaise des Sciences. Lett A*, 355-357. 1937).

[33] D. J. Kadrmas, E. V. R. DiBella, R. H. Huesman, and G. T. Gullberg. Analytical propagation of errors in dynamic SPECT: estimators, degrading factors, bias and noise. *Phys. Med. Biol.*, 44(8):1997–2014, 1999.

[34] D. J. Kadrmas and G.T. Gullberg. 4D maximum a posteriori reconstruction in dynamic SPECT using a compartmental model-based prior. *Phys. Med. Biol.*, 46(5):1553–1574, 2001.

[35] R.E. Kalman. A new approach to linear filtering and prediction problems. *Transactions of the ASME – Journal of Basic Engineering*, 82, 1960.

[36] L. Kaufman. Maximum likelihood, least squares and penalized least squares for PET. *IEEE Trans. Med. Imag.*, 12(2):200–214, 1993.

[37] M. Kervinen, M. Vauhkonen, J. P. Kaipio, and P. A. Karjalainen. Time-varying reconstruction in single photon emission computed tomography. *International Journal of Imaging Systems and Technology*, 14(5):186–197, 2004.

[38] P.E. Kinahan, M. Defrise, and R. Clackdoyle. *Emission Tomography: The fundamentals of PET and SPECT*, chapter 20: Analytic Image Reconstruction Methods. Elsevier, 2004.

[39] M.A. King, S.J Glick, P.H. Pretorius, R.G. Wells, H.C. Gifford, M.V. Narayanan, and T. Farncombe. *Emission Tomography: The fundamentals of PET and SPECT*, chapter 22: Attenuation, Scatter and Spatial Resolution Compensation in SPECT. Elsevier, 2004.

[40] T-Y. Lee. Functional CT: physiological models. *Trends in Biotechnology*, 20(8):S3–S10, 2002.

[41] M.A. Limber, M.N. Limber, A. Celler, J.S. Barney, and J.M. Borwein. Direct reconstruction of functional parameters for dynamic SPECT. *IEEE Trans. Nucl. Sci.*, 42:1249–1256, 1995.

[42] J. M. Links, T.L. Frank, and L. C. Becker. Effect of differential tracer washout during SPECT acquisition. *J. Nucl. Med.*, 32(12):2253–2257, 1991.

[43] J. Maeght. *Analyse et méthodes pour un problème inverse en tomographie dynamique*. PhD thesis, L'Université Paul Sabatier, Toulouse, France, 2000.

[44] J. Maltz. Direct recovery of regional tracer kinetics from temporally inconsistent dynamic ECT projections using dimension-reduced time-activity basis. *Phys. Med. Biol.*, 45:3413–3429, 2000.

[45] I. Matsunari, T. Saga, J. Taki, Y. Akashi, J. Hirai, T. Wakasugi, T. Aoyama, M. Matoba, K. Ichiyanagi, and K. Hisada. Kinetics of iodine-123-BMIPP in patients with prior myocardial infarction: assessment with dynamic rest and stress images compared with stress thallium-201 SPECT. *J. Nucl. Med.*, 35(8):1279–1285, 1994.

[46] P.M. Matthews, G.D. Honey, and E.T. Bullmore. Applications of fMRI in translational medicine and clinical practice. *Nature Reviews: Neuroscience*, 7:732–744, 2006.

[47] C. Miyazaki, H. Harada, N. Shuke, A. Okizaki, M. Miura, and T. Hirano. ^{99m}Tc-DTPA dynamic SPECT and CT volumetry for measuring split renal function in live kidney donors. *Ann. Nucl. Med*, 24(3):189–195, 2010.

[48] J. Nagy and Z. Strakoš. Enforcing nonnegativity in image reconstruction algorithms. In *Proc. SPIE 4121: Mathematical modeling, estimation, and imaging*, pages 1451–1455, 2000.

[49] K. Nakajima, N. Shuke, J. Taki, T. Ichihara, N. Motomura, H. Bunko, and K. Hisada. A simulation of dynamic SPECT using radiopharmaceuticals with rapid clearance. *J. Nucl. Med.*, 33(6):1200–1206, 1992.

[50] K. Nakajima, J. Taki, H. Bunko, M. Matsudaira, A. Muramori, I. Matsunari, K. Hisada, and T. Ichihara. Dynamic acquisition with a three-headed SPECT system: application to technetium 99m-SQ30217 myocardial imaging. *J. Nucl. Med.*, 32(6):1273–1277, 1991.

[51] M.A. O'Connor and D.S. Cho. Rapid radiotracer washout from the heart: Effect on image quality in SPECT performed with a single-headed gamma camera system. *J. Nucl. Med*, 33(6):1146–1151, 1992.

[52] B. E. Oppenheim and J. D. Krepshaw. Dynamic hepatobiliary SPECT: a method for tomography of a changing radioactivity distribution. *J. Nucl. Med.*, 29(1):98–102, 1988.

[53] J. Qranfal. *Optimal recursive estimation techniques for dynamic medical image reconstruction*. PhD thesis, Simon Fraser University, Burnaby, British Columbia, Canada, 2009.

[54] J. Radon. On the determination of functions from their integral values along certain manifolds (trans. P.C. Parks). *IEEE Trans. Med. Imag.*, 5(4):170 –176, Dec.

1986. (Originally published as: Über die Bestimmung von Funktionen durch ihre Integralwerte längs gewisser Mannigfaltigkeiten. *Berichte über die Verhandlungen der Sächsische Akademie der Wissenschaften*, 69:262-277. 1917).

[55] A. Reader, F. Sureau, C. Comtat, R. Trébossen, and I. Buvat. Joint estimation of dynamic PET images and temporal basis functions using fully 4D ML-EM. *Phys. Med. Biol.*, 51:5455–5474, 2006.

[56] B.W. Reutter, G.T. Gullberg, and R. Huesman. Direct least-squares estimation of spatiotemporal distributions from dynamic SPECT projections using a spatial segmentation and temporal B-splines. *IEEE Trans Med. Imag.*, 19:434–450, 2000.

[57] B.W. Reutter, G.T. Gullberg, and R. Huesman. Effects of temporal modelling on the statistical uncertainty of spatiotemporal distributions estimated directly from dynamic SPECT projections. *Phys. Med. Biol.*, 47(15):2673–2683, 2002.

[58] B.W. Reutter, G.T. Gullberg, and R.H. Huesman. Kinetic parameter estimation from attenuated SPECT projection measurements. *Nuclear Science, IEEE Transactions on*, 45(6):3007–3013, 1998.

[59] B.W. Reutter, G.T. Gullberg, and R.H. Huesman. Kinetic parameter estimation from dynamic cardiac patient SPECT projection measurements. In *Nuclear Science Symposium Conference Record, 1998 IEEE*, pages 1953–1958, 1998.

[60] J. Roberts, R. Maddula, R. Clackdoyle, E. DiBella, and Z. Fu. The effect of acquisition interval and spatial resolution on dynamic cardiac imaging with a stationary SPECT camera. *Phys. Med. Biol.*, 52(15):4525–4540, 2007.

[61] S. G. Ross, A. Welch, G. T. Gullberg, and R. H. Huesman. An investigation into the effect of input function shape and image acquisition interval on estimates of washin for dynamic cardiac SPECT. *Phys. Med. Biol.*, 42(11):2193–2213, 1997.

[62] A. Saad, T. Möller, and G. Hamarneh. PropExplorer: Uncertainty-guided exploration and editing of probabilistic medical image segmentation. In *Computer Graphics Forum (Proceedings of Eurographics/IEEE-VGTC Symposium on Visualization 2010 (EuroVis 2010))*, volume 29, pages 1113–1120, 2010.

[63] W.P. Segars, D.S. Lalush, and B.M.W. Tsui. A realistic spline-based dynamic heart phantom. *IEEE Trans. Nucl, Sci.*, 46(3):503–506, 1999.

[64] S. Shcherbinin and A. Celler. Enhancement of quantitative accuracy of the SPECT/CT activity distribution reconstructions from physical phantom experiments. *Computerized Medical Imaging and Graphics*, 34(5):346–353, 2010.

[65] L.A. Shepp and Y. Vardi. Maximum likelihood reconstruction for emission tomography. *IEEE Trans. Med. Imag.*, MI-2:113–122, 1982.

[66] A. Sitek, E. Di Bella, and G. Gullberg. Factor analysis with a priori knowledge – application in dynamic cardiac SPECT. *Phys. Med. Biol.*, 45(9):2619–2638, 2000.

[67] A. Sitek, E. Di Bella, G.T. Gullberg, and R.H. Huesman. Removal of liver activity contamination in teboroxime dynamic cardiac SPECT imaging with the use of factor analysis. *J. Nucl. Cardiol.*, 9(2):197–205, 2002.

[68] A. Sitek, G.T. Gullberg, E.V.R. Di Bella, and A. Celler. Reconstruction of dynamic renal tomographic data acquired by slow rotation. *J. Nucl. Med.*, 42:1704–1712, 2001.

[69] P.J. Slomka, D.S. Berman, and G. Germano. New imaging protocols for new single photon emission CT technologies. *Current Cardiovascular Imaging Reports*, 3(3):162–170, 2010.

[70] A. M. Smith, G. T. Gullberg, and P. E. Christian. Experimental verification of technetium 99m-labeled teboroxime kinetic parameters the the myocardium with dynamic single-photon emission computed tomography: Reproducibility, correlation to flow, and susceptibility to extravascular contamination. *J. Nucl. Cardiol.*, 3(2):130–142, 1996.

[71] A.M Smith and G.T. Gullberg. Dynamic cardiac SPECT computer simulations for teboroxime kinetics. *IEEE Trans. Nucl. Sci.*, 41(4):1626–1633, 1994.

[72] A.M. Smith, G.T. Gullberg, P.E. Christian, and F.L. Datz. Kinetic modeling of teboroxime using dynamic SPECT imaging of a canine model. *J. Nucl. Med.*, 35(3):484–495, 1994.

[73] M. Soret, S.L. Bacharach, and I. Buvat. Partial-volume effect in PET tumor imaging. *J. Nucl. Med.*, 48:932–945, 2007.

[74] K. Suga, K. Nishigauchi, N. Kume, S. Koike, K. Takano, O. Tokuda, T. Matsumoto, and N. Matsunaga. Dynamic pulmonary SPECT of xenon-133 gas washout. *J. Nucl. Med.*, 37(5):807–814, 1996.

[75] A. Taylor and J. Ziffer. *Principles and Practices of Nuclear Medicine*, chapter 23: Urinary Tract. Mosby – Year Book, Inc., 2 edition, 1995.

[76] E. Vandervoort. Implementation of an analytically based scatter correction in SPECT reconstructions. Master's thesis, University of British Columbia, Vancouver, Canada, 2004.

[77] A. Welch, A. M. Smith, and G. T. Gullberg. An investigation of the effect of finite system resolution and photon noise on the bias and precision of dynamic cardiac SPECT parameters. *Medical Physics*, 22(11):1829–1836, 1995.

[78] R. G. Wells, T. Farncombe, E. Chang, and R. L. Nicholson. Reducing bladder artifacts in clinical pelvic SPECT images. *J. Nucl. Med.*, 45(8):1309–1314, 2004.

[79] R.G. Wells. *Analytical calculation of photon distributions in SPECT projections*. PhD thesis, University of British Columbia, Vancouver, Canada, 1997.

[80] L. Wen, S. Eberl, K-P Wong, D. Feng, and J. Bai. Effect of reconstruction and filtering on kinetic parameter estimation bias and reliability for dynamic SPECT: a simulation study. *IEEE Trans. Nucl. Sci.*, 52(1):69 – 78, 2005.

[81] G.L. Zeng, G.T. Gullberg, and R.H. Huesman. Using linear time-invariant system theory to estimate kinetic parameters directly from projection measurements. *IEEE Trans. Nucl. Sci.*, 42(6):2339–2346, 1995.